Characterization of a Geothermal Field using Multiscale Travel Time Tomography

A study of the Miravalles Geothermal Field in Costa Rica

by

Regine Johansen

Master of Science in
Renewable Energy

Abstract

The objective of this thesis is to investigate how travel time tomography and earthquake relocations can improve the understanding of the Miravalles geothermal field in Costa Rica.

Finding the answer to this research question requires a significant amount of work divided into different stages. First, the seismic waveform data was preprocessed, i.e. the arrival times of the P-waves were selected in SEISAN. After that, a ray tracing code was written. This was done by solving the ray equations numerically using the symplectic Euler method. In order to determine the origin of an earthquake a new grid search approach called P-wave single difference was developed. In contrast to conventional grid search methods which use the calculated arrival times and origin times, this method only requires the calculated travel time differences. Subsequently, the travel time tomography code was written and tested using various synthetic models. Finally, a new version of the multiscale travel time tomography was developed and applied to the data obtained in the first step. Unique to the method developed in this thesis, is that it employs three different parameterizations of the velocity model and that these are implemented progressively from the largest to the smallest. Earthquakes are also relocated for each new velocity model using the P-wave single difference algorithm.

The tomography yielded the first image of the Miravalles geothermal reservoir, showing that there is a correlation between locations of the earthquakes, the area of production and the geothermal reservoir. They furthermore indicated that the geothermal reservoir and the seismic activity are restricted by the Guayabo caldera border and la Fortuna graben. Lastly, a high velocity ellipsoid-shaped structure also became apparent. This may be a possible intrusion that has cooled. The relatively poor coverage in this area, however, makes it impossible at this stage to state this with absolute certainty; the possibility remains that it is an artifact of the tomography. This and other features can only be investigated further by employing more data and preferably a denser station coverage. Regardless, it is clear that the research conducted in this thesis shows that the locations of earthquakes and the P-wave velocity tomography yield quite a lot of information about the subsurface structure,

and that this knowledge can provide useful insight to the operators of the Miravalles geothermal field. The outcome of this study also suggests that geothermal reservoirs in general should be monitored with a dense enough network of seismometers, as this is probably the best way to image and monitor such reservoirs.

Acknowledgements

First of all, I would like to express my deepest gratitude to my supervisor, Henk Keers, without whose help and valuable insights this thesis would surely never have been written.

I would also like to thank my other supervisor, Lars Ottemöller, and his contact at ICE, Waldo Taylor, whose combined efforts provided me with important data from the Instituto Costarricense de Electricidad.

Further, I am grateful for the assistance given by my older sister, Talania, who has (somewhat unwillingly) used her leisure time to proofread this thesis.

I would also like to thank my fellow students for all the fun and memorable times we have had during the last five years at the University of Bergen.

Finally, I would like to thank my parents, Elisabeth and Johannes, my other siblings, Kristoffer and Rebekka, and my boyfriend, Vegard, for the great amount of support and chocolate (read: extra kilos) they have given me over the past year.

Contents

List of Figures

List of Tables

Chapter 1

Introduction

1.1 Overview

The first section of this chapter is dedicated to describing the energy consumption in the world based on source and the two main issues associated with hydrocarbon resources. The former is described in section 1.2 and the latter in section 1.3. In section 1.4 renewables are briefly introduced. Since the main focus of this thesis is geothermal energy, subsection 1.4.1 is used to discuss this in more detail. Even though geothermal fields come into being for a wide variety of reasons, they can all be categorized into four different types. These topics are discussed in sections 1.5 and 1.6. Finally, some of the issues linked to the exploration of geothermal resources are presented in section 1.7.

1.2 The Energy Outlook

Human beings worldwide consume a massive amount of energy on a daily basis. And as the population grows, so does the overall energy usage. It is therefore necessary to find reliable energy sources that can fulfill the present and future energy requirements.

Across history, human civilization has been dependent on primarily three forms of energy sources. Initially, wood functioned as the primary energy source. In the second part of the 18$^{\text{th}}$ century, however, it was surpassed by coal. Eventually, coal was in turn replaced by oil and natural gas. Now, in the 21$^{\text{st}}$ century, a new shift has begun and renewable energy resources are increasingly being used more widely [Zou et al., 2016].

Figure 1.1 shows the world consumption of various energy sources between the years

1992-2017. During this time period, hydrocarbons (oil, natural gas and coal) have been the main contributors to the energy mix. In comparison, renewable energy sources are the smallest contributors. It should be noted, however, that there has been a slight increase in the renewables in recent years.
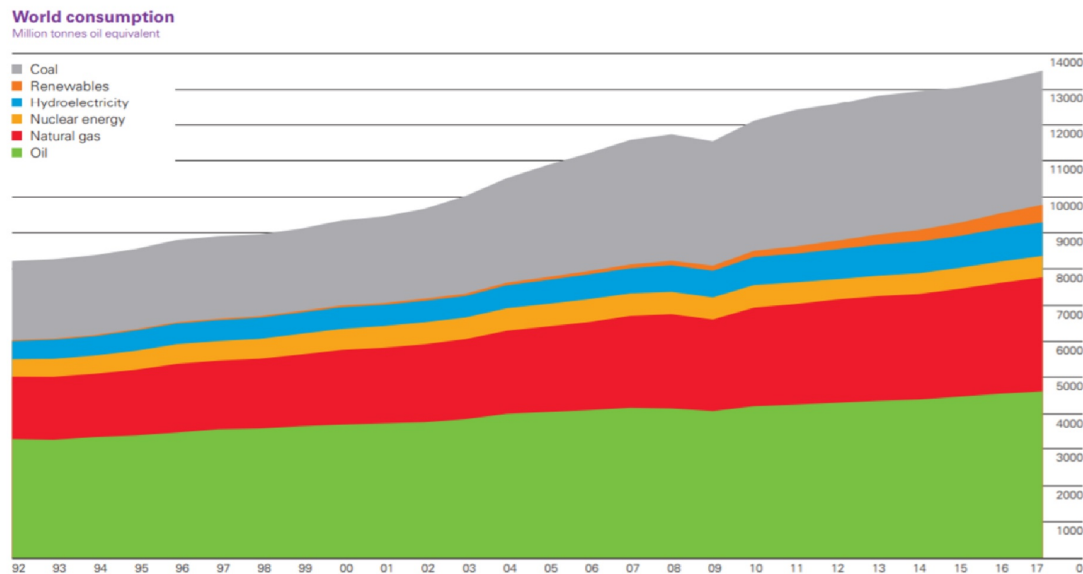
Figure 1.1: The world consumption of various energy resources over the years 1992-2017 in million tonnes oil equivalent. Retrieved from [British Petroleum, 2018]

1.3   Energy Challenges

The most important issues associated with hydrocarbons as the main source of energy are linked to their depletion and global warming. The depletion of hydrocarbons is inevitable, since their rate of extraction exceeds their rate of formation. Global warming, on the other hand, and its causes are one of the most prominent issues debated worldwide. According to the report "Climate Change (2013): The Physical Science Basis (2014)", human activity affects the energy budget of the earth. This is because greenhouse gases, such as carbon dioxide, are emitted into the atmosphere when hydrocarbons are burned [Cubasch et al., 2013]. Combined with the depletion of hydrocarbon resources, the negative effects of these emissions make it necessary to search for alternative and, preferably, renewable and clean energy sources.

1.4   Renewable Energy Sources

Renewable energy sources are characterized by the fact that they can be restored quickly and that greenhouse gas emissions are close or equal to zero. These types of energy sources are therefore invaluable in the effort to limit climate change [Stober and Bucher, 2013].

Almost 200 countries have signed the Paris Agreement which aims to confine the increase in global average temperature below 2°C [United Nations Climate Change, 2019]. As a consequence, the production of energy from renewable energy sources has been growing over the last couple of years. Today the largest renewable sources are solar, hydro, wind and biomass [IRENA, OECD/IEA and REN21, 2018].

One of the most important initiatives that has contributed to the increase of energy produced from renewable sources is subsidies. Subsidies for the various types of renewable energy sources are shown in Figure 1.2. Wind and solar energy receive the most financial support. Despite its tremendous potential, geothermal energy is by contrast among the least. The Massachusetts Institute of Technology [2006] has estimated that the potential amount of energy that can be extracted from geothermal fields in the US is 2000 times larger than the annual consumption of energy in the country.
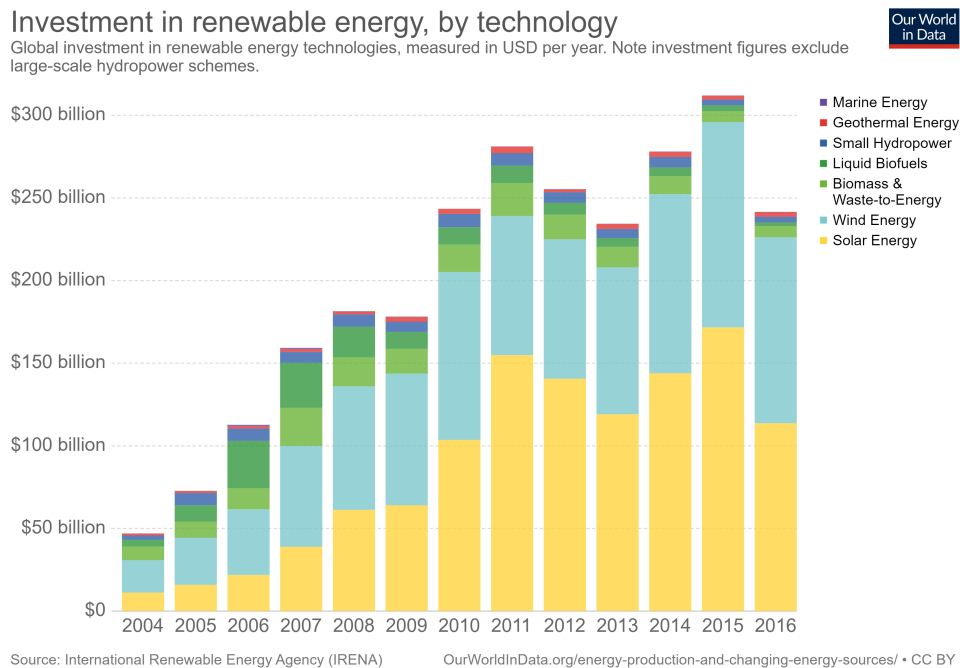
Figure 1.2: The distribution of subsidies per renewable energy source in the time period 2004-2016. Retrieved from [Ritchie and Roser, 2019].

1.4.1   Geothermal Energy

Geothermal energy is thermal energy that can be extracted from the uppermost layer of the Earth, i.e. the crust. This resource supplies energy continuously and can be utilized for both heat and electricity production.

Production of electricity at a geothermal field relies on the drilling of injection and production wells. Cold fluid is injected into the injection wells and heated fluid is extracted from the geothermal reservoir at the production wells. The heated fluid can in turn be used to drive a turbine-generator system in a power plant [Stober and Bucher, 2013].
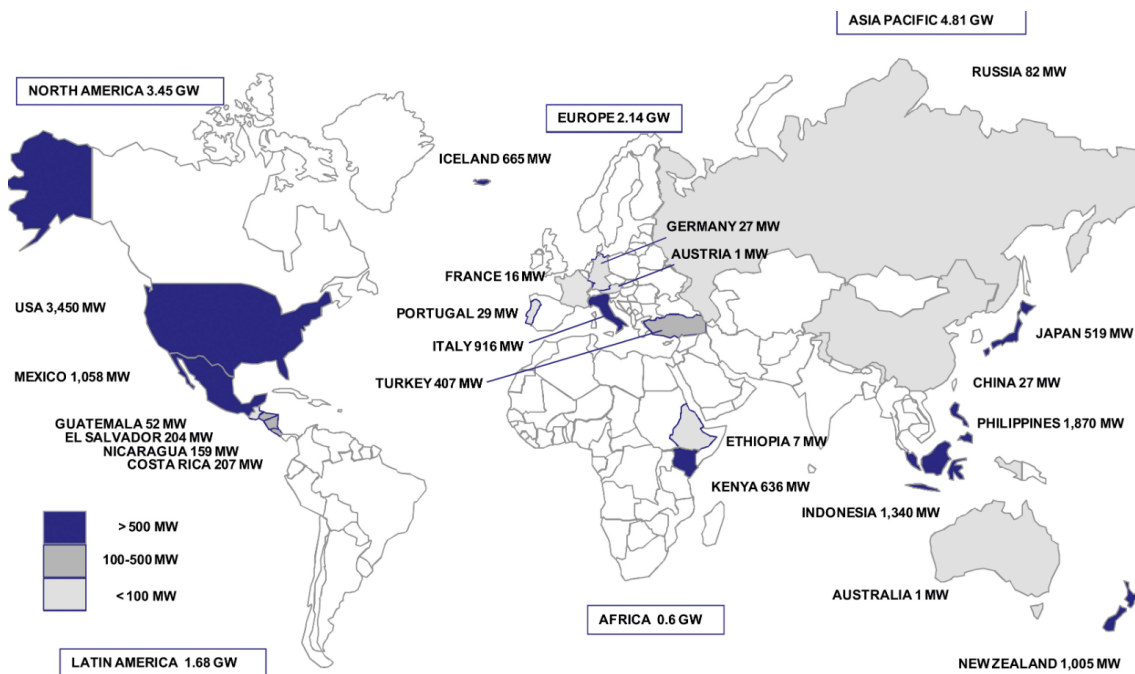
Figure 1.3: The world wide installed capacity of geothermal energy in 2015 [total of 12.6 GW]. Retrieved from [Bertani, 2016]

The total installed capacity of geothermal energy worldwide was approximately 12.6 GW in 2015 [Bertani, 2016]. The geographical distribution is shown in Figure 1.3. North America and Asia are the two continents with the largest installed capacity, with the US having the largest.

According to Lund et al. [2015], 82 countries, such as Canada, Iceland and France, utilized geothermal energy directly in 2015. Only 24 countries, however, produced electric power from geothermal energy. Nonetheless, Bertani [2016] estimates that 40 countries, primarily located in Central America and Africa, can satisfy their entire power production using their own geothermal resources.

Several countries have utilized their geothermal resources with great success. Admittedly though, not all attempts have been successful. Induced earthquakes, for instance, have resulted in the shutdown of geothermal power plants. This occurred at the Basel geothermal power plant in Switzerland [Gaucher et al., 2015]. The main underlying reason behind these failures is that this renewable resource is still quite poorly understood.

In order to increase the success rate of geothermal energy projects, further research is required to enhance the imaging of reservoirs and estimations of basic properties like seismic velocity, porosity and permeability. Studies aimed at improving technology, such as better drilling equipment/methods, are also important.

The main purpose of this thesis will be to investigate if multiscale travel time tomography and earthquake locations can yield an improved understanding of the Miravalles geothermal field located in Costa Rica, and especially how the determined hypocenter locations of earthquakes and the velocity of the subsurface correlate with the geothermal reservoir and its structure.

1.5   Geothermal Energy: Large Scale

Geothermal anomalies, i.e. higher temperature gradients, can be found worldwide and they exist for a variety of reasons. They are, however, primarily discovered at plate boundaries [Stober and Bucher, 2013].

Extensive research has been carried out on the connection between geothermal systems and plate tectonics (e.g. Dipippo [2007]; Williams et al. [2011]; Banks [2012]; Moeck [2014]), and it has been discovered that there is a good correlation between plate margins and the locations of existing geothermal fields (Figure 1.4). The most important type of plate boundary, in view of existing geothermal fields, is that of the convergent plate boundary (colored green in Figure 1.4).
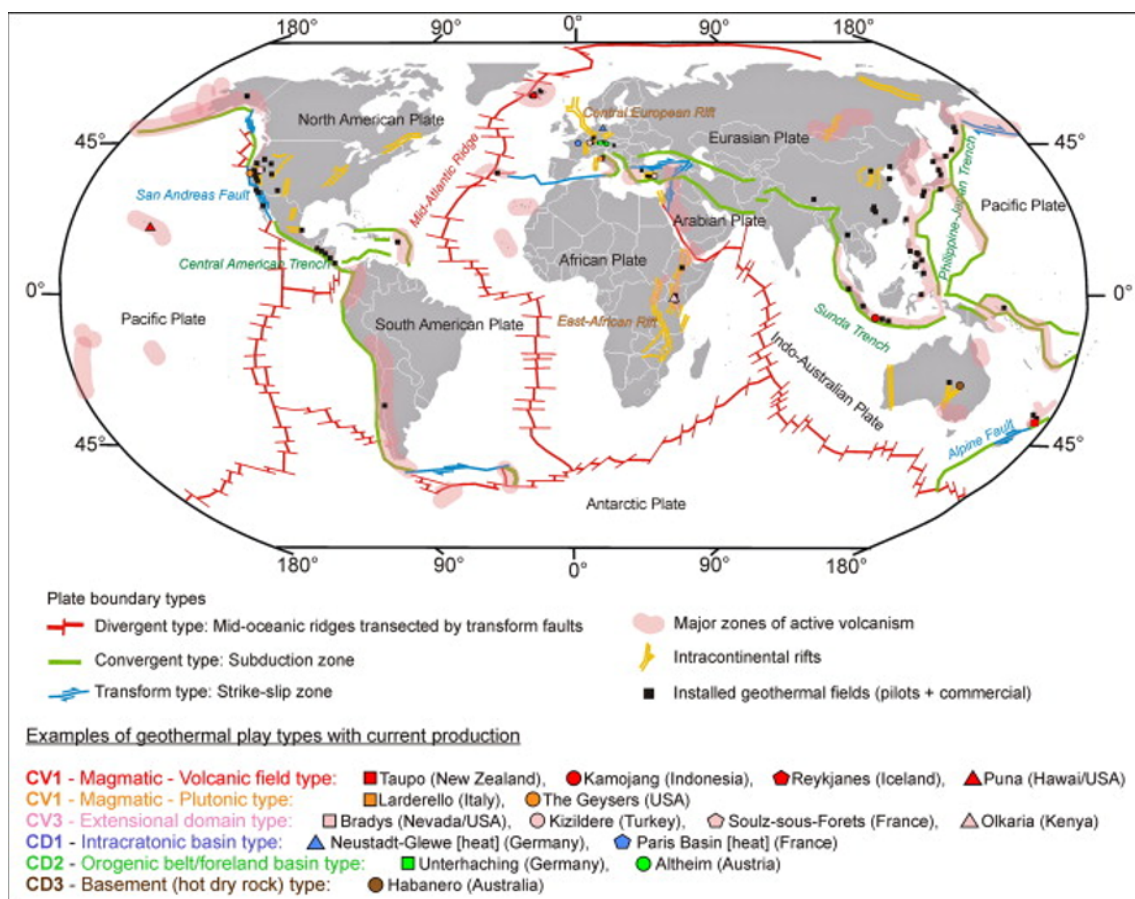
Figure 1.4: The correlation between plate boundaries and existing geothermal fields. Retrieved from Moeck [2014].

1.5.1   Plate Boundaries, Hotspots and Geothermal Energy

The high temperatures experienced at a geothermal field are often linked to three distinct tectonic locations: the extensional plate boundary, the convergent plate boundary and hot spots [Banks, 2012]. An extensional plate boundary is where two plates move away from each other (Figure 1.5a). Classic examples include the mid-oceanic ridges and proto-rifts like the Rhine Graben. The extensional regime causes thinning of the lithosphere. For this reason, the asthenosphere is found at shallower depths along with a higher temperature gradient [Banks, 2012].

The convergent plate boundary is characterized by two plates moving towards each other (Figure 1.5b). A plate with an oceanic crust has a higher density compared to one with a continental crust. As a consequence, the oceanic plate will bend and subduct into the asthenosphere under the opposing plate. Convergent plate boundaries give rise to trenches, accretionary prisms and chains of volcanoes. The latter develop as the downgoing slab melts and magma is generated. Since the magma has a lower density and higher temperature than the surrounding rock it rises [Stober and Bucher, 2013].
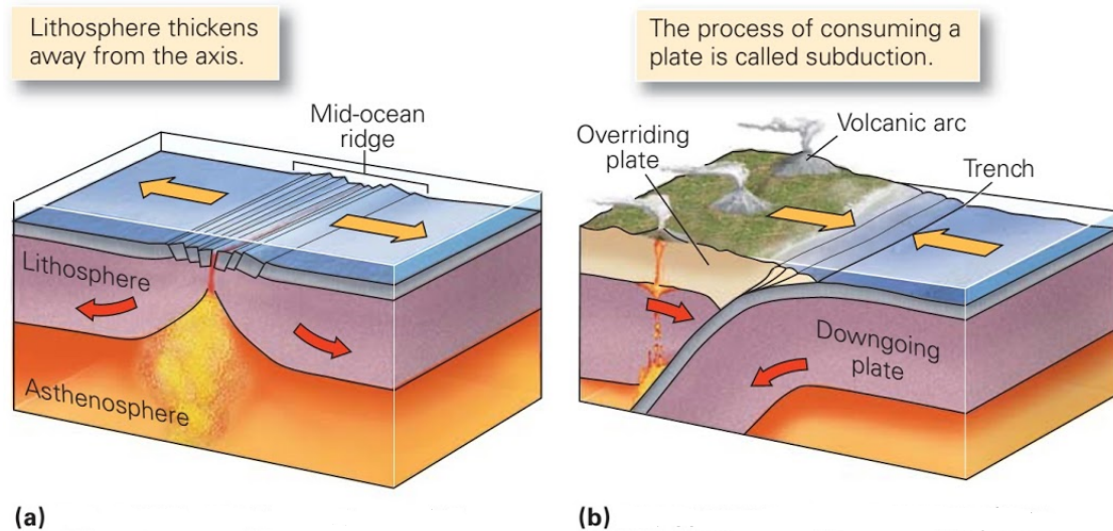
Figure 1.5: (a) A sketch illustration of a divergent plate boundary where two plates move away from each other. (b) A sketch of a divergent plate boundary where two plates move towards each other. Retrieved from Marshak [2012].

Although most volcanoes are a result of movement along plate boundaries, not all of them are. The Yellowstone National Park and Hawaii, for example, are located in the interior of the North American Plate and the Pacific Plate, respectively. These are linked to localized plumes of magma called hot spots [Marshak, 2012].

1.5.2   Other Possible Origins of Geothermal Energy

The majority of the explored geothermal fields of today are related to the tectonic settings already mentioned. There are, however, some that originate for other reasons, e.g. if faulting within a plate provides passage of heated fluid to the surface or if heterogeneities are located inside the crust [Banks, 2012]. Higher temperature gradients due to heterogeneities within the crust are caused by variations in rock properties, such as internal heat production and thermal conductivity. The former can be caused by radioactive decay or chemical oxidation of for example sulfides. The latter, on the other hand, can give rise to higher temperature gradients given that the thermal conductivity of a rock layer is low. The reason for this is that the combination of constant heat flux from the interior of the earth and low conductivity of layers of rocks result in a high temperature gradient. Observations of this have been made at the geothermal fields Southampton in the UK and Paris in France. According to Banks [2012], areas with high measurements of radioactive elements, like uranium and potassium, situated beneath a layer of rock with low conductivity could also be potential geothermal fields.

1.5.3   Tectonic Setting for the 20 Largest Geothermal Power Plants in 2011

Table 1.1 presents the 20 largest geothermal power plants worldwide in 2011 based on installed capacity. The tectonic setting and maximum magnitude of induced events for each of the power plants are also included.

Geothermal field name	Country	Installed Capacity (MW)	Tectonic setting	Maximum magnitude
The Geysers	USA	1584[8]	Extensional Regime[1]	4.6 M_L[10]
Cerro Prieto	Mexico	720[8]	Extensional Regime[1]	6.6 M_L[11]
Tongonan/ Leyte	The Philippines	716[8]	Compressional Regime[6]	-
Landerelleo	Italy	595[8]	Extensional Regime[7]	3.2 M_L[11]
Mak-Ban/Laguna	The Philippines	458[8]	Compressional Regime[6]	-
Gunung Salak- Java	Indonesia	377[8]	Compressional Regime[5]	-
Salton Sea- CA	USA	329[8]	Extensional Regime[1]	5.1M[13]
Coso- CA	USA	270[8]	Extensional Regime[2]	5.1M[12]
Darajat- Java	Indonesia	260[8]	Compressional Regime[5]	-
Tiwi/Albay	The Philippines	234[8]	Compressional Regime[6]	-
Wairakei	New Zealand	233[8]	Compressional Regime[4]	-
Wayang Windu- Java	Indonesia	227[8]	Compressional Regime[5]	-
Hellisheidi	Iceland	213[8]	Extensional Regime[1]	4.0M[14]
Heber- CA	USA	212[8]	Extensional Regime[1]	-
Olkaria	Kenya	202[8]	Extensional Regime[1]	2.5 M_D[11]
Kamojang- Java	Indonesia	200[8]	Compressional Regime[5]	-
Palinpinon/ Negros Oriental	The Philippines	193[8]	Compressional Regime[6]	-
Los Azufres	Mexico	188[8]	Compressional Regime[1]	1.9M_D[11]
Rotokawa	New Zealand	167[8]	Compressional Regime[4]	3.3M[11]
Miravalles	Costa Rica	163[9]	Compressional Regime[3]	3.9 M_L[15]

Table 1.1: The 20 largest geothermal fields in 2011 based on installed capacity. Here M_L is the local magnitude while M_D is the duration magnitude. M is used if the magnitude type is not specified in the data source. A hyphen indicates that no studies were found.

Based on Table 1.1, it is clear that in 2011 the largest geothermal fields emerged primarily as a result of convergent plate boundaries (60%). This corresponds well

---

[1][Harsh and Sukanta, 2007]
[2][Wohletz and Heiken, 1992]
[3][Huene et al., 2000]
[4][Wilson and Rowland, 2016]
[5][Purnomo and Pichler, 2014]
[6][Datuin and Troncales, 1986]
[7][Minissale, 1991]
[8][Bertani, 2012]
[9][Nietzen and Solís, 2015]
[10][Zang et al., 2014]
[11][The Human-Induced Earthquake Database (HiQuake), 2018]
[12][Schoenball et al., 2015]
[13][Brodsky and Lajoie, 2013]
[14][Juncu et al., 2018]
[15]From my data set.

with the theory that this type is the most important tectonic regime for geothermal fields, as mentioned in section 1.5. Nonetheless, some of the largest geothermal fields, i.e. The Geysers, Cerro Prieto and Larderello, have appeared due to extensional tectonic settings.

Table 1.1 also shows that the largest induced event had a local magnitude of 6.6 and took place at the Cerro Prieto geothermal field in Mexico. This order of magnitude, however, is rare; most events that happen at geothermal fields are characterized as microseismic, i.e. that they have a magnitude smaller than 2 [National Research Council, 2013].

1.6 Defining Geothermal Resources

The previous section investigated the locations and conditions that result in higher temperature gradients. In addition to a higher temperature gradient, however, one or more layers of permeable rock, i.e. a reservoir, as well as several other factors are required to exploit a geothermal field for electricity purposes.

First of all, the hot reservoir needs to be shallow enough to be accessible by drilling. The reason for this is that injection of relatively cold fluid and the extraction of heated fluid are the basic principles behind utilizing a geothermal resource. This also means that the circulation of fluid within the reservoir is vital for the production of geothermal energy. It is therefore also important that the permeability within the reservoir is high, i.e. permeability larger than 10 millidarcy [Moeck, 2014]. Ideally, the reservoir should contain generous amounts of fluids. These can originate for example, from rainwater that infiltrates the surrounding cooler rock and reaches the hot reservoir.

In addition to the general properties already mentioned, it is common to distinguish between four types of geothermal energy resources: enhanced geothermal systems (EGS), hydrothermal, geopressured and magmatic geothermal systems. These are discussed in further detail in subsections 1.6.1-1.6.4[1].

1.6.1 Enhanced Geothermal Systems

Recent developments in technology have made enhanced geothermal systems commercially available. This has resulted in an increase in locations that can be utilized for the production of electricity.

Enhanced geothermal systems (EGS) are anthropogenically made. The idea behind them is to improve the permeability of a reservoir. This can be achieved through the injection of fluid into it. For this reason, artificial reservoirs can be made anywhere granted the location of hot, dry rock is accessible by drilling [Barbier, 2002].

The setup for enhanced geothermal systems is illustrated in Figure 1.6. First, wells are drilled, e.g. an injection well, into the hot, dry rock. Afterwards, permeability is enhanced through artificially creating fractures or stimulating naturally occurring ones. This can be accomplished by for instance increasing the pore pressure by injecting large amounts of fluid through the injection well. Once the permeability is good enough, additional wells, e.g. production wells, are drilled into the fracture system. Finally, the field can be employed for electricity production [Olasolo et al., 2016].

---

[1]The reader is advised to take note that although all four of these are discussed, only hydrothermal systems are relevant for the work administered in relation to this thesis.

The geothermal field Soultz in France was the first commercial-scale EGS power plant in the world [Lu, 2018]. In 2013, a total number of 31 enhanced geothermal systems were in production [Breede et al., 2013]. Despite this development, the current exploration of this type of geothermal system is small compared to that of hydrothermal systems [Massachusetts Institute of Technology, 2006].
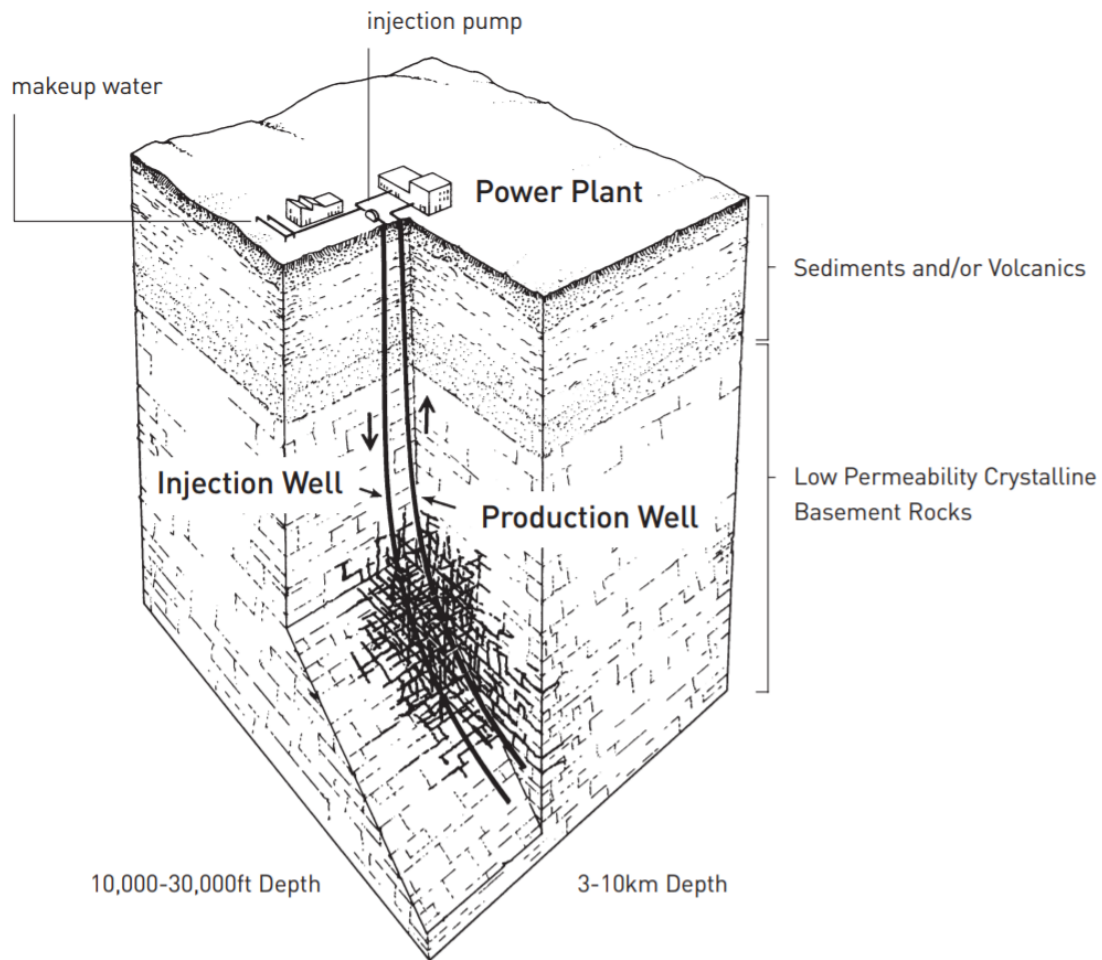
Figure 1.6: A conceptual model of an enhanced geothermal system. Retrieved from the Massachusetts Institute of Technology [2006]

1.6.2 Hydrothermal Systems

The majority of geothermal energy extraction occurs at hydrothermal systems [Barbier, 2002]. A typical hydrothermal system is displayed in Figure 1.7. The reservoir has an overlaying layer of impervious rock. This ensures that the heated fluid is maintained deep within the reservoir. The heat supply is from a magmatic intrusion and is located close to the reservoir. The reservoir is recharged with meteoric water, that is filtered through faults and fractures before it reaches the heated rocks. This type of geothermal system is often located at magmatically active regions, as well as zones that are structurally weak. The Miravalles field in Costa Rica, the Geysers in the US and the Larderello field in Italy are examples of such systems [Barbier, 2002].
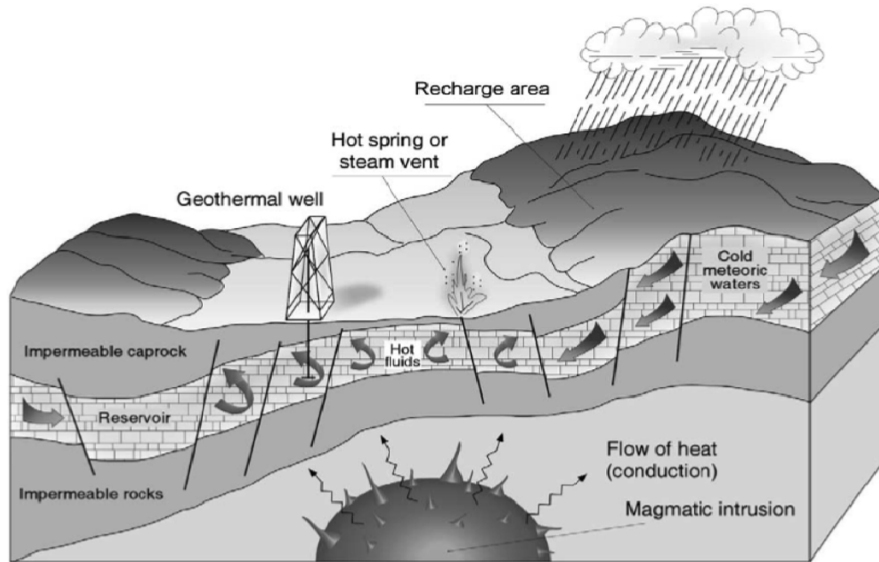
Figure 1.7: A conceptual model of a hydrothermal system. Retrieved from Barbier [2002]

1.6.3 Geopressured Geothermal Systems

A geopressured system is when the surrounding rocks are close to impenetrable. This causes the heated fluid to be detained within the reservoir and sealed from the surrounding cooler rocks. Geothermal systems of this variety have been located at basins where rapid fillings of sediment occur, such as in the sedimentary layers beneath the Gulf of Mexico [Harsh and Sukanta, 2007].

1.6.4   Magmatic Geothermal Systems

Energy extraction from a magmatic geothermal energy resource involves drilling into the magmatic body and injecting it with cold fluid under great pressure. This can result in a partial solidification of the magma, which in turn causes thermal stresses and cracking. Afterwards, recovery of the heated fluid can be used for energy extraction. Extremely high temperatures, however, make this process difficult to administer [Dipippo, 2007]. This type of geothermal system is extremely rare, but can be encountered at the Krafla geothermal field in Iceland [Reinsch et al., 2017].

1.7 Environmental Impact

As with all energy resources, there are certain potential disadvantages related to the utilization of geothermal ones. The disadvantages are, however, much smaller compared to those of hydrocarbon energy resources, and either similar or less than of other renewable energy resources [Ellabban et al., 2014; REN21, 2018]. Solar and wind, for example, rely on large amounts of rare earth elements. The exploration of which requires acids, which is bad for the environment.

In sections 1.7.1-1.7.4 some of the main issues linked to the exploration of geothermal energy are discussed. These are water pollution, air emissions, subsidence and induced seismicity [Barbier, 2002]. It is important to underscore, however, that the first three of these can be mitigated, while the final one is only a concern if the geothermal field is located close to densely populated areas.

1.7.1 Water Pollution

Water pollution can occur at a geothermal power plant if geothermal fluid is released into lakes and rivers. This is problematic since high concentrations of certain elements and minerals, e.g. boron, are toxic for the vegetation [Kristmannsdóttir and Ármannsson, 2003]. Solving this issue can be accomplished by reinjecting the fluid used back into the reservoir. Implementing this method has additional benefits as well, such as maintaining pore pressure. This is good as it makes it possible to extract a greater amount of heat from the reservoir and its lifetime can be extended [Barbier, 2002].

1.7.2 Air Pollution

Air pollution is caused by discharge of geothermal gases in steam. The steam mostly consists of water, but also contains carbon dioxide (CO_2) and smaller portions of mercury, boron, ammonia, methane, hydrogen sulfide and radon. Mercury, boron and ammonia can leach from the atmosphere via precipitation and contaminate soil, vegetation and surface water [Barbier, 2002].

Figure (1.8) shows a comparison of CO_2 emissions (g/kWh) from geothermal and hydrocarbon power plants. Emissions of carbon dioxide per kWh generated is much lower for a geothermal power plant than for ones that use fossil fuels. Creating geothermal power plants instead would therefore reduce the amount of carbon dioxide emitted into the atmosphere.

The magnitude of air pollution varies for open-loop and closed-loop systems. In open-loop systems, the steam interacts with the atmosphere and air pollution occurs. In closed-loop systems, the geothermal fluid is reinjected. There is no interaction
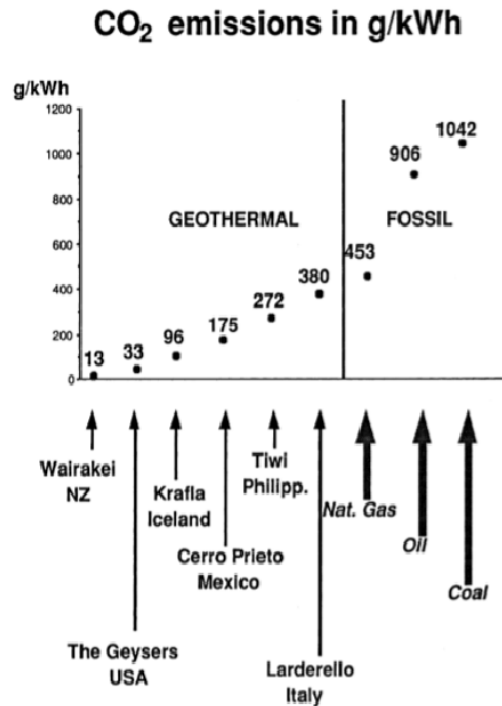
Figure 1.8: A comparison of geothermal and hydrocarbon power plant emissions of carbon dioxide. Retrieved from Barbier [2002].

between the geothermal fluid and the atmosphere. The air pollution in the closed-loop system is consequently minimal [REN21, 2018].

Research on technologies that can reduce the emissions from geothermal power plants is currently being administered, some of which has shown great potential. In Iceland, for example, the CarbFix project has demonstrated that carbon dioxide from geothermal power plants can be captured and stored [REN21, 2018].

1.7.3   Subsidence

Fluid withdrawal from the reservoir is necessary for power production at a geothermal field. This can, however, result in subsidence if the inflow of fluid is less than the extracted amount, i.e. a reduction in pore pressure takes place. Subsidence is, to varying degrees, observed at most geothermal fields. Reservoirs consisting of softer rock types are likely to experience more subsidence than those with harder rocks. Another important difference is that vapor-dominated fields tend to subside less than water-dominated ones. The Wairakei geothermal field in New Zealand, for instance, is water-dominated and had a local subsidence of 4.5 m between the years 1964-1974. The Geysers geothermal field in California, on the other hand, is vapor-

dominated and had a subsidence of 0.14 m over the period 1973-1977. Subsidence can be mitigated, or at least controlled, if fluid is reinjected into the reservoir, as it can help to maintain pore pressure. The downside of doing this is that it may induce microseismicity [Barbier, 2002].

1.7.4 Induced Seismicity

Nearly all geothermal reservoirs are found at or close to plate boundaries. For this reason, most geothermal reservoirs are located in regions prone to volcanic and seismic activity.

A seismic event takes place on a fault if the resistance to slip, the shear resistance, is smaller than the shear stress. Normal stress, shear stress and pore pressure are therefore important parameters to surveil [National Research Council, 2013]. Nonetheless, predicting whether an incident will take place is practically impossible [Stober and Bucher, 2013].

Earthquakes that occur due to anthropogenic activity are categorized as induced seismic events. This entails that they are caused by a build-up and release of stress in the subsurface, or that naturally existing stresses are released as a result of human activity [Stober and Bucher, 2013].

Induced events are often experienced at geothermal fields, since fluid injection and extraction provoke both stress and pore pressure changes in the reservoir and its surroundings. Injection can result in changes in pore pressure because of the high pressures required to force the injected fluid down into the reservoir. Another reason is that the difference in temperature of the fluid injected and extracted can lead to a thermal contraction of the reservoir. Fluid withdrawal, on the other hand, can cause a decrease in pore pressure and thereby affect the local stress regime [National Research Council, 2013].

Over the past decades, induced events related to the exploration of geothermal energy have been closely monitored [Stober and Bucher, 2013]. A reason for this is that induced events can indirectly yield information regarding the properties of the reservoir, e.g. the subsurface velocity structure and the extent of the permeable reservoir [Hutchings et al., 2014]. Another important factor is that induced events at geothermal reservoirs have become a source of interest to the public, particularly if the field is located close to a densely populated area [Knoblauch et al., 2019]. Public opinion is important, as it turns out it can result in the shutdown of geothermal power plants. This occurred at the Basel geothermal power plant in Switzerland where an induced earthquake of local magnitude 3.4 took place in 2006 [Gaucher et al., 2015].

The amount of induced seismicity at a vapor-dominated field, e.g. the Geysers

and the Landerello, differs from that of a water-dominated field, e.g. Miravalles. The reason for this is that the temperature differences between the injected and withdrawn fluid from the reservoir are smaller in a water-dominated field compared to a vapor-dominated one. That is, the injected fluid at a water-dominated field will result in less cooling of the reservoir. This field is therefore less prone to induced events given that the pressure difference at the top and bottom of the injection wells are limited. Pressure and temperature decline will normally follow after some years of production at a water-dominated field. The number of induced events can consequently increase. Observations of this have been made, for example, at the water-dominated field called Coso in the US [National Research Council, 2013].

A study was conducted at the Landerello geothermal field in Italy to find out whether there was a correlation between fluid reinjection and seismicity. The findings indicated that some of the microseismicity was induced. It also suggested that the number of induced events increased when the injected volume did as well. This correlation was not discovered for the magnitude of the events and the injected volume [Barbier, 2002]. Similar findings have been made at the Geysers geothermal field in California [National Research Council, 2013].

Chapter 2

Costa Rica and the Miravalles Geothermal Field

2.1 Overview

As has been previously mentioned, the main goal of this thesis is to study seismicity and determine the velocity structure of the Miravalles geothermal field in Costa Rica. For this reason, relevant background information about Costa Rica and its energy consumption is given in section 2.2, and the Miravalles geothermal field in section 2.3.

2.2 Costa Rica

Costa Rica has a population of approximately 5 million and its capital is San José [World Population Review, 2019]. The country is situated in the southern part of Central America, and borders to Nicaragua in the north and Panama in the southeast (Figure 2.1). In terms of plate tectonics, it is on the western margin of the Caribbean Plate. The volcanic ranges in the country are parallel to the western margin. They have formed due to the Cocos plate subducting beneath the western margin of the Caribbean plate (Figure 2.1) [Zhen-Wu, 2010].

Energy consumption in Costa Rica is rather eco-friendly when compared to many other countries in the world. The energy sources used to meet the energy needs of the country in the years 1970, 2013 and 2015 are shown in Figure 2.2. The electricity production in Costa Rica relies mainly on renewable energy sources. The importance of thermal energy sources, i.e. hydrocarbons, on the other hand, has been reduced substantially from 30% in 1970 to 1% in 2015. The electricity production from geothermal energy accounted for about 15% of the total energy production of the

country in 2013 and 11% in 2015 (Figure 2.2). This reduction is only in relative terms; the installed capacity of the geothermal fields has remained constant.
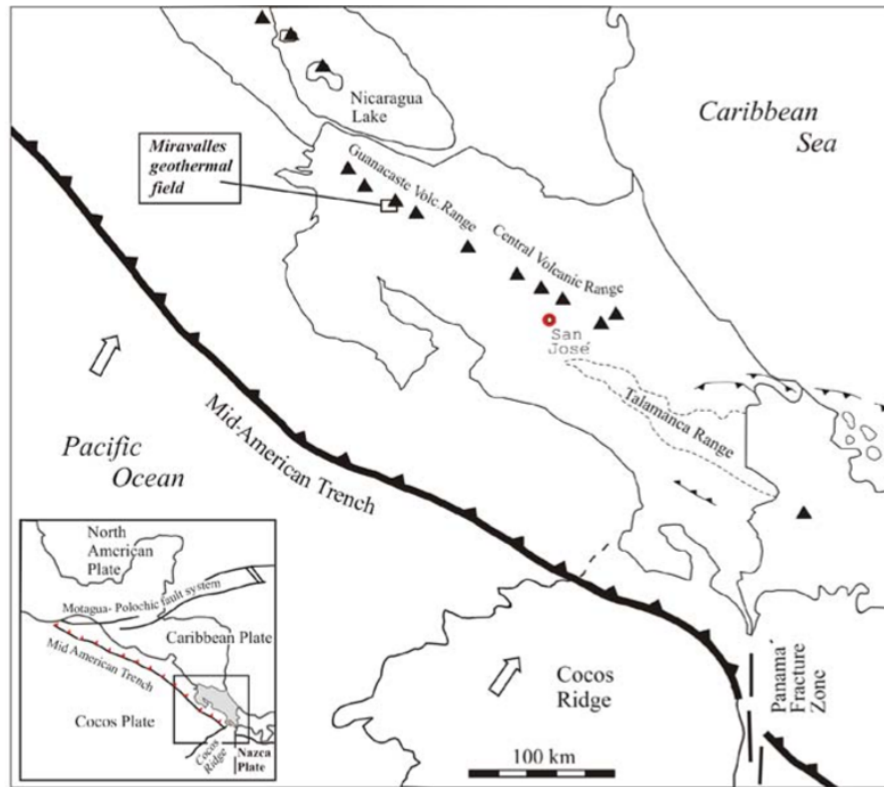
Figure 2.1: The tectonic situation in Southern Central America. Costa Rica is colored gray in the inserted figure in the bottom left corner. Retrieved from Rojas [2003].

The current energy mix in Costa Rica is the result of an energy crisis that took place in the 1970s. Prior to it, the electricity needs of the country were met by using hydro (70%) and thermal (hydrocarbons) (30%) energy sources. The rise of oil prices in the first half of the 1970s, however, resulted in the need for different and cheaper energy sources. As a consequence, the possibility for geothermal energy was investigated. Preliminary exploration studies were organized by the Instituto Costarricense de Electricidad (ICE) in 1975 at the Guanacaste volcanic range (Figure 2.1). Since these showed potential, ICE applied for loans from the Interamerican Development Bank to start the development of a geothermal field. Today this field is known as Miravalles [Moya and Yock, 2007].

There are currently two active geothermal sites in Costa Rica: Miravalles and Las Pilas. These provide power to the electrical grid. In addition to these, there are two other sites: Borinquen and Poco Sol. The former is currently under construction,
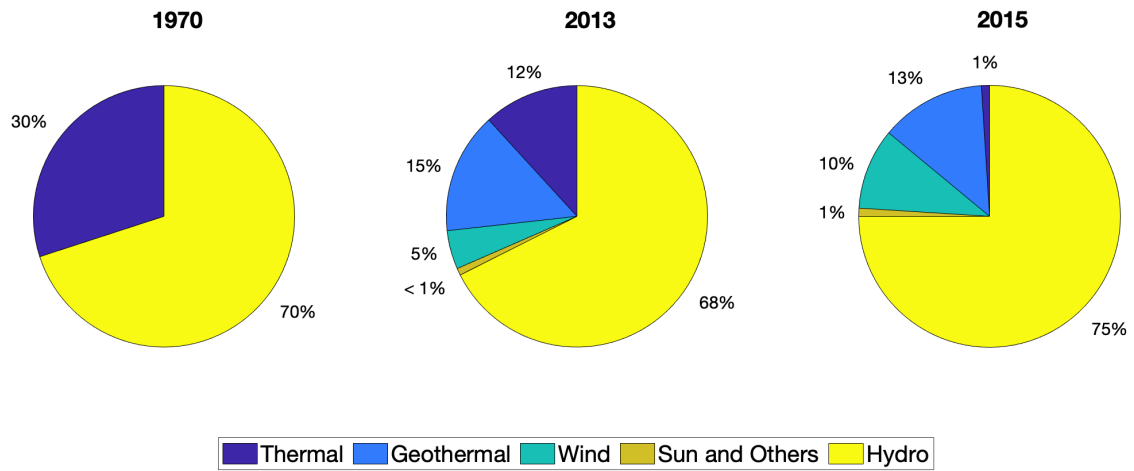
1970   **2013**   **2015**

Figure 2.2: The total electricity production according to source for Costa Rica in 1970, 2013 and 2015. Thermal energy refers to hydrocarbons. The figure is generated from data in Sánchez-Rivera and Vallejos-Ruiz [2015]; Fernando and Martí [2018].

while the latter exploration [Sánchez-Rivera and Vallejos-Ruiz, 2015].

2.3   The Miravalles Geothermal Field

The Miravalles geothermal field, has the largest geothermal power plant in Costa Rica. The field is located within the Guanacaste volcanic range and has a capacity of 163 MW (Figure 2.1). A schematic representation of its main features, especially the surface geology and faults, is shown in Figure 2.3. The Miravalles geothermal field is situated within the Guayabo caldera on the southwestern slope of the Miravalles stratovolcano, last active 7000 years ago. The existence of hot springs and fumaroles in the area, however, suggest that there is an active ongoing geothermal system in the area [Rojas, 2003].

The Miravalles geothermal field is characterized by several tectonic features. On a large scale, there is a NW-SE fracture parallel to the Guanacaste Volcanic Range. La Fortuna graben, located to the south of the caldera margin, is linked to this fracture system (Figure 2.3). On a smaller scale, on the other hand, four faults are found within the caldera border. The strike of the these, from oldest to youngest, are: NW-SE[1], N-S[2], NE-SW[3] and E-W[4] [Ruiz, 2013].

As already mentioned the Miravalles geothermal field is a hydrothermal system. Its reservoir is a water dominated aquifer located approximately 700 m below ground, varying in thickness from 800 to 1000 m. The permeability of the reservoir is mainly fracture related, and it is greatest at the southern part of the field. It gets smaller towards the northern part. The average value of the reservoir is in the range 50 to 100 millydarcy (high permeability[5]) [Ruiz, 2013].

The system of faults and fractures surrounding the Miravalles geothermal reservoir ensures a natural inflow of meteoric water. Most of the fluid that reaches the reservoir originates from the northeastern part of the field [González-Vargas et al., 2005]. The flow of fluid from the northeastern part is first parallel to the large normal fault. In the center of the field, however, it changes direction and runs parallel to the north-south fault system. Fluid is also injected into the reservoir, this occurs at the western and, predominately, southern sector of the field (the white zone marked by dashed lines in Figure 2.4). The fluid injected in the west has a temperature of 165 °C, while in the south 136 °C. The lower temperatures in the latter are caused by the fluid used there being first employed in a binary power plant for additional heat extraction before it is reinjected [Ruiz, 2013].

Inside the Miravalles geothermal field, the reservoir can be divided into four aquifers.

---

[1]The faults that cross Figure 2.4 from the top left corner to the center of it.

[2]The fault marked by a dashed line in the center of Figure 2.4.

[3]The large normal fault in Figure 2.4.

[4]The faults located in the top right corner of Figure 2.4.

[5]As already mentioned in sub-chapter (1.6), the permeability of a geothermal reservoir is relatively high if it is larger than 10 millydarcy [Moeck, 2014].
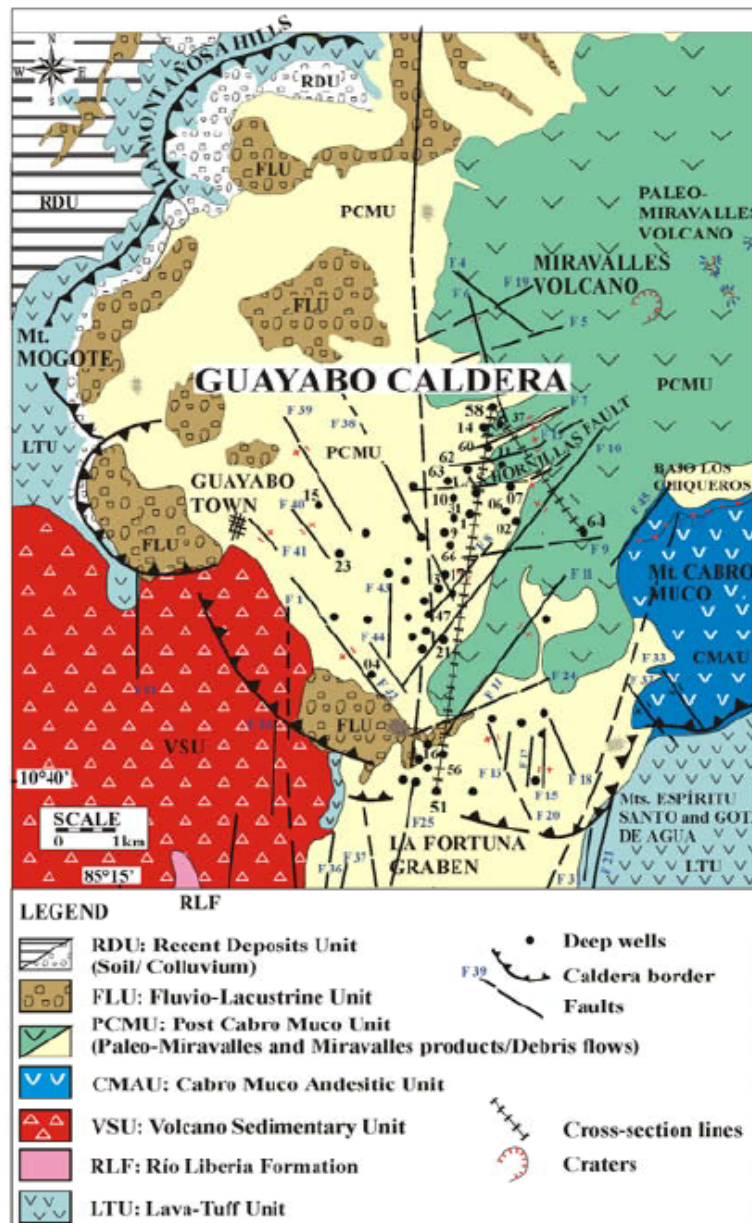
Figure 2.3: The surface geology and main tectonic features of the Guayabo caldera. Retrieved from Ruiz [2013].

Three of these have a pH of about 7. By contrast, the fourth is acidic [Zhen-Wu, 2010]. The main aquifer has temperatures ranging from 230 to 255°C (the yellow zone in Figure 2.4). Injected fluid moves through the fractures extending from the main aquifer towards the northeastern part of the field. The higher temperatures in this area cause the fluid to evaporate and a steam-dominated aquifer to form. This is the second aquifer [Sánchez-Rivera et al., 2010]. The third neutral aquifer is in
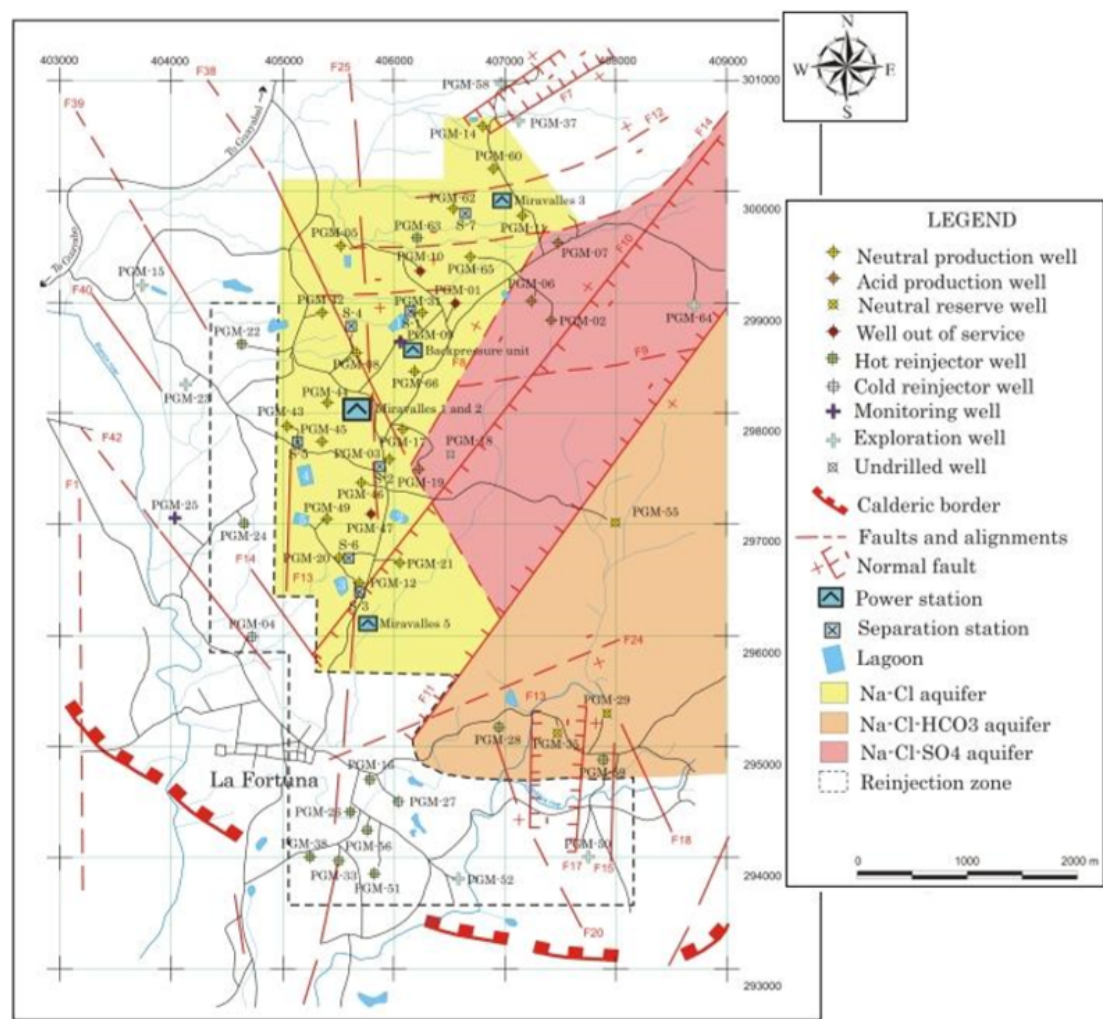
Figure 2.4: The main features of the Miravalles geothermal field. Three of the four reservoirs are colored. The yellow and orange areas are the natural reservoirs (aquifers 1 and 3), while the red area is the acidic reservoir (aquifer 4). The white zone marked by a dashed boundary is the area where fluid is injected. Retrieved from Sánchez-Rivera et al. [2010].

the southeastern sector of the field (the orange zone in Figure 2.4). Finally, the last aquifer is an acidic aquifer (the red zone in Figure 2.4).

Above the reservoir there is a cap rock. The thickness of it varies between 400 and 600 m. The larger values are found towards the central and southern part of the field. The exact location and depth of the heat source (magmatic body) is as of yet uncertain. Assumptions have nonetheless been made that it is situated towards the northeastern part of the field, near the Miravalles volcano [Ruiz, 2013]. This assumption correlates well with the measured (purple contour lines) and modeled temperatures (surface plot) of the field shown in Figure 2.5. The temperatures of the geothermal field are lowest at the southern and western parts.
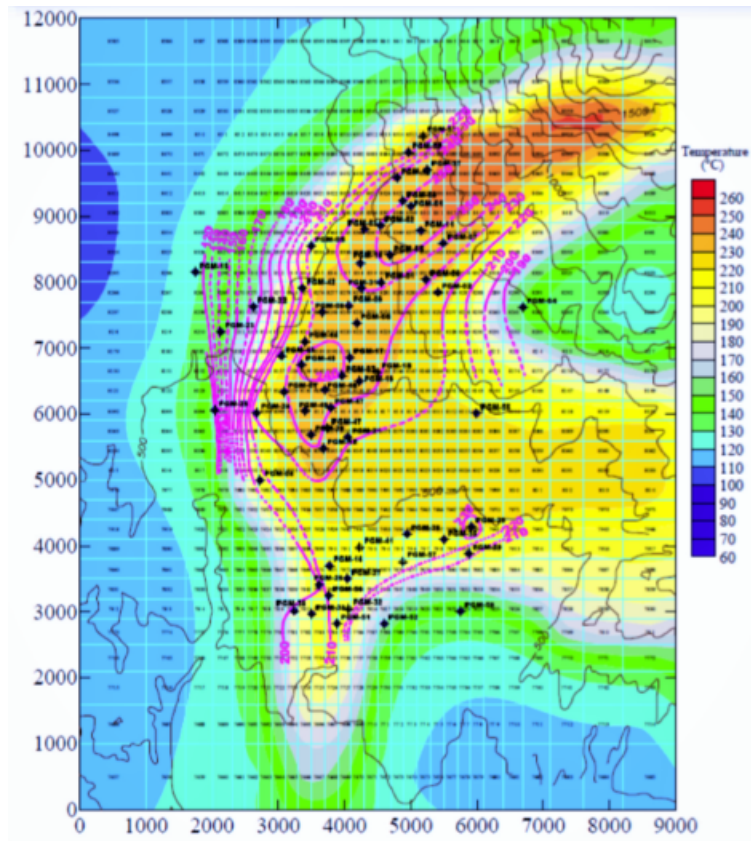
Figure 2.5: Temperatures at the Miravalles geothermal reservoir. The purple contour lines are based on measurements taken in the field, while the surface plot is numerically modeled. Retrieved from Ruiz [2013].

By 2013, 53 production, injection and observations wells had been drilled at the Miravalles geothermal field at depths varying from 900 to 3000 m [Ruiz, 2013]. The fluids extracted at the production wells are used to operate four units, as well as three 5 MW wellhead units of which only one is currently in operation (Table 2.1).

The field has been producing electricity since the startup of Unit 1 in 1994 [Moya et al., 2011]. The newest contribution to the field was was Unit 5 in 2003. This increased the total capacity from 144 MW to 163 MW [Nietzen and Solís, 2015].

Name of Power Plant	Commissioned Year	Status	Total Installed Capacity (MW)
Unit I	1994	Operative	55
Wellhead 1	1995	Operative	5
Wellhead 2	1996	Shut-down (1998)	5
Wellhead 3	1997	Shut-down (1999)	5
Unit II	1998	Operative	55
Unit III	2000	Operative	29
Unit V	2003	Operative	19

Table 2.1: Geothermal power plants at the Miravalles geothermal field. A modified version of a table in Nietzen and Solís [2015].

The growth in energy production at the Miravalles geothermal field is shown in Figure 2.6. The total installed capacity increased linearly between 1994-1997 with about 5 MW each year. It remained constant at 163 MW, however, between 2005-2019.
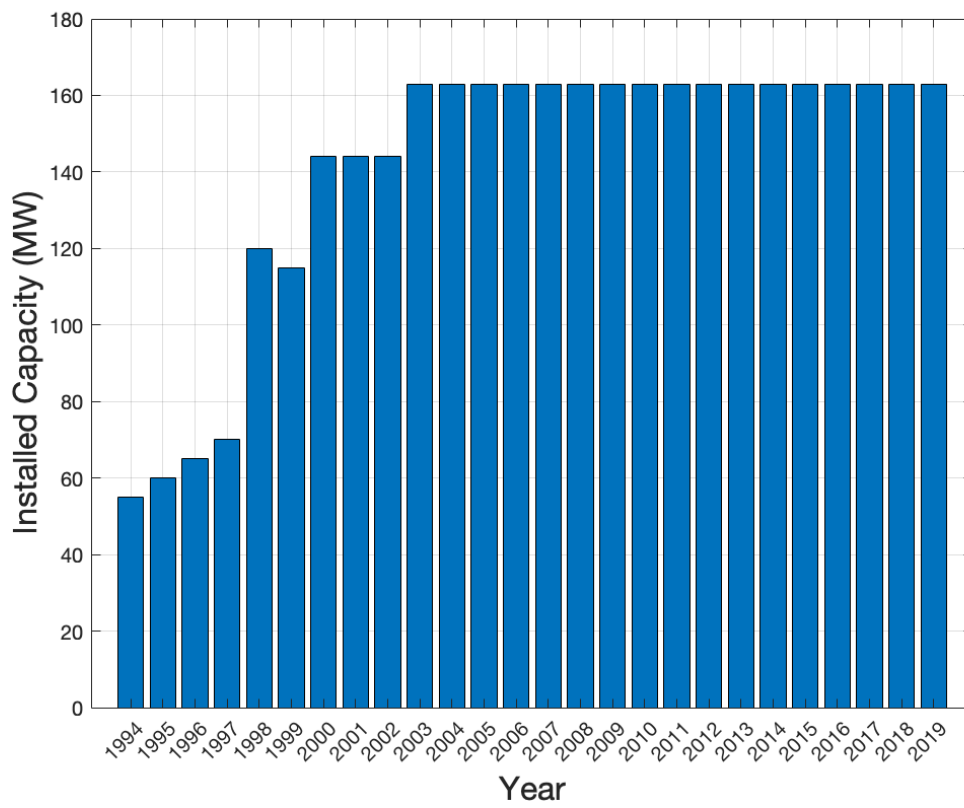
Figure 2.6: The annual total installed capacity (MW) at the Miravalles geothermal reservoir between 1994-2019. Created from data in Table 2.1.

2.3.1   Microseismicity at the Miravalles Geothermal Field

Microseismicity can occur at geothermal fields during both the exploration- and production-phase. This is because injection and extraction of fluid from the field, as well as changes in temperatures in the reservoir can cause changes in the local stress regime [National Research Council, 2013].

Figure 2.7 shows the annual seismicity at the Miravalles geothermal field from 1994 to 2013. The number of events per year was small during the first decade of production. Since 2004, however, there has been a considerable increase in seismic activity. The year with the highest number of events was 2010. Studies have found that this correlated with a decrease in the total amount of fluid injected at the Miravalles geothermal field [Nietzen and Solís, 2015].
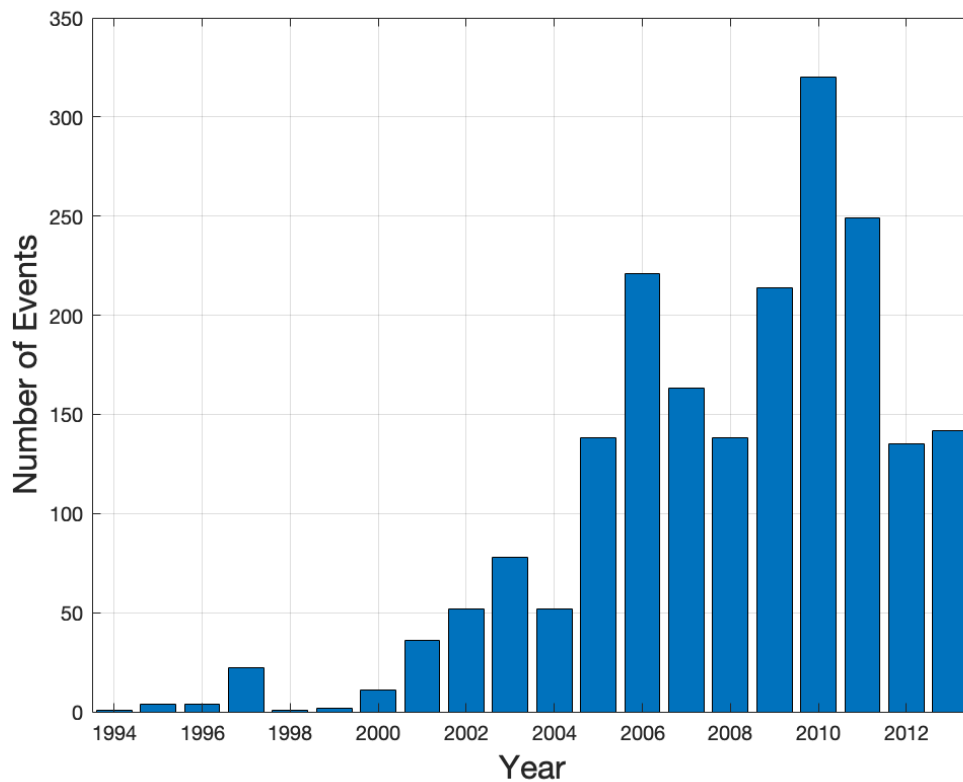
Figure 2.7: Number of detected earthquakes per year at the Miravalles geothermal field between 1994 and 2013. Modified figure from Nietzen and Solís [2015]

Chapter 3

Theory: Seismic Wave Propagation

3.1 Overview

In this chapter, the theory behind seismic wave propagating in acoustic and elastic media is presented. In sections 3.4 and 3.8 the eikonal equation is derived for both instances. Solving the eikonal equation for wavefronts can be computational demanding [Rawlinson et al., 2010]. Consequently, instead of investigating wavefronts rays will be look at in section 3.5. An analytical solution for rays propagating through a complex elastic structure does not exist. A numerical solution, however, can be found. In section 3.6, symplectic Euler is introduced. This is the numerical solution employed to solve the ray equations in this thesis. The concepts behind one- and two-point ray tracing are discussed in section 3.7. Two-point ray tracing results give the ray path and travel time of the wave traveling from the source to a receiver.

3.2 The Acoustic Wave Equation

The acoustic wave equation describes how the pressure field U changes as the waves propagate away from the source S (see e.g. [Cerveny, 2001; Stein and Wysession, 2003; Chapman, 2004]), and is given by:

$$\nabla^2 U(\mathbf{x}, t) - \frac{1}{c^2(\mathbf{x})} \frac{\partial^2 U(\mathbf{x}, t)}{\partial t^2} = S(\mathbf{x}, t). \tag{3.1}$$

Here ∇^2 is the Laplacian operator, t is the time and $\mathbf{x}$ is the position vector. The velocity at position $\mathbf{x}$ is given by $c(\mathbf{x})$. The Cartesian coordinates of $\mathbf{x}$ are x, y and z.

The acoustic wave equation (3.1) is a linear partial differential equation. In order to solve it, initial conditions are required. These are the pressure field at time $t = 0$, $U(\mathbf{x}, 0)$, and the first time derivative of the pressure field $\partial U(\mathbf{x}, 0)/\partial t$.

Some of the analyses of the acoustic wave equation are often more conveniently done in the frequency domain. The transformation from the time domain to the frequency domain is done through the Fourier transformation. It and its inverse are defined as:

$$f(t) = \frac{1}{2\pi} \int F(\omega) e^{-i\omega t} d\omega \leftrightarrow F(\omega) = \int f(t) e^{i\omega t} dt, \tag{3.2}$$

where $\omega = 2\pi f$, ω is the angular frequency and f is the frequency.

Fourier transformation is applied to the acoustic wave equation to get its equivalent in the frequency domain:

$$\nabla^2 U(\mathbf{x}, \omega) - \frac{\omega^2}{c^2(\mathbf{x})} U(\mathbf{x}, \omega) = S(\mathbf{x}, \omega). \tag{3.3}$$

This equation is called the Helmholtz equation. One of the main challenges in seismology is to solve equation (3.1) (or, equivalently, equation (3.3)) for the case when the source is known and the velocity is a function of x, y, and z. This can be done either using fully numerical techniques, such as finite difference or finite element methods, or using approximate techniques like ray tracing. The former are slow, but accurate. The latter are fast, but approximate [Chapman, 2004]. In this thesis ray tracing is used, as computing travel times is of interest, which is one of the parameters provided by ray tracing.

3.3   The Green Function

It is often convenient to express the source term in equation (3.1) as a point source:

$$S(\mathbf{x}, t) = -\delta(\mathbf{x} - \mathbf{x}_s)\delta(t), \tag{3.4}$$

where the position of the source is given by $\mathbf{x}_s$ and $\delta(t)$ is the Dirac-delta function:

$$\delta(t) = \begin{cases} 1 & \text{if } t = 0, \\ 0 & \text{if } t \neq 0. \end{cases} \tag{3.5}$$

The solution of the acoustic wave equation (3.1) for a point source (3.4) is called the Green function, G [Cerveny, 2001]. The Green function therefore satisfies:

$$\nabla^2 G(\mathbf{x}, t) - \frac{1}{c^2(\mathbf{x})} \frac{\partial^2 G(\mathbf{x}, t)}{\partial t^2} = -\delta(\mathbf{x} - \mathbf{x}_s)\delta(t). \tag{3.6}$$

Consequently, the solution for a general source $S(\mathbf{x}, t)$ can be computed by means of superposition:

$$U(\mathbf{x}, t) = \int G(\mathbf{x}, \mathbf{x}_s, t) S(\mathbf{x}_s, t) d\mathbf{x}_s dt. \tag{3.7}$$

It is useful to note that the Green function can be computed explicitly for a homogeneous medium [Cerveny, 2001]:

$$G(\mathbf{x}, t) = \frac{1}{4\pi |\mathbf{x} - \mathbf{x}_s|} \delta(t - \frac{|\mathbf{x} - \mathbf{x}_s|}{c}). \tag{3.8}$$

Here $1/4\pi |\mathbf{x} - \mathbf{x}_s|$ is the amplitude and $|\mathbf{x} - \mathbf{x}_s|/c$ is the travel time of the wavefield. An analytical solution of the Green function is inadequate for a more complex medium. Instead of solving the wave equation analytically, however, it can be solved using ray theory [Cerveny, 2001]. This technique is described in more detail in remainder of this chapter.

3.4 The Eikonal & Transport Equation

In this thesis, the high frequency approximation method called ray theory is implemented. For high frequencies, the pressure field is specified as:

$$U(\mathbf{x}, \omega) = A(\mathbf{x})e^{i\omega T(\mathbf{x})}. \tag{3.9}$$

Here the amplitude of the wave is denoted by A and T is the travel time. This method can only be implemented if the dominant wavelength of the seismic source signal is sufficiently small, i.e. the seismic properties of the model do not alter much over this distance [Cerveny, 2001].

Equation (3.9) is used in the wave equation (3.3) to derive equations for T and A. The derivation follows Cerveny [2001]. The source term is set to zero in the Helmholtz equation:

$$\nabla^2 U(\mathbf{x}, \omega) - \frac{\omega^2}{c^2(\mathbf{x})}U(\mathbf{x}, \omega) = 0. \tag{3.10}$$

For simplicity, independent variables such as $(\mathbf{x}, \omega)$ are left out in the rest of the derivation. Equation (3.9) is subsequently inserted into equation (3.10). For this it is necessary to compute $\nabla^2 U$. First ∇U is computed:

$$\nabla U = (\nabla A)e^{i\omega T} + i\omega A(\nabla T)e^{i\omega T}. \tag{3.11}$$

Now $\nabla^2 U$ is given by:

$$\nabla^2 U = (\nabla^2 A + 2i\omega(\nabla A)\cdot(\nabla T) + i\omega A(\nabla^2 T) - \omega^2 A(\nabla T)^2)e^{i\omega T}. \tag{3.12}$$

Finally, the obtained value for the Laplacian of the pressure field (3.12) and the initial assumption of U (3.9) are inserted into the Helmholtz equation (3.10):

$$(\nabla^2 A + 2i\omega(\nabla A)\cdot(\nabla T) + i\omega A(\nabla^2 T) - A\omega^2(\nabla T)^2)e^{i\omega T} = \frac{\omega^2}{c^2}Ae^{i\omega T}. \tag{3.13}$$

Dividing both sides of the equation by $\omega^2 Ae^{i\omega T}$ and rearranging the terms yields:

$$0 = -\frac{\nabla^2 A}{A\omega^2} - \frac{i}{\omega}(2(\nabla A)\cdot(\nabla T)\frac{1}{A} - \nabla^2 T) + ((\nabla T)^2 - \frac{1}{c^2}). \tag{3.14}$$

For high frequencies the first term on the right-hand side of equation (3.14) goes to zero. Setting the second term in (3.14) equal to zero yields the transport equation:

$$2\nabla A \cdot \nabla T - A\nabla^2 T = 0. \tag{3.15}$$

The third term yields the eikonal equation:

$$(\nabla T)^2 = \frac{1}{c^2}. \tag{3.16}$$

The eikonal equation is characterized as a first order non-linear partial differential equation. This is the equation that needs to be solved in order to determine travel time T. This equation is the starting point for ray tracing and is described in more detail in the section 3.5. Once the travel time T is known, the amplitude A can be determined using equation (3.15). Due to the fact that it is not needed for travel time tomography, it will not be discussed in greater detail.

3.5   Ray Tracing

Figure 3.1 shows wavefronts and rays for a medium containing a high velocity region. The rays are perpendicular to the wavefronts. Studying wave propagation by means of ray paths provides insights into the behaviour of seismic waves. In ray theory, rays are defined as characteristics of the eikonal equation (3.16). This entails that the solution to the eikonal equation (3.16), which is an equation describing wavefronts, can be found by solving a set of ordinary differential equations (e.g. Cerveny [2001]). These equations are called the ray equations:

$$\begin{aligned} \frac{d\mathbf{x}}{dt} &= c^2 \mathbf{p}, \\ \frac{d\mathbf{p}}{dt} &= -\frac{1}{c}\nabla c, \end{aligned} \tag{3.17}$$

where c is the velocity, $\mathbf{x}$ is the position vector along the ray and $\mathbf{p}$ is the slowness vector. The slowness vector is tangent to the ray path and determines the direction in which the ray is going. Initial conditions for the position vector $\mathbf{x}$, i.e. the source position, and the slowness vector $\mathbf{p}$ are needed to solve the ray equations. These are given as a function of the source position $\mathbf{x}_s$, the velocity at $\mathbf{x}_s$ and take-off angles. The initial condition for the source position is given as:

$$\mathbf{x}(0) = \mathbf{x}_s. \tag{3.18}$$

The initial condition for the slowness vector for 3D ray tracing can be given using spherical coordinates (Figure 3.2) [Cerveny, 2001]:

$$\mathbf{p}(0) = \frac{1}{c(\mathbf{x_s})}(\cos\phi\sin\theta, \sin\phi\sin\theta, \cos\theta). \tag{3.19}$$

Where $\phi \in [0, 2\pi]$ is the azimuth and $\theta \in [0, \pi]$ is the angle from the vertical to the ray path (Figure 3.2). These parameters are also called the take-off angles.

One of the reasons why solving equation (3.17) is preferred over equation (3.1) (or equation (3.3)), is that it is much easier.
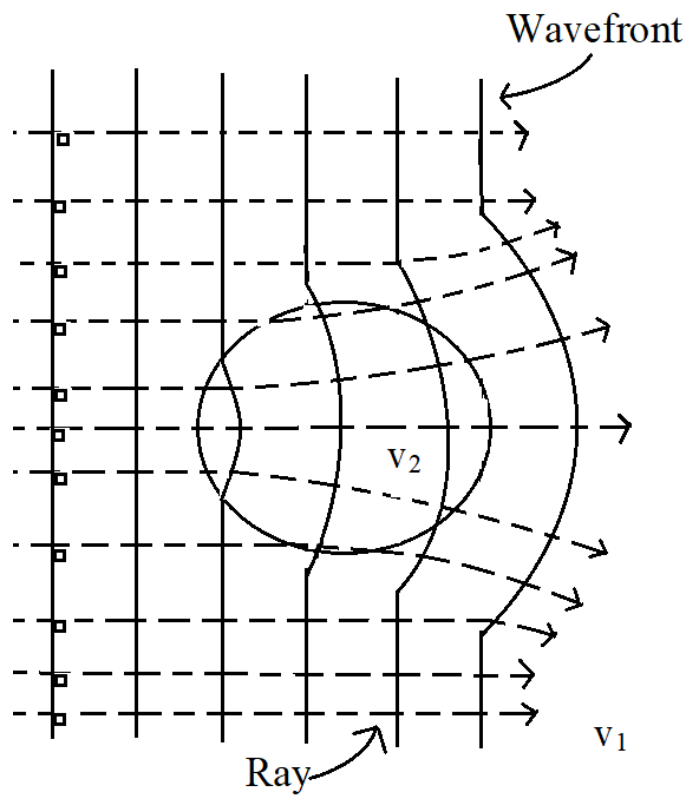
Figure 3.1: An illustration of how seismic wavefronts and rays are connected. Rays are perpendicular to the wavefronts. The wavefronts propagate through a high velocity area ($v_2 > v_1$) which causes the plane wavefronts to become irregular.
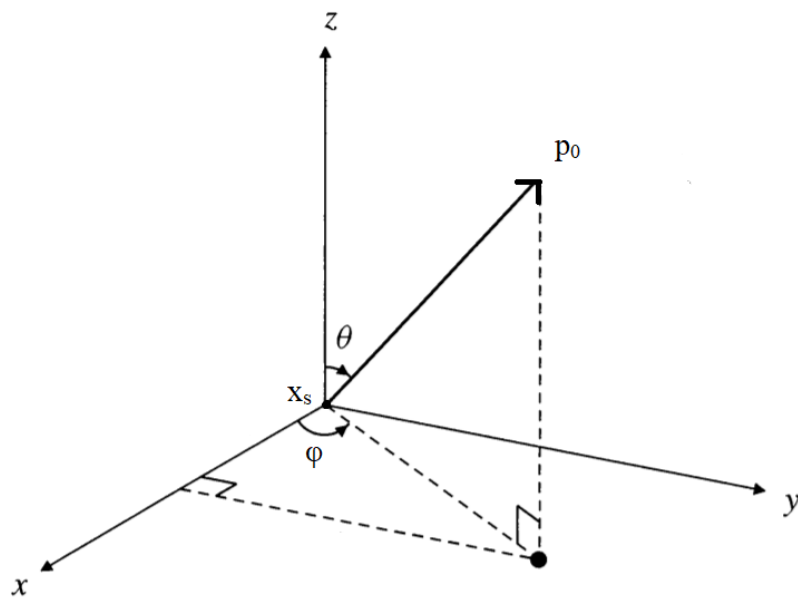
Figure 3.2: Schematics of the initial condition for slowness $\mathbf{p}_0$ in spherical coordinates in 3D.

3.6   Numerical Solution of the Ray Equations

Ray tracing involves solving a set of ordinary differential equations (3.17):

$$\frac{d\mathbf{x}}{dt} = c^2\mathbf{p},$$
$$\frac{d\mathbf{p}}{dt} = -\frac{1}{c}\nabla c, \tag{3.20}$$

where the velocity c is a function of $\mathbf{x}$. Initial conditions for each equation in the system are needed in order to solve it. They were mentioned in section 3.5 (equations (3.18) and (3.19)).

The ray equations (3.20) can be solved numerically:

$$\frac{\mathbf{x}_{i+1} - \mathbf{x}_i}{\Delta t} = c^2(\mathbf{x}_i)\mathbf{p}_i,$$
$$\frac{\mathbf{p}_{i+1} - \mathbf{p}_i}{\Delta t} = -\frac{1}{c(\mathbf{x}_i)}\frac{\partial c(\mathbf{x}_i)}{\partial \mathbf{x}}. \tag{3.21}$$

The unknowns are $\mathbf{x}_{i+1}$ and $\mathbf{p}_{i+1}$, and they are found after rearranging terms in equation (3.21):

$$\mathbf{x}_{i+1} = c^2(\mathbf{x}_i)\mathbf{p}_i\Delta t + \mathbf{x}_i,$$
$$\mathbf{p}_{i+1} = -\frac{1}{c(\mathbf{x}_i)}\frac{\partial c(\mathbf{x}_i)}{\partial \mathbf{x}}\Delta t + \mathbf{p}_i. \tag{3.22}$$

This can be written in discretized form as:

$$x_{i+1} = c^2(\mathbf{x}_i)p_{i,x}\Delta t + x_i,$$
$$y_{i+1} = c^2(\mathbf{x}_i)p_{i,y}\Delta t + y_i,$$
$$z_{i+1} = c^2(\mathbf{x}_i)p_{i,z}\Delta t + z_i,$$
$$p_{i+1,x} = -\frac{1}{c(\mathbf{x}_i)}\frac{\partial c(\mathbf{x}_i)}{\partial x}\Delta t + p_{i,x},$$
$$p_{i+1,y} = -\frac{1}{c(\mathbf{x}_i)}\frac{\partial c(\mathbf{x}_i)}{\partial y}\Delta t + p_{i,y}, \tag{3.23}$$
$$p_{i+1,z} = -\frac{1}{c(\mathbf{x}_i)}\frac{\partial c(\mathbf{x}_i)}{\partial z}\Delta t + p_{i,z}.$$

The set of equations (3.22) is the simplest numerical solution to the ray equations (3.20). This method is called the standard Euler method [Sauer, 2014]. In this thesis, a method called symplectic Euler is implemented to numerically solve the ray equations (3.20). The only difference between it and the standard Euler method

is that $\mathbf{x}_{i+1}$ is used instead of $\mathbf{x}_i$ in the equation for the slowness vector $\mathbf{p}$ in equation (3.22). This gives:

$$\mathbf{x}_{i+1} = c^2(\mathbf{x}_i)\mathbf{p}_i\Delta t + \mathbf{x}_i,$$
$$\mathbf{p}_{i+1} = -\frac{1}{c(\mathbf{x}_{i+1})}\frac{\partial c(\mathbf{x}_{i+1})}{\partial \mathbf{x}}\Delta t + \mathbf{p}_i. \tag{3.24}$$

It can be shown that this is more accurate than equation (3.22) [Niiranen, 1999].

3.7 One- & Two-Point Ray Tracing

The numerical method outlined in the previous sections are used to do one-point ray tracing, i.e. to trace rays from a source in a certain direction specified by the take-off angles. An example of this is given in Figure 3.4, which is based on the 3D velocity model in Figure 3.3.
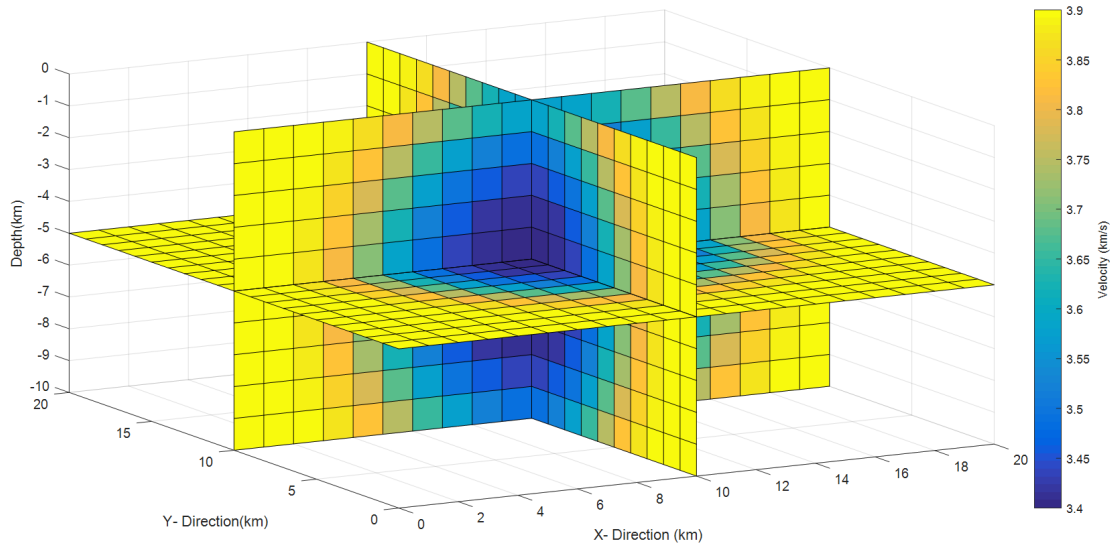
Figure 3.3: The 3D velocity model used for one-point ray tracing. This model has a low velocity area in its center of it which was generated by a generalization of the Gaussian velocity formula.

As opposed to one-point ray tracing, the goal of two-point ray tracing is to compute the ray path that connects the source (hypocenter) and receiver location (seismic station location on surface). This is more complicated since the take-off angles are unknown.

One way of conducting two-point ray tracing involves computing the ray paths for a series of take-off angles, i.e. first doing one-point ray tracing for a lot of rays. This is shown in Figure 3.4 where each location on the surface (blue triangles) indicates the position of a seismic station. All of them have their own associated take-off angles and can therefore be used in a triangulation (see Figure 3.5).

The receiver location for which it is desirable to find the two-point ray path can be used by finding the triangle that encloses this receiver. Once that is done, the next step is to use interpolation to estimate the take-off angles of that receiver. In this thesis, linear interpolation is applied. If necessary, one-point ray tracing is performed for the estimated take-off angles and the two-point ray tracing through
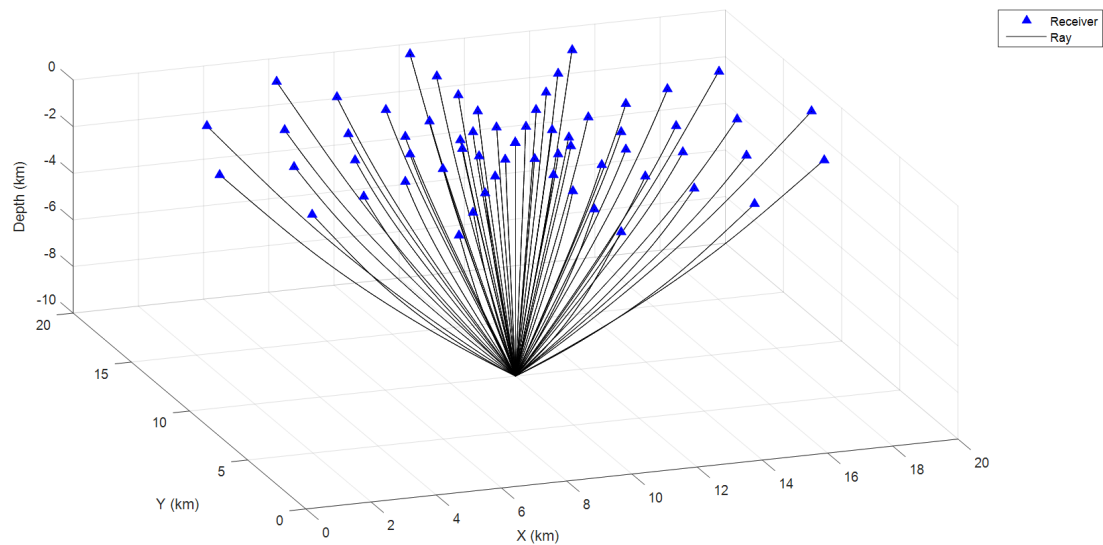
Figure 3.4: An illustration of one-point ray tracing for a series of take-off angles for the 3D velocity model in Figure 3.3. Symplectic Euler is the implemented numerical method. In this figure the source is located at (x, y, z)=(10, 10,-10), while the receivers are on the surface (x, y, 0) and are marked by blue triangles.
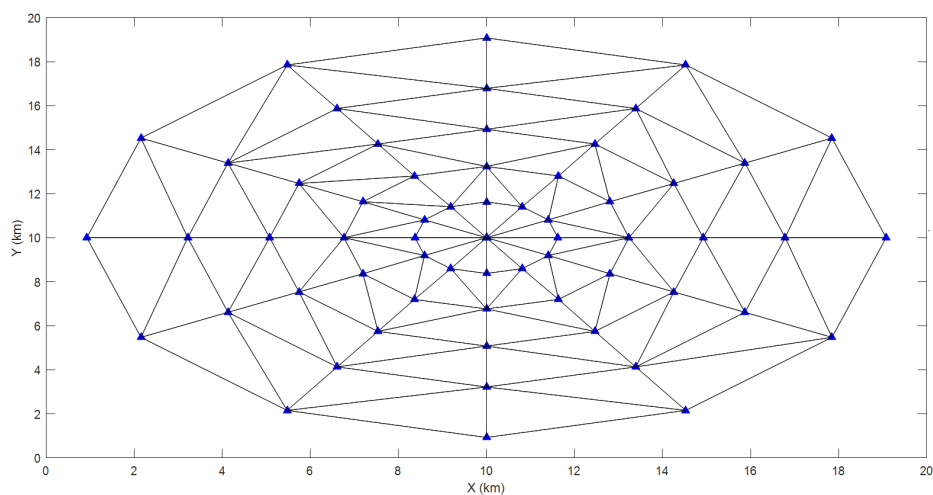
Figure 3.5: An illustration of a triangulation on the surface. The blue triangles are receiver locations with known take-off angles.

interpolation is repeated. The correct trajectory is found if the computed ray path receiver location is in close proximity to the real receiver location.

3.8 The Elastic Wave Equation

In the previous sections ray tracing through an acoustic medium, i.e. a medium that is gaseous or liquid, was discussed. Since the Earth is solid, elastic wave propagation is needed. Elastic wave propagation is therefore briefly presented in this section. It is shown that for elastic isotropic waves ray tracing is very similar to acoustic ray tracing.

The derivation of the elastic wave equation follows [Pujol, 2003]. The equation of motion can be derived from Newtons 2nd law of motion (see e.g. [Pujol, 2003]). It is given by:

$$\nabla \mathbf{T} = \rho \ddot{\mathbf{u}} - \mathbf{f}. \tag{3.25}$$

Here $\mathbf{T}$ denotes the stress tensor, ρ the density, $\ddot{\mathbf{u}}$ the acceleration vector and $\mathbf{f}$ the source function.

Deformation of a solid occurs when external forces are applied to it. It is considered elastic if it is temporary, i.e. the deformation goes to zero when the applied forces are removed. For small deformations, the strain is linearly proportional to stress. This is known as Hooke's law:

$$T_{ij} = c_{ijkl} S_{kl}. \tag{3.26}$$

With i, j, k, l equal to 1, 2 or 3. Here T_{ij} are the components of the stress tensor, S_{kl} of the strain tensor and c_{ijkl} of the elastic stiffness tensor $\mathbf{c}$. The components of the elastic stiffness tensor for an isotropic medium are given by:

$$c_{ijkl} = \lambda \delta_{ij} \delta_{kl} + \mu (\delta_{ik} \delta_{jl} + \delta_{il} \delta_{jk}). \tag{3.27}$$

Here λ and μ are Lamé's parameters which describe the elastic properties of the medium, and δ_{ij} is the Kronecker delta:

$$\delta_{ij} = \begin{cases} 1 & \text{if } i = j, \\ 0 & \text{if } i \neq j. \end{cases} \tag{3.28}$$

The relationship between strain and displacement is given by:

$$S_{kl} = \frac{1}{2} \left(\frac{\partial u_k}{\partial x_l} + \frac{\partial u_l}{\partial x_k} \right). \tag{3.29}$$

Using the expression for strain (3.29) in Hooke's law (3.26) and inserting it in the left-hand side of the equation of motion (3.25) yields the elastic wave equation:

$$\rho \ddot{u}_i = \partial_j (c_{ijkl} \partial_k u_l) + f_i. \tag{3.30}$$

In the frequency domain this is equivalent to:

$$\rho\omega^2 u_i + \partial_j(c_{ijkl}\partial_k u_l) = -f_i. \tag{3.31}$$

The elastic wave equation is a linear second order partial differential equation. It can be solved for the displacement vector $\mathbf{u}$, given the density ρ, source function $\mathbf{f}$ and elasticity tensor $\mathbf{c}$. An analytical solution for this equation can be found if the medium is homogeneous and isotropic. If however it is heterogeneous, then this is not possible and numerical approximation methods are needed [Pujol, 2003].

As in the acoustic case, ray theory can be applied to solve the isotropic elastic wave equation. This is when one seeks solutions of the form:

$$\mathbf{u}(\mathbf{x}, \omega) = \mathbf{A}(\mathbf{x})e^{i\omega T(\mathbf{x})}. \tag{3.32}$$

For simplicity, independent variables such as $(\mathbf{x}, \omega)$ are left out in the rest of the derivation. Using equation (3.32) and the value for the elastic stiffness tensor in an isotropic medium (3.27) in the elastic wave equation (3.31), gives for higher order ω [Nolet, 2008]:

$$-\mathbf{A} + \frac{(\lambda + \mu)}{\rho}\nabla T(\nabla T \cdot \mathbf{A}) + \frac{\mu}{\rho}|\nabla T|^2\mathbf{A} = \mathbf{0}. \tag{3.33}$$

If $\mathbf{A}$ and ∇T are parallel, then equation (3.33) yields:

$$|\nabla T|^2 = \frac{\rho}{\lambda + 2\mu}. \tag{3.34}$$

The velocity of the P-wave is given by $\sqrt{\frac{\lambda + 2\mu}{\rho}}$. This means that the right-hand side of equation (3.34) is equal to $1/c_p^2$. Equation (3.34) is therefore the eikonal equation for the P-wave in an isotropic heterogeneous medium.

If $\mathbf{A}$ and ∇T are perpendicular, on the other hand, then equation (3.33) gives:

$$|\nabla T|^2 = \frac{\rho}{\mu}. \tag{3.35}$$

The velocity of the S-wave is given by $\sqrt{\frac{\mu}{\rho}}$. As a result, the right-hand side of equation (3.35) is equal to $1/c_s^2$. Equation (3.35) is thus the eikonal equation for the S-wave in an isotropic heterogeneous medium.

Based on the equations for the P-wave, it is also observable that the eikonal equation for it is the same in acoustic and elastic media, as will therefore ray tracing. In this thesis only the P-waves are considered. As a consequence the ray equations from section 3.6 are solved for c equal to c_p.

Chapter 4

Theory: Inversion

4.1 Overview

In this chapter, sections 4.2-4.4 consider the general ideas and theory underlying inverse problems. This includes solving nonlinear inverse problems using a grid search and inverse problems by linearization. The former is applied to determine the location of an earthquake in sections 4.5, as well as a uniform starting model for travel time tomography in section 4.7. The linearized problem is implemented in travel time tomography and is considered in section 4.6. A description of the algorithm employed, that renders a solution to the travel time tomography problem is given in section 4.8. This algorithm is applied to various synthetic tests in section 4.9 to confirm that it works and to investigate how different acquisition geometries affect the resolution. Ultimately, in section 4.10 multiscale travel time tomography is introduced. It is also explained how this method is implemented in the work carried out in this thesis.

4.2 Inversion

Inverse modelling is often used in seismology, e.g. to determine the location of earthquakes, their origin time and the velocity model. Inverse modeling involves connecting collected observations $\mathbf{d}$ to some model $\mathbf{m}$. Generally, the relation between $\mathbf{m}$ and $\mathbf{d}$ can be written as:

$$G(\mathbf{m}) = \mathbf{d}. \tag{4.1}$$

Here G is a function which often is quite complicated. Equation (4.1), in principle, is a non-linear problem and therefore often difficult to solve [Aster et al., 2005]. One way of doing this, however, is through using a grid search method. The idea

underlying this approach is to first discretize the model parameters. Afterwards, the forward problem is solved repeatedly, generating data $\hat{\mathbf{d}}$ for each model parameter $\hat{\mathbf{m}}$. A solution to the nonlinear problem is found by locating the model parameter that results in the least amount of misfit, i.e. the model parameter which yields the best overall fit between the observed data $\mathbf{d}$ and the generated data $\hat{\mathbf{d}}$ [Havskov and Ottemöller, 2010].

Grid search is a nonlinear method. It is simple to implement and works well if the number of parameters are limited. It does, however, have some disadvantages. For instance, it can be ineffective when there are too many parameters since this requires a large number of calculations of the forward problem.

Another approach for solving equation (4.1) is linearization and it does not have this limitation. This technique involves seeking a linear approximation to equation (4.1) for the model parameter.

The derivation of the linearized inverse problem given in this thesis follows Stein and Wysession [2003]. The model parameter m_j can be written as the sum of an initial guess $m_{0,j}$ and the changes Δm_j needed in order to make it equal to m_j:

$$m_j = m_{0,j} + \Delta m_j. \tag{4.2}$$

The observed data d_i can be given as:

$$d_i = d_{0,i} + \Delta d_i. \tag{4.3}$$

Here $d_{0,i}$ is the generated data obtained from solving equation (4.1) for $m_{0,j}$, while Δd_i are the changes needed in order to make it equal to the real observations d_i.

Equation (4.3) can be rewritten as:

$$\Delta d_i = d_i - d_{0,i}. \tag{4.4}$$

The generated data $d_{0,i}$ and the observed data d_i can be written in terms of equation (4.1):

$$
\begin{aligned}
d_{0,i} &= \sum_j G_{ij}(m_{0,j}), \\
d_i &= \sum_j G_{ij}(m_{0,j} + \Delta m_j).
\end{aligned}
\tag{4.5}
$$

Using the expressions for $d_{0,i}$ and d_i in equation (4.4) yields:

$$\Delta d_i = \sum_j G_{ij}(m_{0,j} + \Delta m_j) - \sum_j G_{ij}(m_{0,j}). \tag{4.6}$$

A solution to equation (4.6) is found by applying a first order Taylor expansion about the expression for the observed data:

$$\sum_j G_{ij}(m_{0,j} + \Delta m_j) \approx \sum_j G_{ij}(m_{0,j}) + \sum_j \frac{\partial G_{ij}(m_{0,j})}{\partial m_j} \Delta m. \qquad (4.7)$$

Rearranging equation (4.7) gives:

$$\sum_j G_{ij}(m_{0,j} + \Delta m_j) - \sum_j G_{ij}(m_{0,j}) \approx \sum_j \frac{\partial G_{ij}(m_{0,j})}{\partial m_j} \Delta m. \qquad (4.8)$$

Inserting equation (4.8) on the right-hand side of equation (4.6) results in the linearized version of the nonlinear problem (equation (4.1)):

$$\Delta d_i = \sum_j \frac{\partial G_{ij}(m_{0,j})}{\partial m_j} \Delta m_j. \qquad (4.9)$$

In matrix form this is often written as:

$$\mathbf{d} = \mathbf{Gm}. \qquad (4.10)$$

4.3 The Method of Least Squares

The least squares approach can be used to solve the inverse problem (4.10) for $\mathbf{m}$. This involves minimizing the 2-norm of the residuals [Aster et al., 2005]:

$$||\mathbf{r}||_2 = \sqrt{\sum_{i=1}^{n} r_i^2} \, . \tag{4.11}$$

The residual is the difference between the observed data $\mathbf{d}$ and the generated data $\mathbf{Gm}$:

$$\mathbf{r} = \mathbf{d} - \mathbf{Gm}. \tag{4.12}$$

Equation (4.12) is in vector notation and accounts for the fact that the residuals are non-zero. The 2-norm is the sum of the squared residual:

$$\mathbf{r}^T\mathbf{r} = (\mathbf{d} - \mathbf{Gm})^T(\mathbf{d} - \mathbf{Gm}). \tag{4.13}$$

Here $\mathbf{r}^T$ denotes the transpose of $\mathbf{r}$. Equation (4.13) can be written as:

$$\mathbf{r}^T\mathbf{r} = \mathbf{m}^T\mathbf{G}^T\mathbf{Gm} + \mathbf{d}^T\mathbf{d} - \mathbf{m}^T\mathbf{G}^T\mathbf{d} - \mathbf{d}^T\mathbf{Gm}. \tag{4.14}$$

The derivative of equation (4.14) with respect to $\mathbf{m}^T$ gives the minimized 2-norm:

$$\frac{\partial \mathbf{r}^T\mathbf{r}}{\partial \mathbf{m}^T} = \mathbf{G}^T\mathbf{Gm} - \mathbf{G}^T\mathbf{d}. \tag{4.15}$$

Setting this expression equal to zero yields the normal equation [Aster et al., 2005]:

$$\mathbf{G}^T\mathbf{Gm} = \mathbf{G}^T\mathbf{d}. \tag{4.16}$$

Multiplying both sides of the normal equation with the inverse of $\mathbf{G}^T\mathbf{G}$, gives the equation used to find the model parameter:

$$\mathbf{m} = (\mathbf{G}^T\mathbf{G})^{-1}\mathbf{G}^T\mathbf{d}. \tag{4.17}$$

The operator $(\mathbf{G}^T\mathbf{G})^{-1}\mathbf{G}^T$ is often referred to as the generalized inverse of $\mathbf{G}$.

Equation (4.17) can only be solved if all the columns of $\mathbf{G}$ are linearly independent. If this is not the case, however, then singular value decomposition can be employed [Aster et al., 2005].

The concept behind singular value decomposition is that a m by n matrix $\mathbf{G}$ can be written as:

$$\mathbf{G} = \mathbf{USV}^T. \tag{4.18}$$

Here the two matrices $\mathbf{U}$ and $\mathbf{V}$ are both orthogonal. Each column is a unit basis vector that together span the data space and model space, respectively. $\mathbf{U}$ is a m by m matrix and $\mathbf{V}$ is a n by n matrix. The final factor $\mathbf{S}$ is a diagonal matrix of size m by n with elements $S_{i,i}$. The nonzero elements are called the singular values and they are arranged in a decreasing order [Aster et al., 2005]:

$$S_{1,1} >= S_{2,2} >= ... >= 0. \tag{4.19}$$

The generalized inverse of $\mathbf{G}$, denoted by $\mathbf{G}^{-g}$, can be calculated using singular value decomposition. This yields:

$$\mathbf{G}^{-g} = \mathbf{VS}^{-1}\mathbf{U}^T. \tag{4.20}$$

The generalized inverse is also called the pseudoinverse. It can be employed to compute the pseudoinverse solution:

$$\hat{\mathbf{m}} = \mathbf{G}^{-g}\mathbf{d}. \tag{4.21}$$

Using equation (4.20) for the generalized inverse gives:

$$\hat{\mathbf{m}} = \mathbf{VS}^{-1}\mathbf{U}^T\mathbf{d}. \tag{4.22}$$

The inverse of a diagonal matrix is found by computing the reciprocal of the diagonal elements. Therefore:

$$\hat{\mathbf{m}} = \sum_{i=1}^{n} \frac{\mathbf{U}_{.,i}^T \mathbf{d}}{\mathbf{S}_{i,i}} \mathbf{V}_{.,i} . \tag{4.23}$$

The notation $U_{r,c}$ denotes the components of U. The punctuation mark indicates that the whole row r or column c is used.

It is always possible to compute equation (4.17) using singular value decomposition on the generalized inverse of $\mathbf{G}$, since one of its properties is that it always exists. The same will therefore apply to $\hat{\mathbf{m}}$.

A drawback with the generalized inverse solution (equation (4.22)) is that it can be highly unstable if one or more of the singular values are close to zero. The solution can be made more stable if the terms in equation (4.22) that are linked to the small singular values are excluded. This, however, will reduce the resolution and bias the solution. More detailed information regarding this topic can be found in Aster et al. [2005].

4.4 The Method of Tikhonov Regularization

Tikhonov regularization is a technique often employed to stabilize discrete ill-posed problems, as it minimizes the issue associated with small singular values by giving greater weight to larger ones. This is achieved by considering the damped least squares problem [Aster et al., 2005]:

$$\min \|\mathbf{Gm} - \mathbf{d}\|_2^2 + \alpha^2 \|\mathbf{m_0}\|_2^2 \,. \tag{4.24}$$

Where α is a regularization parameter. The aim of the damped least square problem is to minimize the sum of the solution norm and residual norm, i.e. to constrain unneeded features without large compromises regarding the fit of the data [Aster et al., 2005]. The dampened least squares problem (4.24) can be rewritten as:

$$\min \left\| \begin{bmatrix} \mathbf{G} \\ \alpha\mathbf{I} \end{bmatrix} \mathbf{m_0} - \begin{bmatrix} \mathbf{d} \\ \mathbf{0} \end{bmatrix} \right\|_2^2 . \tag{4.25}$$

Where $\mathbf{I}$ is the identity matrix. The argument matrix is non-singular if the regularization parameter is nonzero. Equation (4.25) can thus be solved by the normal equations (4.17). This yields the zeroth-order Tikhonov regularization:

$$(\mathbf{G}^T\mathbf{G} + \alpha^2\mathbf{I})\mathbf{m_0} = \mathbf{G}^T\mathbf{d}. \tag{4.26}$$

Using singular value decomposition on $\mathbf{G}$, equation (4.26) becomes:

$$(\mathbf{VS}^T\mathbf{SV}^T + \alpha^2\mathbf{I})\mathbf{m_0} = \mathbf{VS}^T\mathbf{U}^T\mathbf{d}. \tag{4.27}$$

The solution to equation (4.27) is given by:

$$\mathbf{m}_{0,\alpha} = \sum_{i=1}^{k} \frac{\mathbf{S}_{i,i}^2}{\mathbf{S}_{i,i}^2 + \alpha^2} \frac{(\mathbf{U}_{.,i})^T\mathbf{d}}{\mathbf{S}_{i,i}} \mathbf{V}_{.,i} \,. \tag{4.28}$$

Where k takes the minimum value of the dimensions of matrix $\mathbf{S}$. The term $\mathbf{S}_{i,i}^2/(\mathbf{S}_{i,i}^2 + \alpha^2)$ is referred to as the filter factors. The filter factors are close to one if the singular value is much larger than α, and close to zero if it is much smaller than α. Consequently, the problem associated with small singular values are minimized [Aster et al., 2005].

The best value of α is determined by using a trade-off curve. This curve is visualized by plotting the residual norm versus the solution norm (Figure 4.1). Increasing the value of α will generate decreasing and increasing values of the solution norm and residual norm, respectively. The curve will as a result often have a characteristic L shape. The most optimal value of α is chosen as the corner of the L-curve, since this will minimize the solution norm and the residual norm (red star in Figure 4.1) [Aster et al., 2005].
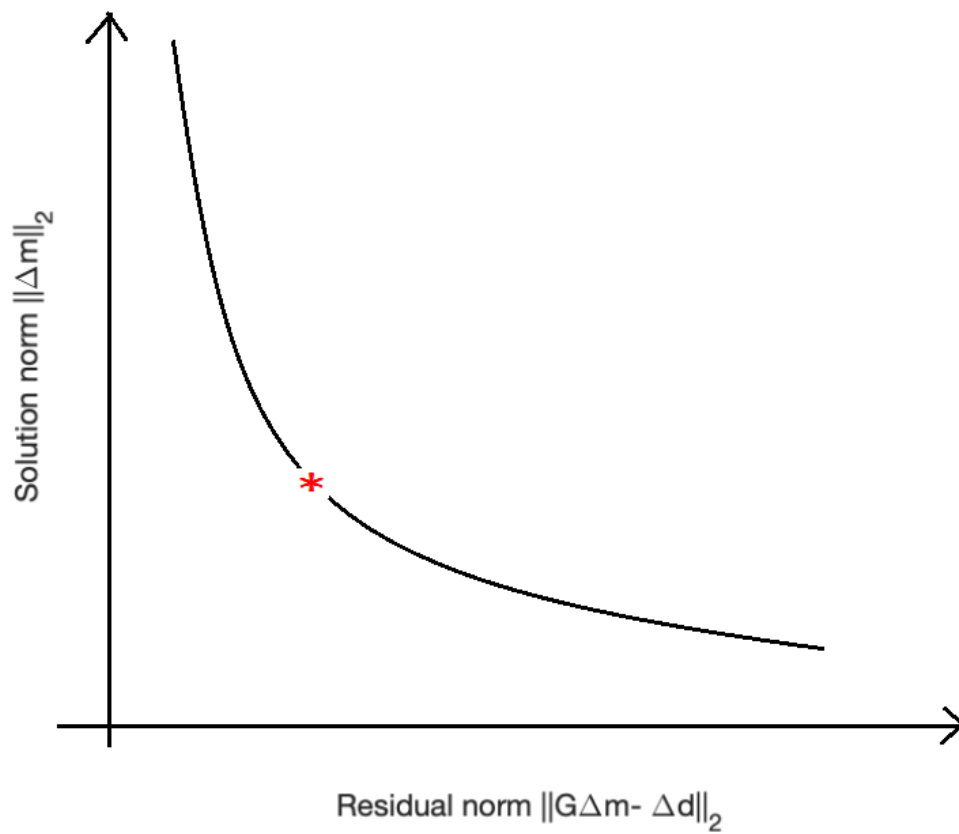
Figure 4.1: An illustration of a L-curve. The x-axis is the residual norm and the y-axis is the solution norm. The red star marks the location that has the best damping value.

4.5 Grid Search for Earthquake Location

In this section the problem of determining the location of earthquakes and their origin time are discussed. Two things are needed in order to estimate these values: the arrival times of body waves and the local velocity model. Arrival times can be read from seismic data and are characterized as:

$$T = t(\mathbf{x}, \mathbf{r}) + t_0. \tag{4.29}$$

Here t is the travel time from a source located at $\mathbf{x}$ to a receiver located at $\mathbf{r}$, and t_0 is the origin time of the seismic event.

A method frequently employed to determine the location of an earthquake is a systematic grid search over all possible locations. This approach is computationally demanding. Advancements in computer power, however, have made carrying it out more practical [Lomax et al., 2009].
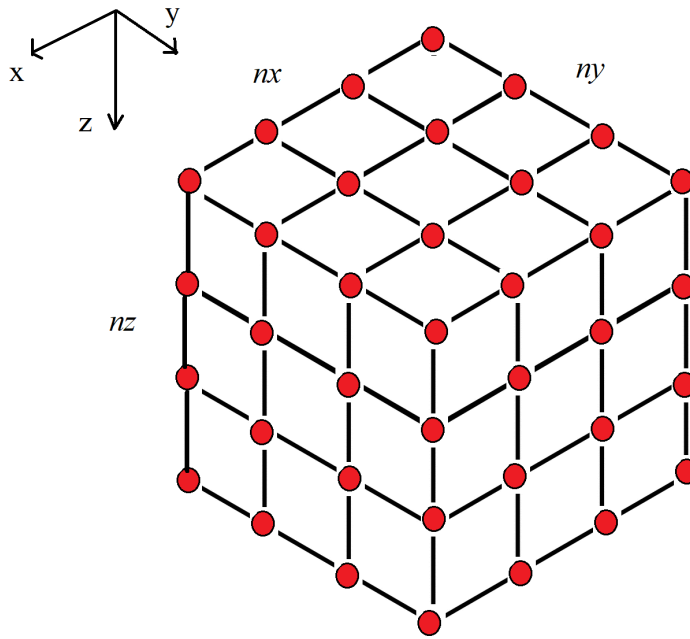
Figure 4.2: An illustration of how the subsurface is divided into a grid to find earthquake locations. The red circles are grid points, i.e. possible earthquake locations. This illustration consists of $nx \times ny \times nz = 4 \times 4 \times 4$ grid points in total.

The area where the earthquakes are assumed to originate from is divided into $N = nx \times ny \times nz$ theoretical grid points (Figure 4.2). Some form of misfit is required

in order to evaluate which location is the most likely. In order to do this, the least squares approach is frequently implemented. This approach refers to when the misfit M for a trial earthquake location $\mathbf{x}$ is given by the sum of the squared residuals r [Havskov and Ottemöller, 2010]:

$$M(\mathbf{x}) = \sum_{i=1}^{n_r} r_i(\mathbf{x})^2. \tag{4.30}$$

Here n_r is the number of receivers that have recorded the earthquake. The residual is given as the difference between the observed arrival time and the calculated arrival time:

$$r_i(\mathbf{x}) = T_i^{obs} - T_i^{cal}(\mathbf{x}). \tag{4.31}$$

The observed arrival time $T_i^{obs}(\mathbf{x})$ can be selected from seismic waveform data. The calculated arrival time $T_i^{cal}(\mathbf{x})$, on the other hand, is the sum of the origin time and the travel time of a seismic wave propagating from the source located at $\mathbf{x}$ to the receiver where T^{obs} was selected[1].

The misfit is calculated for each grid location (equation (4.30)). Generally, the most probable location for an earthquake is where the overall fit between the observed arrival time and calculate arrival time is best, i.e. the location with least misfit.

In this thesis a new method named P-wave single difference is implemented to determine earthquake location. Following this approach, rays are traced from the theoretical grid point $\mathbf{x}$ to the receiver where arrival times have been selected. This is equal to what is done when using the least squares approach. In contrast to the least squares approach which needs the computed arrival times T^{cal}, however, this method only requires the computed travel time of the rays t^{cal}. Before the misfit is computed, furthermore, the observed arrival times T^{obs} and calculated travel times t^{cal} are separated for an additional computation where the difference between the receiver pairs $l = 1 \dots m$ is calculated:

$$\begin{aligned} \delta T_l^{obs} &= T_i^{obs} - T_j^{obs} && \text{for } i \neq j, \\ \delta t_l^{cal}(\mathbf{x}) &= t_i^{cal}(\mathbf{x}) - t_j^{cal}(\mathbf{x}) && \text{for } i \neq j. \end{aligned} \tag{4.32}$$

Here i and j denote the index of the receiver and $i \in [1, n_r - 1]$ and $j \in [2, n_r]$. In turn, the misfit is given as the sum of the squared difference between δT^{obs} and δt^{cal}:

$$M(\mathbf{x}) = \sum_{l=1}^{m} (\delta T_l^{obs} - \delta t_l^{cal}(\mathbf{x}))^2. \tag{4.33}$$

---

[1]As explained in chapter 3, travel times are computed using ray tracing in this thesis.

The hypocentre is at the location $\mathbf{x}$ where the misfit has the lowest value.

An advantage with P-wave single difference is that knowledge of the origin time of the seismic event is not required to find a location. In fact, this parameter can be estimated after determining the earthquake location.

An earthquake detected by n_r receivers will have n_r equations of (4.29). Consequently, the origin time can be computed by solving equation (4.29) for t_0 and averaging the n_r values:

$$t_0 = \frac{1}{n_r} \sum_{i=1}^{n_r} (T_i^{obs} - t_i(\mathbf{x}, \mathbf{r})). \tag{4.34}$$

Since in this thesis the origin time is not needed to determine earthquake locations, it is not computed.

The reason why grid search is applied to determine earthquake locations in this thesis, is that when it is used it is possible to calculate the misfit for a number of locations and choose the location with the least misfit. When linearized inversion is employed, on the other hand, only one location is determined. The misfit of the surrounding locations is therefore unknown. Furthermore, an inversion can also fail to find the best location if the initial guess of the hypocenter is not close enough to the real location [Lomax et al., 2009].

4.6   Linear Equation & its Application to Travel Time Tomography

The idea behind travel time tomography is that a three-dimensional distribution of the subsurface velocity can be found by integrating along a number of rays propagating through the subsurface [Bording et al., 1987]. In this thesis the ray equations are solved numerically using the symplectic Euler method (described in chapter 3).

The travel time associated with a given seismic ray is the integral of slowness, i.e. the reciprocal of the velocity c, along the ray path l. The slowness changes based on its position throughout the medium. Thus, the travel time of a ray is given as:

$$t = \int \frac{1}{c} dl. \tag{4.35}$$

Solving for c if t is given is difficult because it is a nonlinear problem; the ray path of the seismic ray depends on the unknown velocity. Section 4.2 introduced the idea that this type of problem, i.e. a nonlinear problem, can be solved by linearization about the model parameter $\mathbf{m}$. In travel time tomography, the model parameter is a starting velocity model $\mathbf{c_0}$. The principle behind travel time tomography is thus that one starts out with a guess of the background velocity model $\mathbf{c_0}$. One then determines the changes in velocity, $\mathbf{\Delta c}$, that need to be added to the background model in order to make it as close as possible to the real velocity model $\mathbf{c}$.
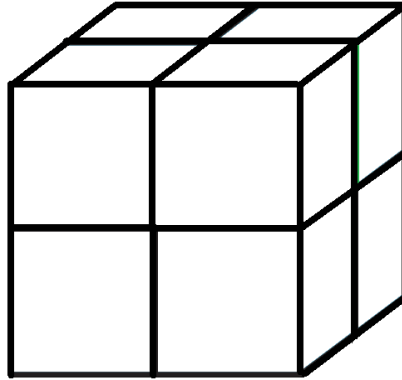

Figure 4.3: An illustration of a block structure which consists of 8 cells. Each of the cells have a uniform velocity.

The background velocity model is a rough estimate of what is believed to be the subsurface structure. Nonetheless, knowledge regarding the subsurface structure actually tends to be limited. For this reason, it is typically smooth and does not have many features.

The background velocity is modeled as a block structure in this thesis. An illustration of a block structure is shown in Figure 4.3. All the blocks are uniform in size. A single block is called a cell and the velocity is constant within it.

4.6.1 Derivation of the Linearized Inverse Problem

The linearized inverse problem is derived in order to find an expression for the function parameter $\mathbf{G}$. The difference in travel time is given by:

$$\Delta t = t^{obs} - t^{cal}. \tag{4.36}$$

The equation for the travel time of a ray (4.35) is used in equation (4.36). This yields:

$$\Delta t = \int \frac{1}{c} dl - \int \frac{1}{c_0} dl_0. \tag{4.37}$$

Here c and c_0 are the real and initial guesses of velocity of the medium in which the ray propagates through, respectively. It is assumed that the ray through c is the same as the ray through c_0. In this case:

$$\Delta t = \int \left[\frac{1}{c} - \frac{1}{c_0} \right] dl. \tag{4.38}$$

The real velocity can be written as the sum of the initial guess and the changes in velocity required to make it equal to the real velocity:

$$c = c_0 + \Delta c. \tag{4.39}$$

The expression for the real velocity (4.39) is used in (4.38), and the terms are rearranged:

$$\Delta t = \int \left[\frac{1}{c_0} \frac{1}{1 + \frac{\Delta c}{c_0}} - \frac{1}{c_0} \right] dl. \tag{4.40}$$

Taylor's theorem is applied to the non-linear factor containing Δc in equation (4.40):

$$\frac{1}{1 + \frac{\Delta c}{c_0}} \approx 1 - \frac{\Delta c}{c_0}. \tag{4.41}$$

Inserting the linear approximation (4.41) into (4.40) yields:

$$\Delta t = - \int \frac{1}{(c_0)^2} dl \Delta c. \tag{4.42}$$

The discretized form of equation (4.42) for travel time Δt for ray i is:

$$\Delta t_i = - \sum_{j=1}^{n_c} \frac{L_{ij}}{(c_{0,j})^2} \Delta c_i.$$ (4.43)

Here n_c is the number of cells the background velocity model consists of, i is the index for the ray, L_{ij} is the distance traveled by ray i in cell j and $c_{0,j}$ is the velocity in cell j in the background model (Figure 4.4).
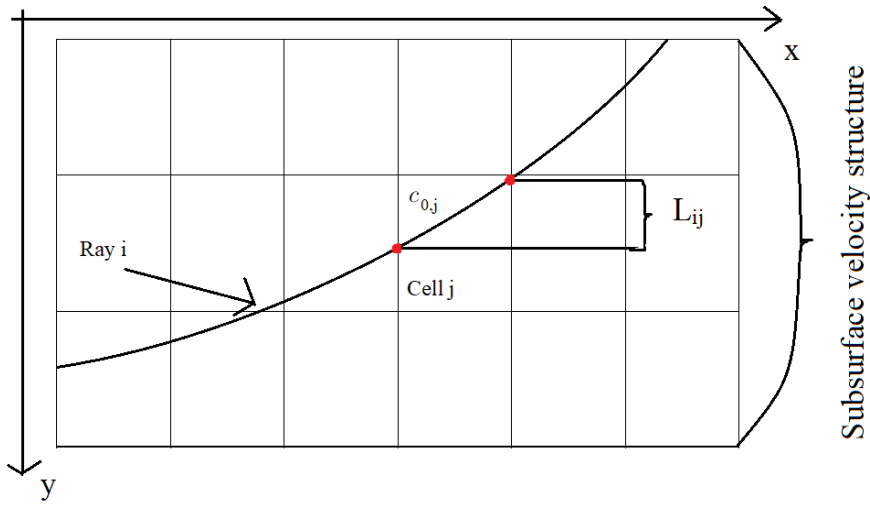
Figure 4.4: A 2D illustration of a ray path propagating through the subsurface velocity structure. The velocity structure is discretized into cells. The velocity in each cell is uniform, and the velocity in cell j is given by $c_{0,j}$. The two red dots indicate where the ray intercepts with cell j. The distance traveled in cell j by ray i is denoted by L_{ij}.

Equation (4.43) can be written in vector notation:

$$\mathbf{\Delta t} = \mathbf{G \Delta c}.$$ (4.44)

Equation (4.43) is a problem of the form $\mathbf{d} = \mathbf{Gm}$ (see equation (4.10)), written in terms of the travel time of a ray. It is thus the linearized solution to the nonlinear problem (4.35).

When travel time tomography is solved by linearization, the components of $\mathbf{G}$ are given by:

$$G_{ij} = - \frac{L_{ij}}{(c_{0,j})^2}.$$ (4.45)

The tomography matrix is the same as the function parameter $\mathbf{G}$, and it connects $\mathbf{\Delta c}$ to $\mathbf{\Delta t}$. Each row of the tomography matrix describes the path of a ray propagating from a source to a receiver. The size of the matrix is consequently the number of rays times the number of cells the velocity structure consists of. The tomography matrix will normally have more rows than columns. Moreover, it is usually very sparse. This is due to the fact that a single ray only intersects with a limited number of cells in the velocity model.

In this thesis, equation (4.44) is solved using Tikhonov regularization. This yields:

$$\mathbf{\Delta c}_\alpha = \sum_{i=1}^{k} \frac{\mathbf{S}_{i,i}^2}{\mathbf{S}_{i,i}^2 + \alpha^2} \frac{(\mathbf{U}_{.,i})^T \mathbf{\Delta t}}{\mathbf{S}_{i,i}} \mathbf{V}_{.,i} \, . \tag{4.46}$$

Singular value decomposition is used on the tomography matrix $(\mathbf{G} = \mathbf{USV}^T)$. The index k is equal to the minimum of the dimensions of S, and α is the regularization parameter.

4.7   Flow Chart: Background Model using Grid Search

The data received from the Miravalles geothermal field are used to determine earthquake locations and perform travel time tomography. The purpose of the latter is to image the subsurface structure, as well as obtain a more accurate velocity model for the exact location of earthquakes. In this section the algorithm implemented to determine a constant starting velocity model for the travel time tomography is explained. A flow chart illustrating the main features of the algorithm is shown on p.58. The flow chart consists of four steps and a total of three loops. Each loop has a separate color and is indexed by [1], [2] or [3].

The input for the algorithm are the dimensions of the velocity grid, the grid size, the receiver locations and the selected arrival times.

The first step in the algorithm consists of looping over different velocities (loop [1]). For each velocity, a new uniform test background velocity model is used.

The second step is to relocate the earthquakes for the test background velocity model, employing P-wave single difference described in section 4.5. Determining earthquake locations is accomplished by first looping over the detected earthquakes (loop [2]), before looping over the grid locations (loop [3]). For each grid location the misfit is computed (equation 4.33). Once the loop over the grid locations is complete (loop [3]), the most probable origin of the earthquake is determined to be where the misfit is least. All the earthquakes have been relocated once the loop over the detected earthquakes is done (loop [2]).

The third step is to evaluate the test background model. The overall fit of it is calculated as the mean misfit of all the relocated earthquakes, where the misfit for one earthquake location is computed as in equation (4.33).

The fourth step is to select the best constant background velocity model for the travel time tomography. This can be accomplished once the loop over the velocities is complete (loop [1]). The most optimal constant background velocity model is the constant test background velocity model that gives the smallest amount of misfit.
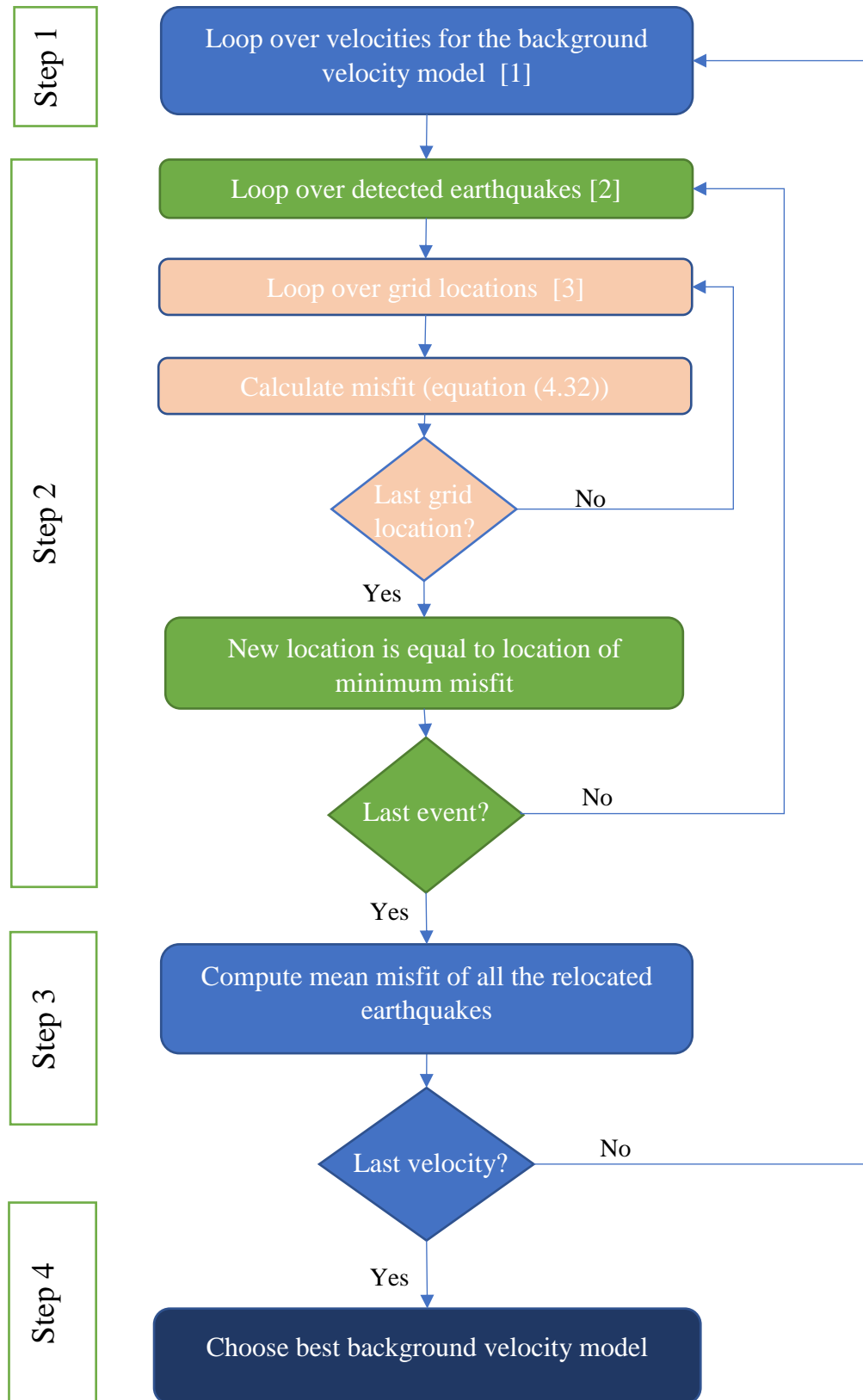
4.8   Flow Chart: Travel Time Tomography

In this section the inversion algorithm used to solve equation (4.44) for $\mathbf{\Delta c}$ through the implementation of Tikhonov regularization is explained. A flow chart illustrating the main features of the algorithm is shown on p.62. The flow chart consists of seven steps and a total of three loops. Each loop has a separate color and is indexed by [1], [2] or [3].

Values for the tomography matrix $\mathbf{G}$, and the difference in observed and calculated travel time $\mathbf{\Delta t}$ are needed in order to solve the linearized inverse problem (equation (4.46)). The purpose of this algorithm is to first compute values for the tomography matrix and the calculated arrival times[2]. This is done by forward modeling through the background velocity model. Afterwards, inversion is performed.

The first step in the algorithm is to loop over all the source-receiver combinations (loop [1]), i.e. rays. This is carried out since arrival times and values for the tomography matrix are required for all rays traveling through the background model. The input data for the loop are the background velocity model, selected arrival time of the detected earthquakes, as well as the associated source and receiver locations.

The second step is to perform one- and two-point ray tracing, described in section 3.7. This gives the set of coordinates $\mathbf{x^{ray}}$ that represents the path of the ray. The straight line that connects two coordinates is called a line segment (Figure 4.6).

The third step is to use the set of coordinates $\mathbf{x^{ray}}$ to find the path length in each cell. The difference between the line segments of the ray path and its length in a cell is observed in Figure 4.7. In order to find the path length in each cell, it is necessary to first find where the ray intersects with the cells in the background velocity model. This information is obtained by performing three separate loops over the line segments which describe the ray path. Each loop finds the intersection between the line segment and one of the three axes of the grid (loop [2]). The corresponding values of the two other coordinates are found with simple geometry. Finally, Pythagoras is employed to compute the length traveled in the cell.

The fourth step is to loop over the path lengths in each cell (loop [3]). Within this loop the midpoint of the path length is calculated. This is used to find the index for the path length that is equal to that of a cell in the background velocity model. Once this has been done, the velocity in the cell is known. Afterwards, the travel time for the path segment in the cell and the value of the tomography matrix is computed (equations (4.29) and (4.45)).

The fifth step is to compute the calculated arrival time T^{cal} (equation (4.29)). This can be accomplished once the loop over the path lengths in each cell is complete

---

[2]It is assumed that values for the observed arrival times are known in this section.
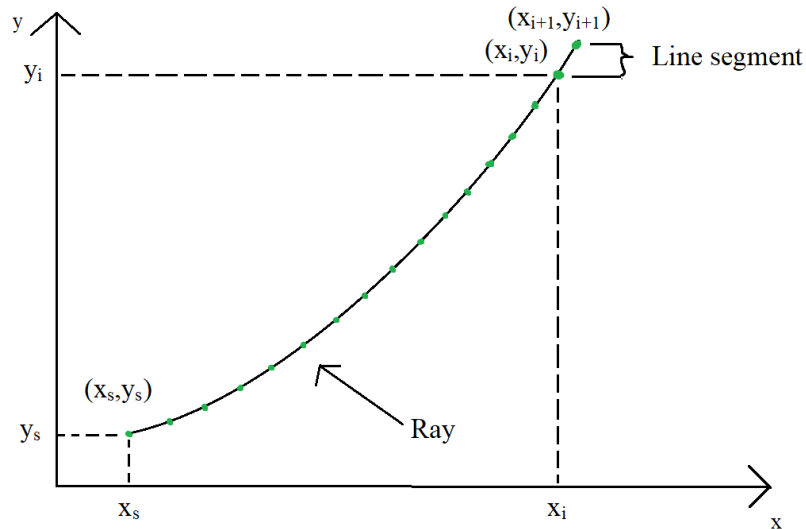
Figure 4.6: A 2D illustration of a ray path. The ray starts at (x_s, y_s) and ends at (x_{i+1}, y_{i+1}). The green dots are the locations of the set of coordinates that describe the ray path. The straight line between the two green dots, i.e. the coordinates that describe the ray path, is a line segment.
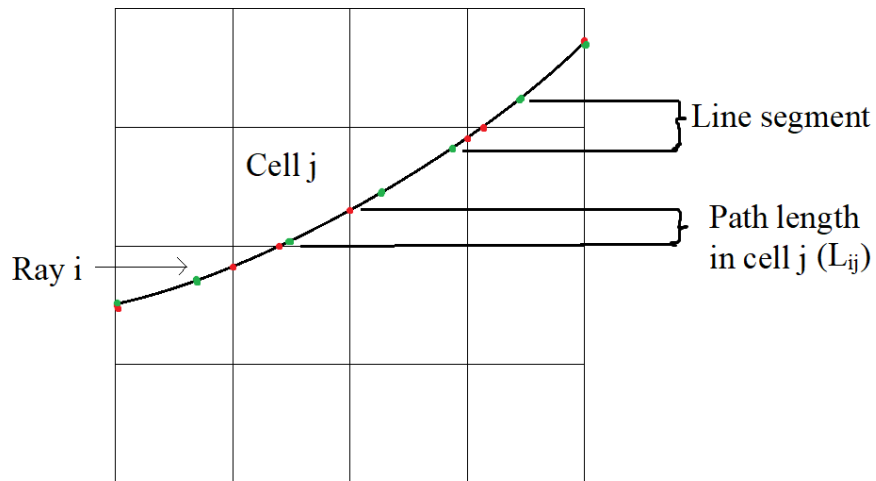
Figure 4.7: A 2D area of the subsurface discretizated into cells, i.e. a representation of the structure of the background velocity model. The figure shows ray i traveling through the structure. The ray path is given by the lines that connect the green dots, while the path length traveled in a cell is given by the line segment that connects the red dots. The length traveled in cell j by ray i is given by L_{ij}.

(loop [3]).

The values for the tomography matrix and the arrival travel time for all the rays traveling through the background velocity model are found once the loop over the source-receiver combinations is finished (loop [1]). Following these five steps, the travel time residual can be computed. All the matrices required to perform the linearized inversion (4.44) are thus generated.

The sixth step in the algorithm is to use singular value decomposition on the tomography matrix $\mathbf{G}$, followed by the implementation of Tikhonov regularization described in section 4.4. This entails that the inversion (equation (4.46)) is first performed for a number of damping values α in the range [0,1]. The best damping value is subsequently decided based on the L-curve.

The seventh and final step consists of performing the linearized inversion on the generated data for the best damping value. This will give the changes in velocity, $\mathbf{\Delta c}$, which should be added to the background velocity model in order for it to converge towards the real velocity model.
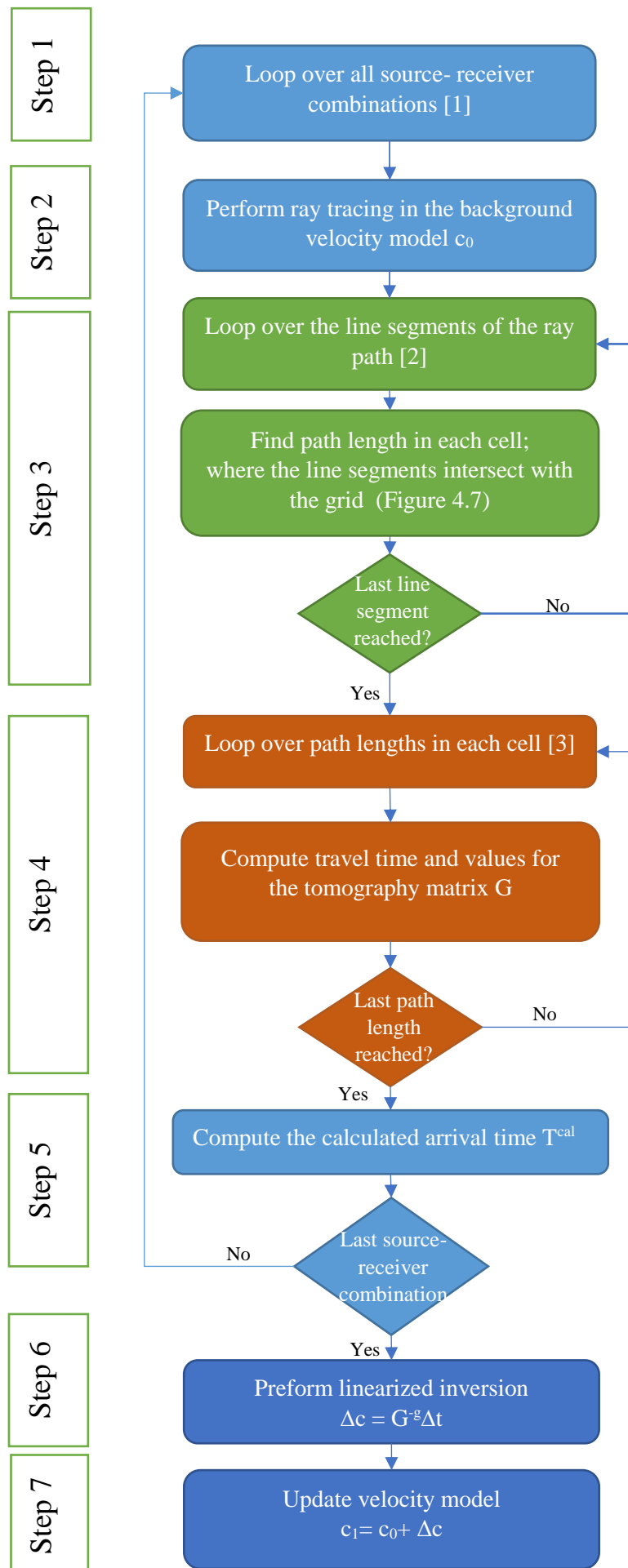
4.9   Tomography: Synthetic Tests

The inversion algorithm introduced in subsection 4.8 is tested on synthetic data before it is applied to the real observed data. This procedure is done in order to validate that it was working properly and to assess how different acquisition geometries affect the resolution.

The difference between applying travel time tomography to real data and synthetically generated data lies in the observed arrival times T^{obs}. When the algorithm is used on real data, the observed arrival times are selected from waveform data in SEISAN. In a synthetic test, however, they are generated by tracing rays through a known input model. The aim of the inversion for a synthetic test is to recover the input model used to generate the observed arrival times.
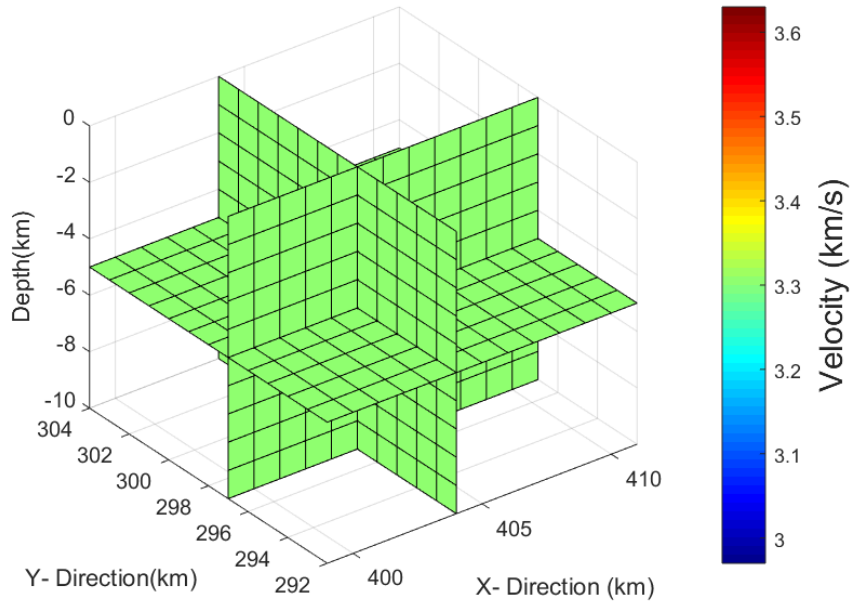
Figure 4.9: The background velocity model employed in all the synthetic tests. The dimensions of the cells are $1 \times 1 \times 1$ km, and the velocity is constant.

In this section the results from two input models and acquisition geometries, i.e. four tests, are discussed. The background velocity model for all four tests is completely homogeneous and consists of $nx \times ny \times nz = 12 \times 12 \times 10$ cells, each of size $l_x \times l_y \times l_z = 1 \times 1 \times 1$ km (Figure 4.9). The two different input models are called input model A and B, and are shown in Figures 4.10 and 4.11, respectively. The synthetic tests that employ input model A to generate data for T^{obs} are called spike tests. The velocity in model A is uniform except for a square in the center which has 10%
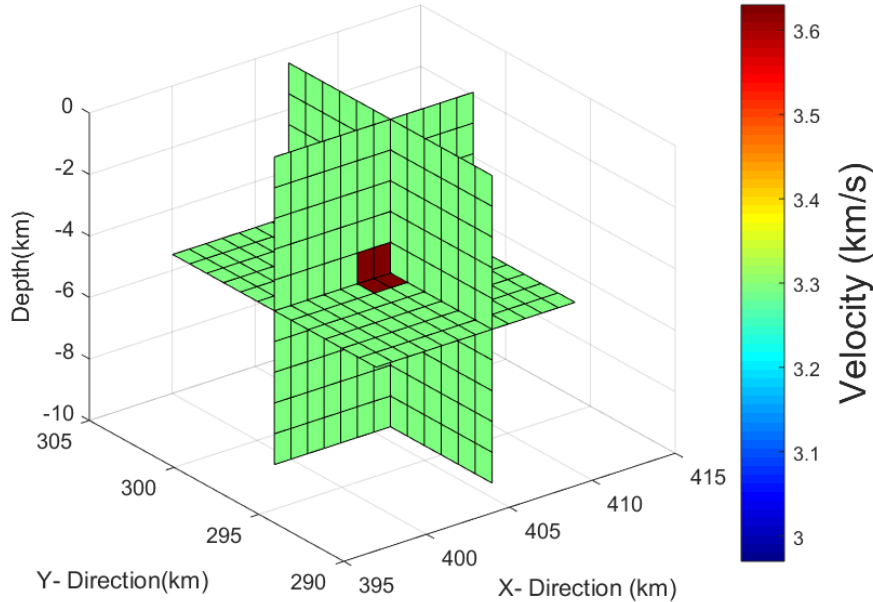
Figure 4.10: The input model used in the spike tests (input model A). The dimensions of the cells are $1 \times 1 \times 1$ km, and the velocity is constant except for a higher velocity area $2 \times 2 \times 2$ km^3 in the center of the model.

higher velocity, i.e. a spike. The synthetic tests that use input model B are called checkerboard tests. The heterogeneous input model for this approach consists of an alternating pattern of positive and negative anomalies of magnitude $\pm 10\%$. Both models have the same block structure as the background model.

The first acquisition geometry consists of evenly spaced receivers, i.e. seismic stations, and earthquakes[3]. The receivers are located on the surface ($z = 0$ km) and the sources at a depth of 10 km. The distribution of sources and receivers in the x- and y-direction is shown in Figures 4.12a and 4.12c; they are all situated in the center of the cells. The dimensions of the grid in the x- and y-directions are 12×12 (in km) cells. This means that the even acquisition geometry consists of 144 sources and 144 receivers. The total number of rays propagating through the background velocity model is therefore $144 \times 144 = 20736$. The acquisition geometry is symmetrical. As a result, the same will apply to the ray coverage (Figure 4.13).

For the second acquisition geometry, named the real acquisition geometry, the locations of the sources are equal to those in the previous case (Figure 4.12c). The receiver positions, however, are equal to those located close to the Miravalles geother-

---

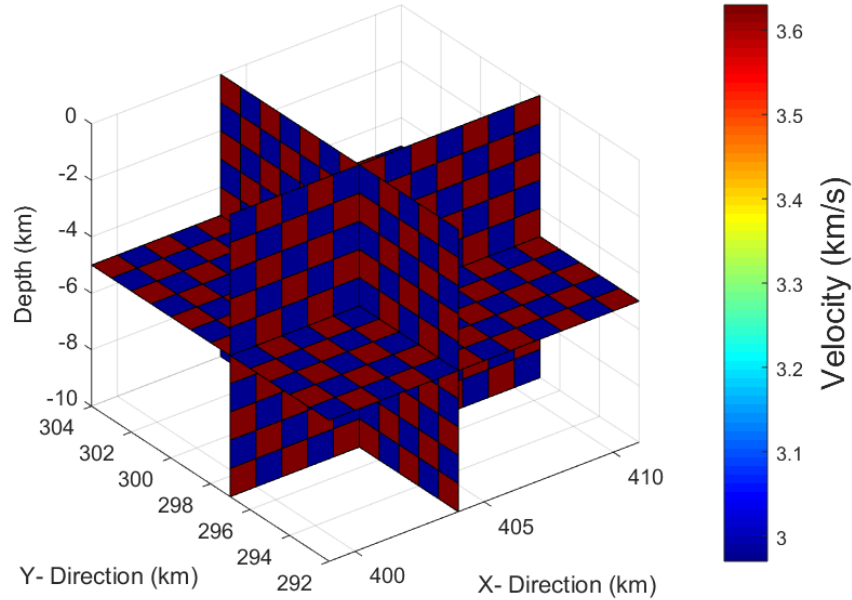[3]These are referred to as "sources" in the rest of this subsection.

Figure 4.11: The heterogeneous input model used in the checkerboard tests (input model B). The dimensions of the cells are $1 \times 1 \times 1$ km, and the velocity alternates with $\pm 10\%$

mal field (Figure 4.12b). This setup has only 9 unevenly spaced receivers, unlike the previous setup which had 144. Consequently, only $9 \times 144 = 1296$ rays are traveling through the velocity models for this acquisition geometry. The ray coverage is shown in Figure 4.14.

The first synthetic test is for input model A (spike test) and the even acquisition geometry. Figure 4.15 shows the relative change in velocity for each layer in the recovered model. The inversion has recovered the structure of input model A. It is also evident from this figure that information about the low velocity area smear into the adjacent blocks, and that the recovered model is symmetrical. Symmetry was expected since the input model and acquisition geometry are symmetrical. This indicates that the applied inversion algorithm is working.

The second synthetic test combines input model A (spike test) with the real acquisition geometry. The relative change in velocity for each layer is shown in Figure 4.16. As expected, the recovered structure of the input model is not as good as for the even setup of sources and receivers. Nonetheless, the high velocity anomaly in the center of input model A is detected. There is smearing of this anomaly into adjacent blocks. This is similar to what occurred with the symmetric setup. The smearing is, however, not symmetrical due to the position of the receivers.
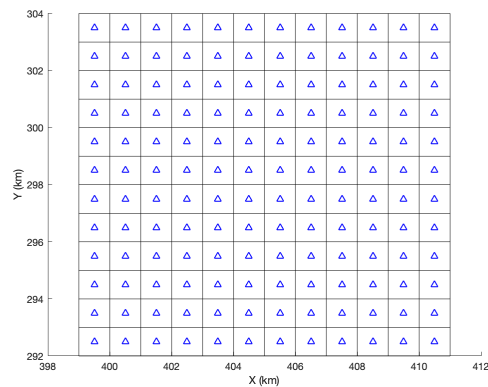
(a) Surface plot of the even acquisition geometry. The blue triangles mark the position of the stations, they are located in the center of the cells.
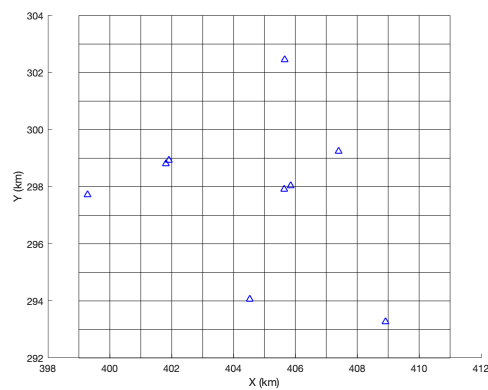
(b) Surface plot of the acquisition geometry at the Miravalles geothermal field, i.e. real acquisition geometry. The blue triangles mark the position of the stations.
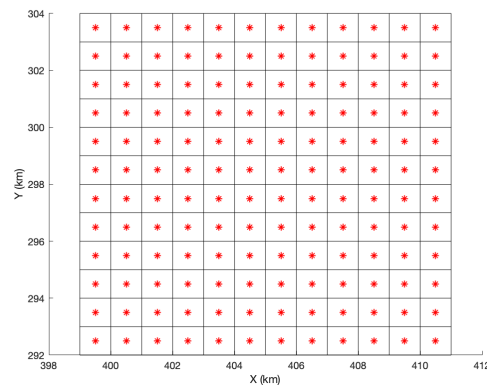
(c) Plot of the evenly spaced sources. They are marked by red stars and located at 10 km depth.

Figure 4.12: Plots of the two different acquisition geometries (even and real) and the locations of the sources used in the synthetic tests.
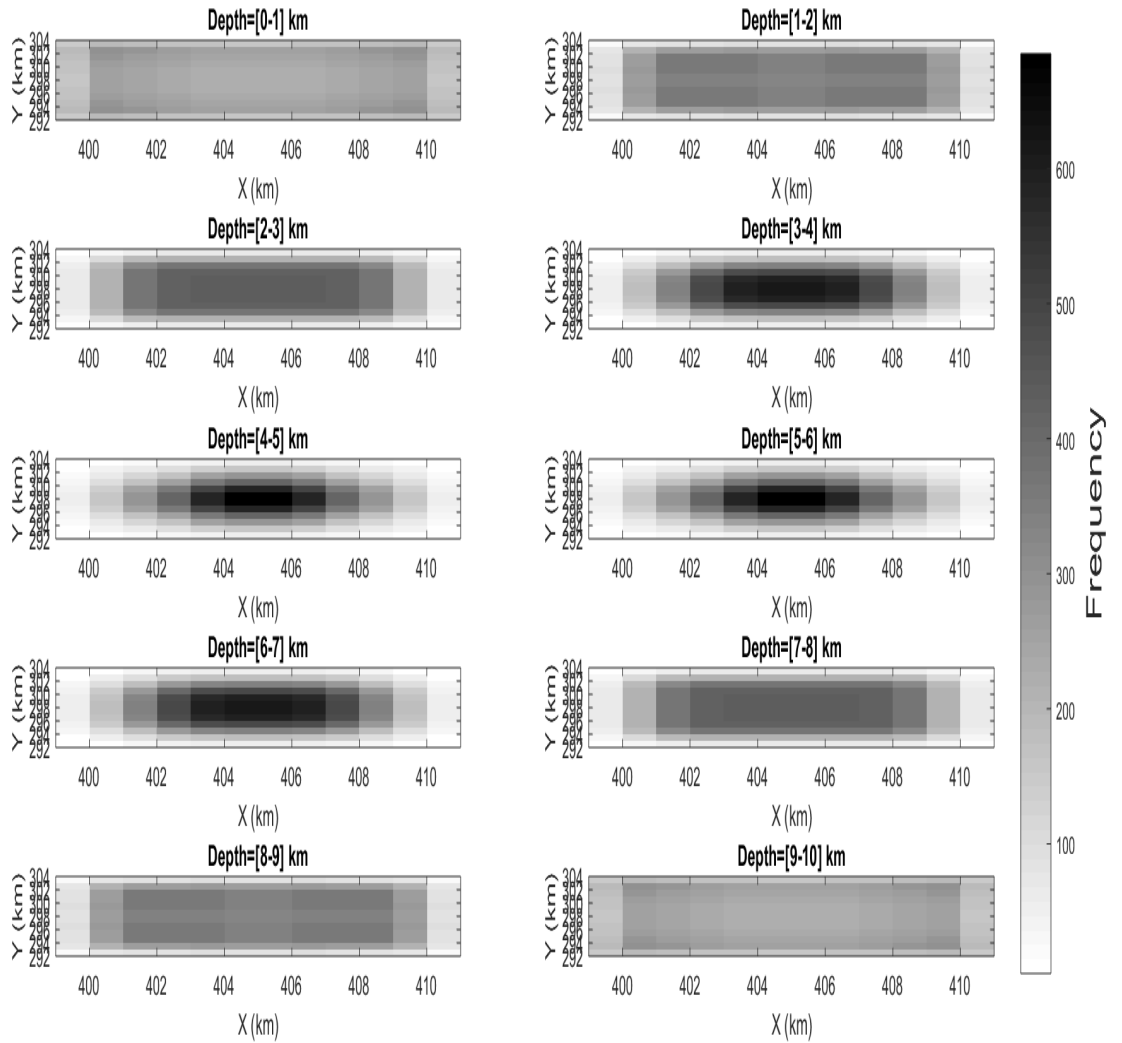
Figure 4.13: The coverage at each depth interval for the even acquisition geometry. The dimensions of the cells are $1 \times 1 \times 1$ km. The color in each cell indicates the number of rays that travel through it.
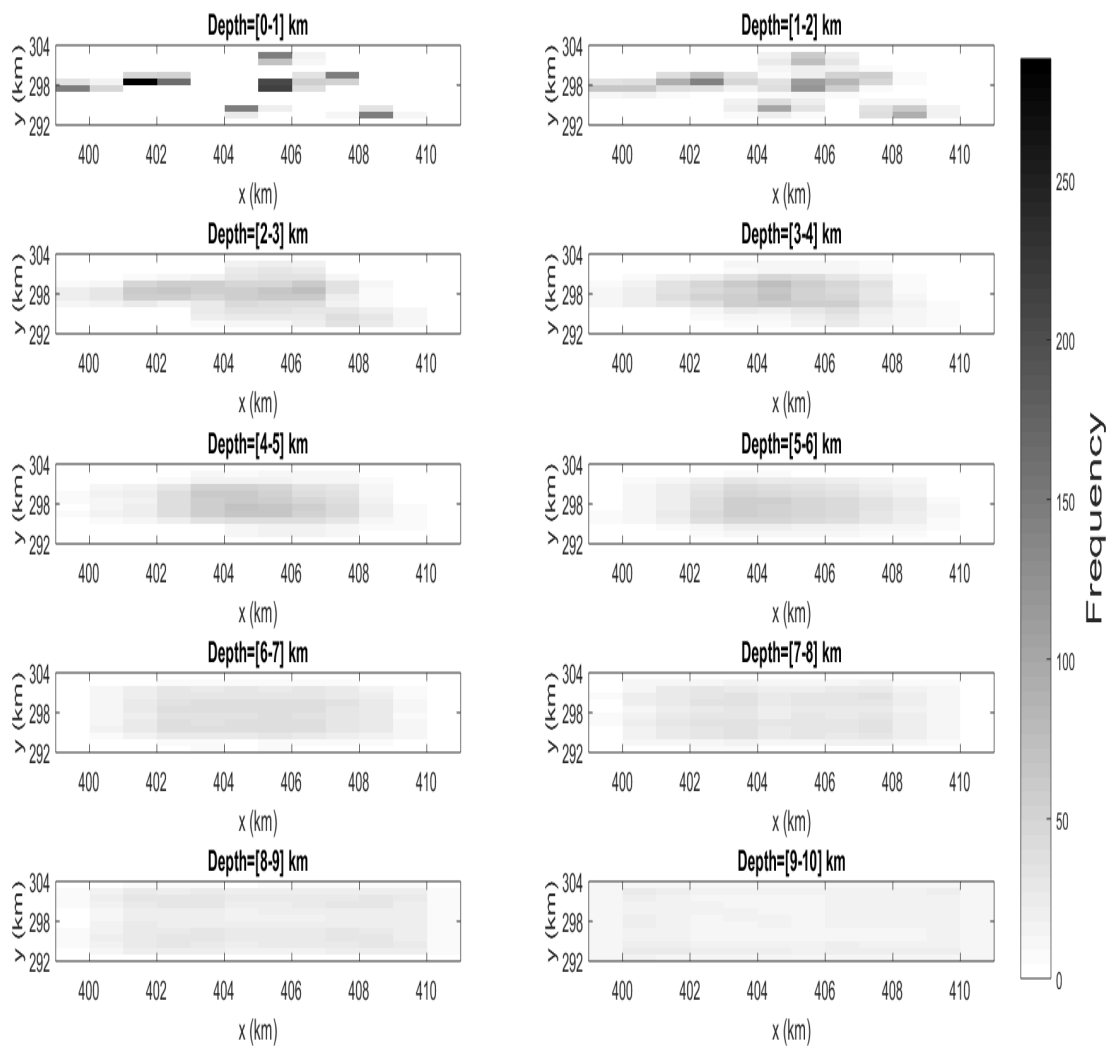
Figure 4.14: The coverage at each depth interval for the real acquisition geometry. The dimensions of the cells are $1 \times 1 \times 1$ km. The color in each cell indicates the number of rays that travel through it.
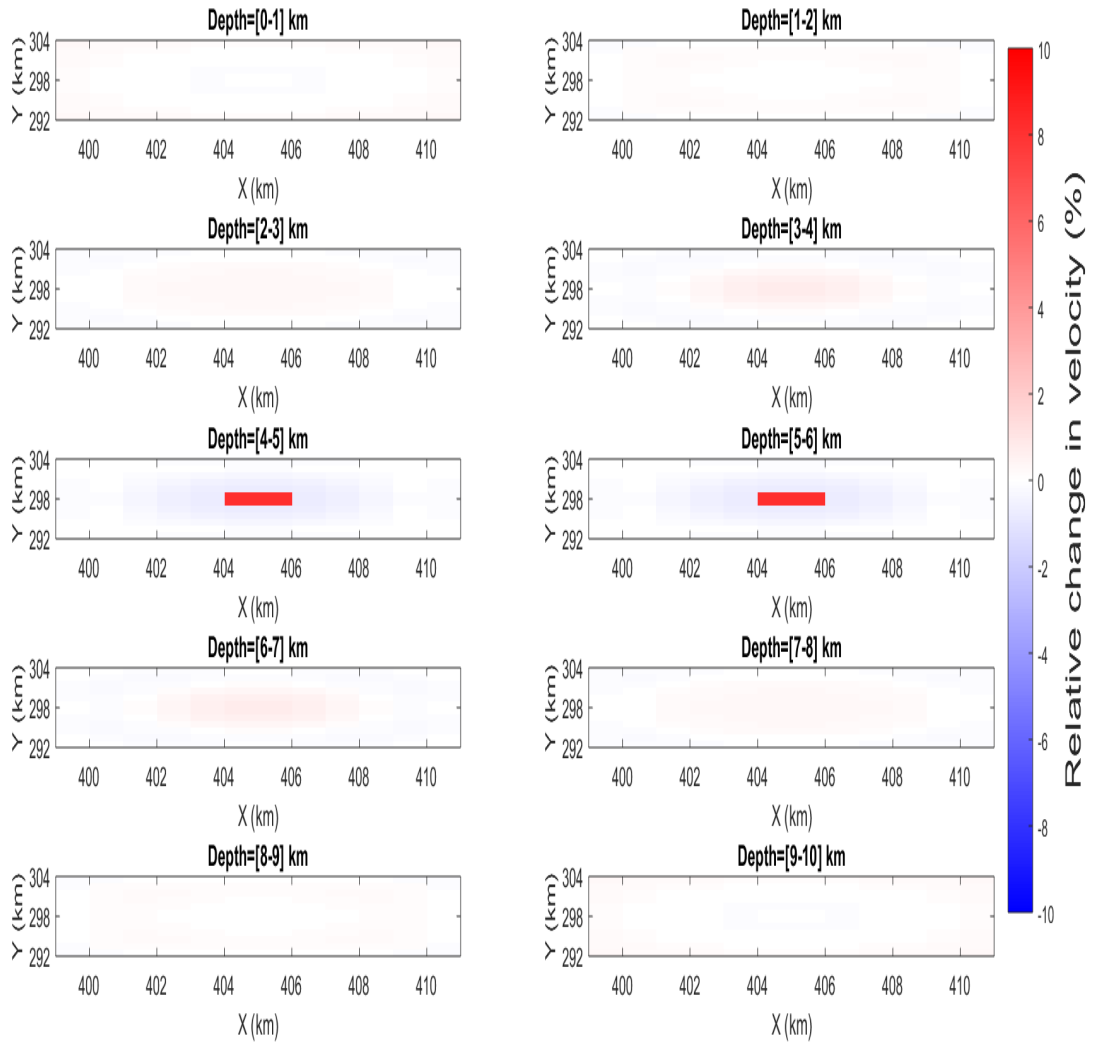
Figure 4.15: The relative change (%) in velocity with respect to the background velocity for test 1 (even acquisition geometry and input model A). The dimensions of the cells are $1 \times 1 \times 1$ km.
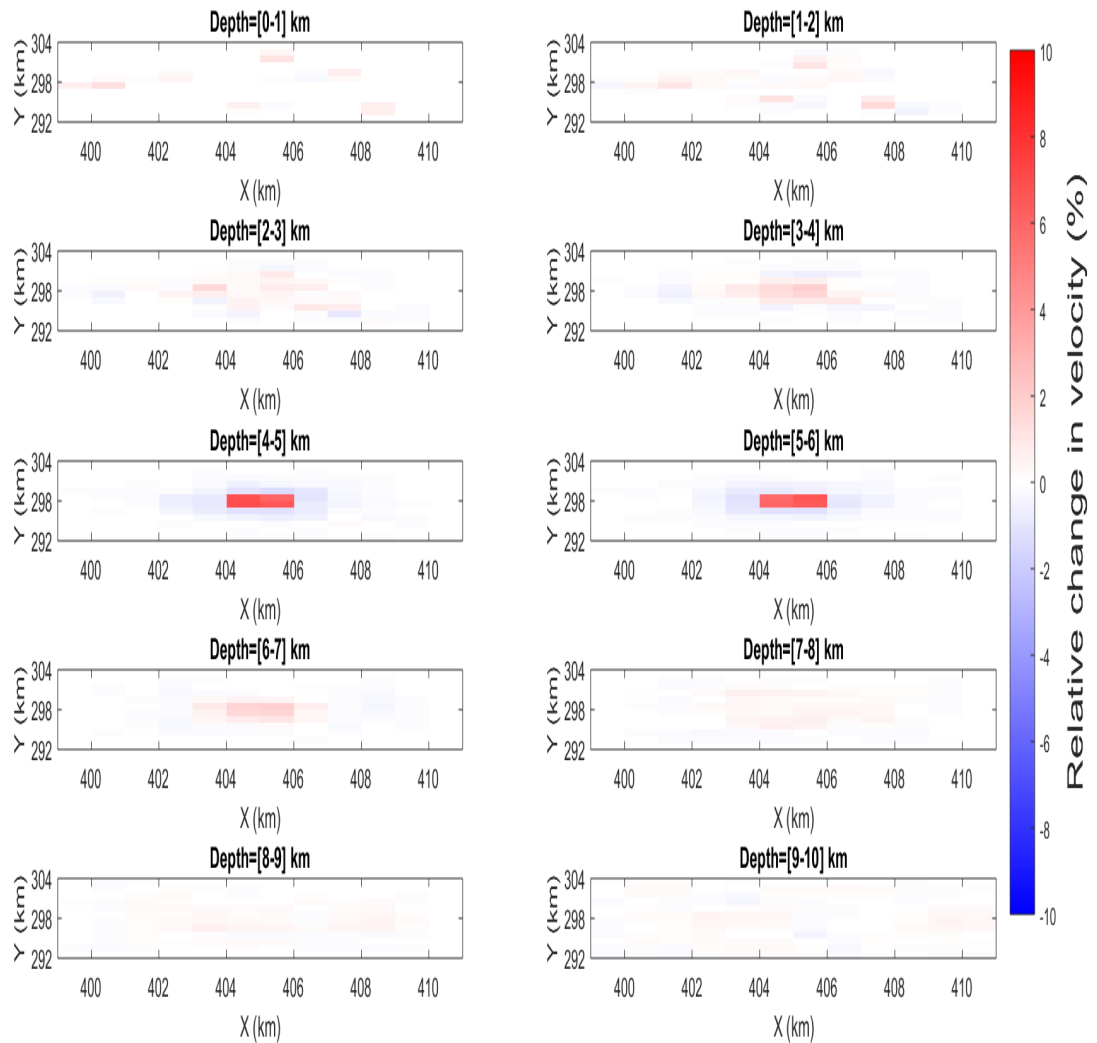
Figure 4.16: The relative change (%) in velocity with respect to the background velocity for test 2 (real acquisition geometry and input model A). The dimensions of the cells are $1 \times 1 \times 1$ km.
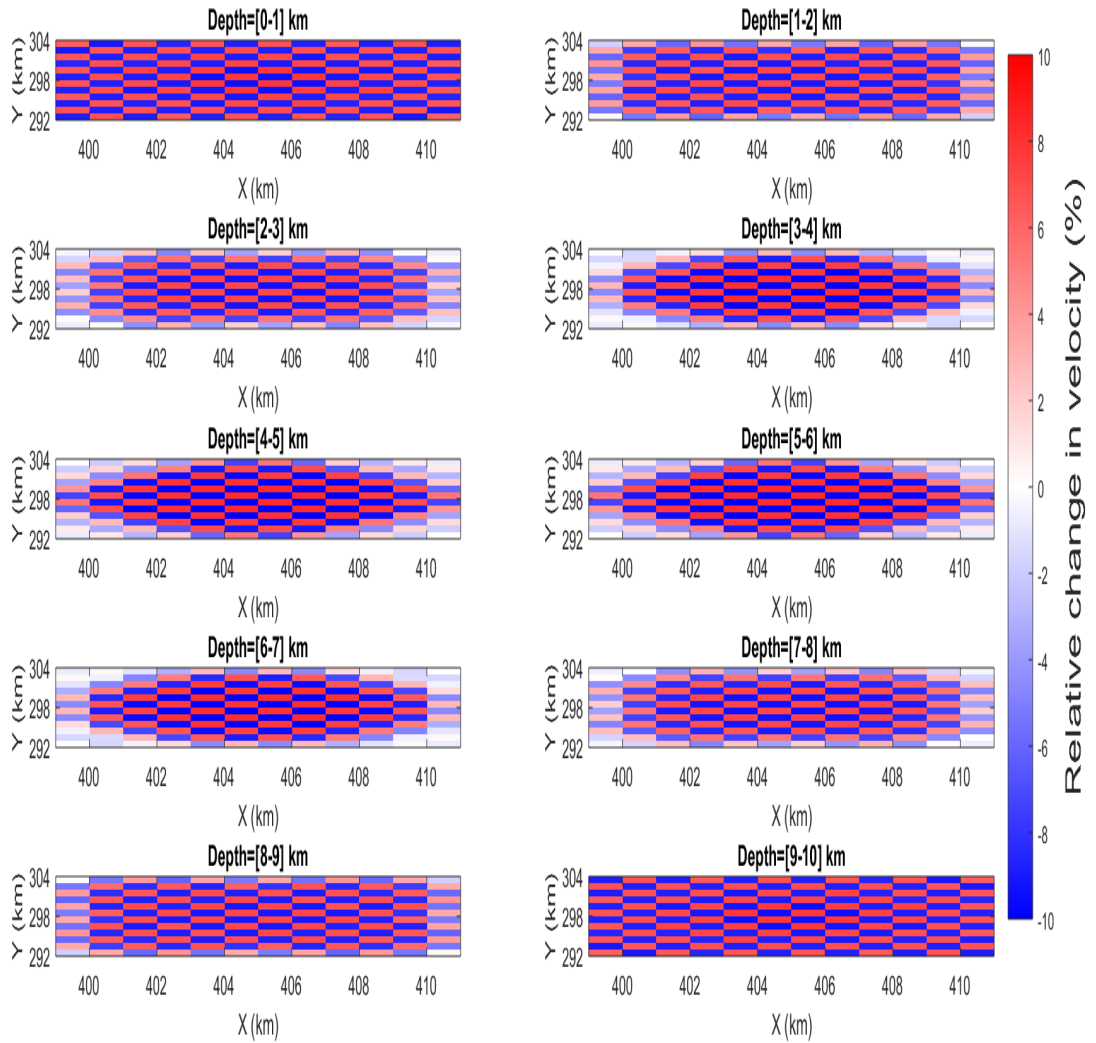
Figure 4.17: The relative change (%) in velocity with respect to the background velocity for test 3 (even acquisition geometry and input model B). The dimensions of the cells are $1 \times 1 \times 1$ km.
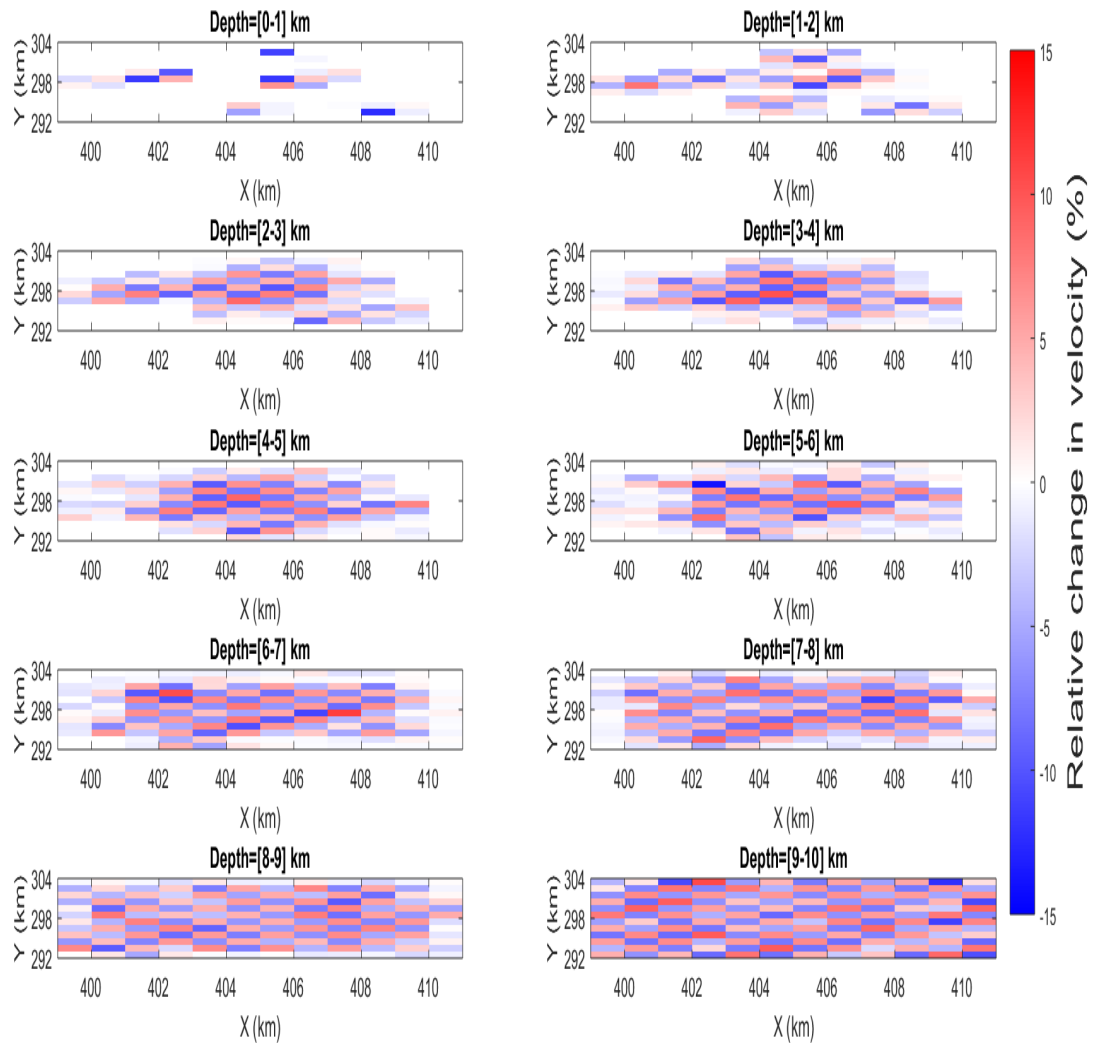
Figure 4.18: The relative change (%) in velocity with respect to the background velocity for test 4 (real acquisition geometry and input model B). The dimensions of the cells are $1 \times 1 \times 1$ km.

The next set of synthetic tests were for the checkerboard (input model B). First
the even acquisition geometry was used. This was test number three. The relative
change in velocity for each layer is shown in Figure 4.17. The recovered velocity
model showed that the resolution is best where the coverage is high, i.e. at the top
and bottom layer, and in the center of the other layers. The change in velocity was
symmetrical. This was also seen in the first test for the even acquisition geometry.

The final synthetic test was the checkerboard test for the real acquisition geometry
(test four). The relative change in velocity for each layer is shown in Figure 4.18.
From this figure it can be observed that the input model was best recovered in the
bottom layer, and the magnitude of recovery decreased as one moved closer to the
surface. Smearing of the anomalies also took place, and the resolution in the top
layer was poor due to the limited coverage.

4.10   Multiscale Travel Time Tomography

An issue associated with tomography is nonuniqueness, i.e. more than one model fits the observed data. This problem is highly affected by the model parameterization[4]. The reason for this is that the size of the cells has direct bearing on the overall ray coverage. At the same time, the ray coverage influences the resolution and thus the magnitude of nonuniqueness [Zhou, 2003].

The fact that parameterization affects the resolution can be discovered from equation (4.43), since each component of $\mathbf{\Delta c}$ corresponds to a cell in the velocity structure. When equation (4.44) is solved for $\mathbf{\Delta c}$, only the components of $\mathbf{\Delta c}$ that correspond to cells which have rays propagating through them will have nonzero values. Furthermore, it is common to set the component of $\mathbf{\Delta c}$ equal to zero if the ray coverage of the corresponding cell is not sufficient. It is clear that the resolution will improve if the size of the cells is larger. A model will, however, not be able to resolve details smaller than its cell size. Tomography that combines cells of different proportions will make it possible to improve the coverage, as well as resolve details of different sizes.

In this thesis the issue associated with limited ray coverage has been addressed through the implementation of multiscale travel time tomography. Using a multiscale system, the overall coverage and resolution of the final velocity model improves. The idea behind this method is to perform travel time tomography for a velocity structure that is discretized into different cell sizes.

The multiscale travel time tomography that is developed in this thesis consists of three steps and three model parameterizations. The first model is a 1D model and is shown in Figure 4.19a and has a cell size equal to $l_x \times l_y \times l_z = 12 \times 12 \times 1$ km. Where l_j, for j equal to x, y or z, is the length of the cell in direction j. The second model is displayed in Figure 4.19b and its cell size is equal to $l_x \times l_y \times l_z = 4 \times 4 \times 1$ km. The third model is shown in Figure 4.19c and has a cell size of $l_x \times l_y \times l_z = 2 \times 2 \times 1$ km.

The first step in the multiscale travel time tomography developed in this thesis involves solving equation (4.44) for $\mathbf{\Delta c}$ for the first model parameterization (Figure 4.19a), until it converges towards a 1D solution. Equation (4.44) is solved by implementing the algorithm introduced in section 4.8 and the first background velocity model is the one obtained from running the algorithm explained in section 4.7. For each new background velocity model, the earthquakes are relocated by applying P-wave single difference as described in section 4.5.

The second step entails solving equation (4.44) for $\mathbf{\Delta c}$ for the second model parameterization (Figure 4.19b), until it converges towards a 3D solution. The final 1D

---

[4]The model parameterization is the size of the cells that the subsurface is divided into.
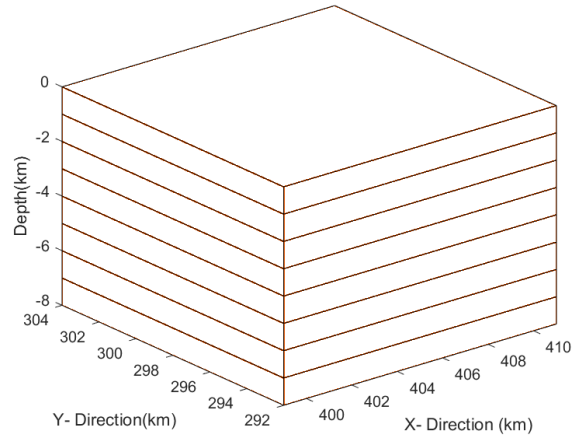
(a) The first model parameterization. The dimensions of one
cell is $l_x \times l_y \times l_z = 12 \times 12 \times 1$ km.
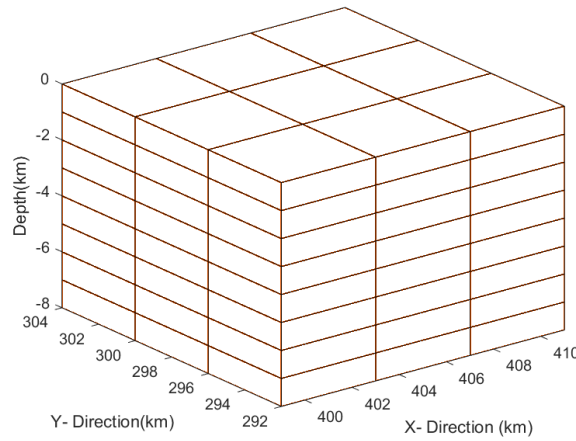
(b) The second model parameterization. The dimensions of one
cell is $l_x \times l_y \times l_z = 4 \times 4 \times 1$ km.
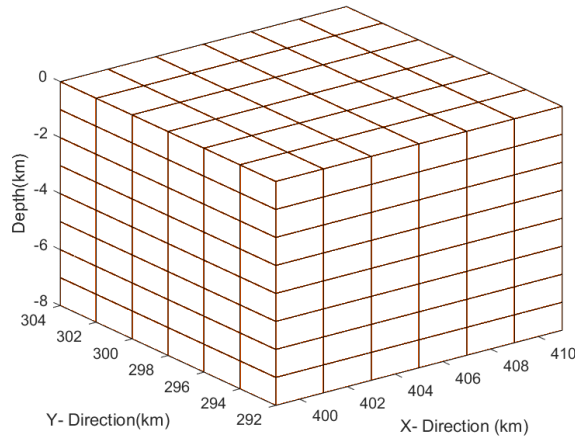
(c) The third model parameterization. The dimensions of one
cell is $l_x \times l_y \times l_z = 2 \times 2 \times 1$ km.

Figure 4.19: Plots of the three different model parameterizations used in the multi-
scale travel time tomography.

velocity model obtained in the first step is used as the first background model in the second step. The earthquakes are relocated for each new background velocity model employing the same method as in the first step.

The third step is equal to the two preceding steps, but relies on the third model parameterization (Figure 4.19c). The final 3D velocity model obtained in the second step is employed as the first background velocity model. The result from this inversion gives the final velocity model.

The aspect that is new with this approach is that it requires a division of the multi-scale travel time tomography into three separated sets. Each of these have a different model parameterization. The inversion is performed on one set at the time, starting at set one where the first background model is uniform, before using the final result derived from it as the first background model in sets two and so on. This is different from multiscale tomography that has been carried out previously. One method that has been practiced before is to perform the inversion on number of model parameterizations simultaneously and combine the output models into one model (e.g. [Zhou, 2003]). Another method involve using irregular model parameterization (e.g. [Fukao et al., 1992; Bijwaard et al., 1998; Fichtner et al., 2013]).

Chapter 5

Results

5.1 Overview

In this chapter an initial description of the data used in this thesis is first given in section 5.2, before the process of selecting seismic arrival times is described in section 5.3. Afterwards, the results from implementating grid search for a background model and the 3D multiscale travel time tomography is presented in sections 5.4 and 5.5. The results from the 3D multiscale travel time tomography are separated into three subsections. Subsection 5.5.1 investigates the results from the 1D inversion, subsection 5.5.2 from the 3D inversion and subsection 5.5.3 the earthquake locations. Lastly, a checkerboard test is employed to examine the resolution of the final parameterization of the 3D multiscale travel time tomography in section 5.6.

5.2 Description of the Data

Waveform data recorded at seismic stations can be used to select the arrival times of seismic waves. These data are needed in order to determine earthquake locations and perform travel time tomography. Waveform data, a catalouge of detected events, some selected arrival times and earthquake locations of earthquakes that took place within the Miravalles geothermal field between the 1st of January 2016 and 1st of August 2018, was provided by the Instituto Costarricense de Electricidad (ICE) that operates the Miravalles geothermal field in Costa Rica.

The data were recorded by 45 broadband stations. Table 5.1 gives the exact locations of these stations. Their geographical distribution is shown in Figure 5.1a. It should be noted that the station coverage of the geothermal field is not optimal, as only 9 of the 45 stations are located in close proximity to the Miravalles geothermal field (Figure 5.1b).
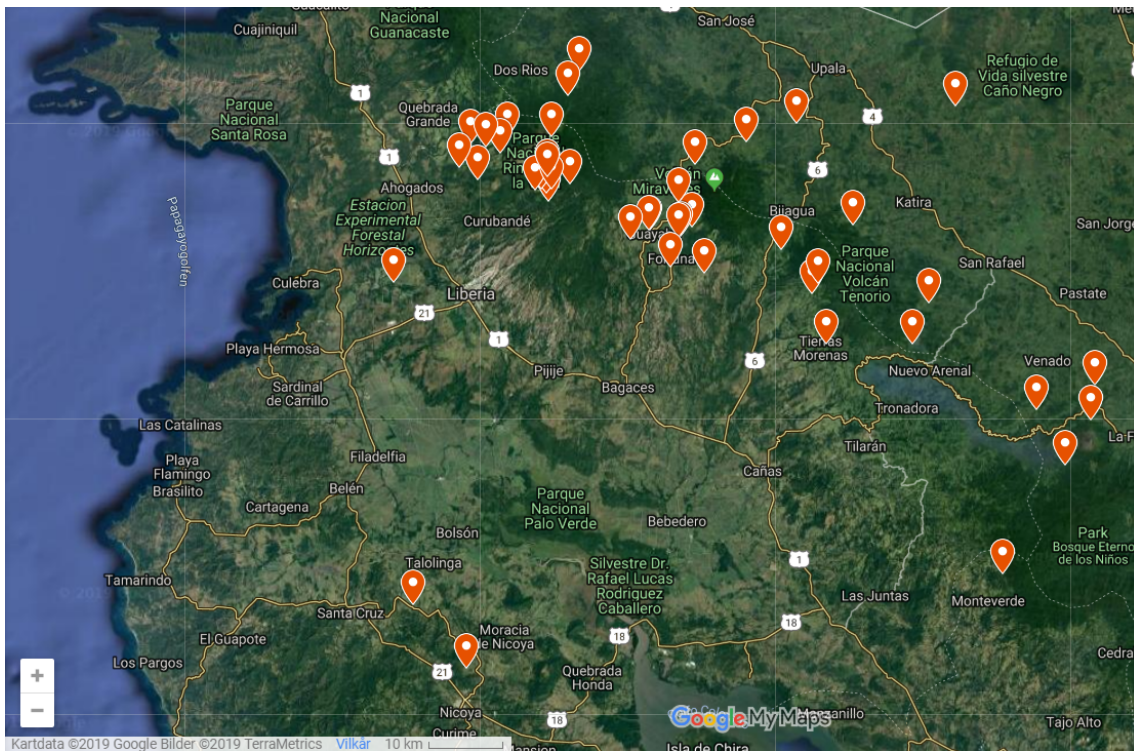
(a) Location of all the 45 seismic stations.
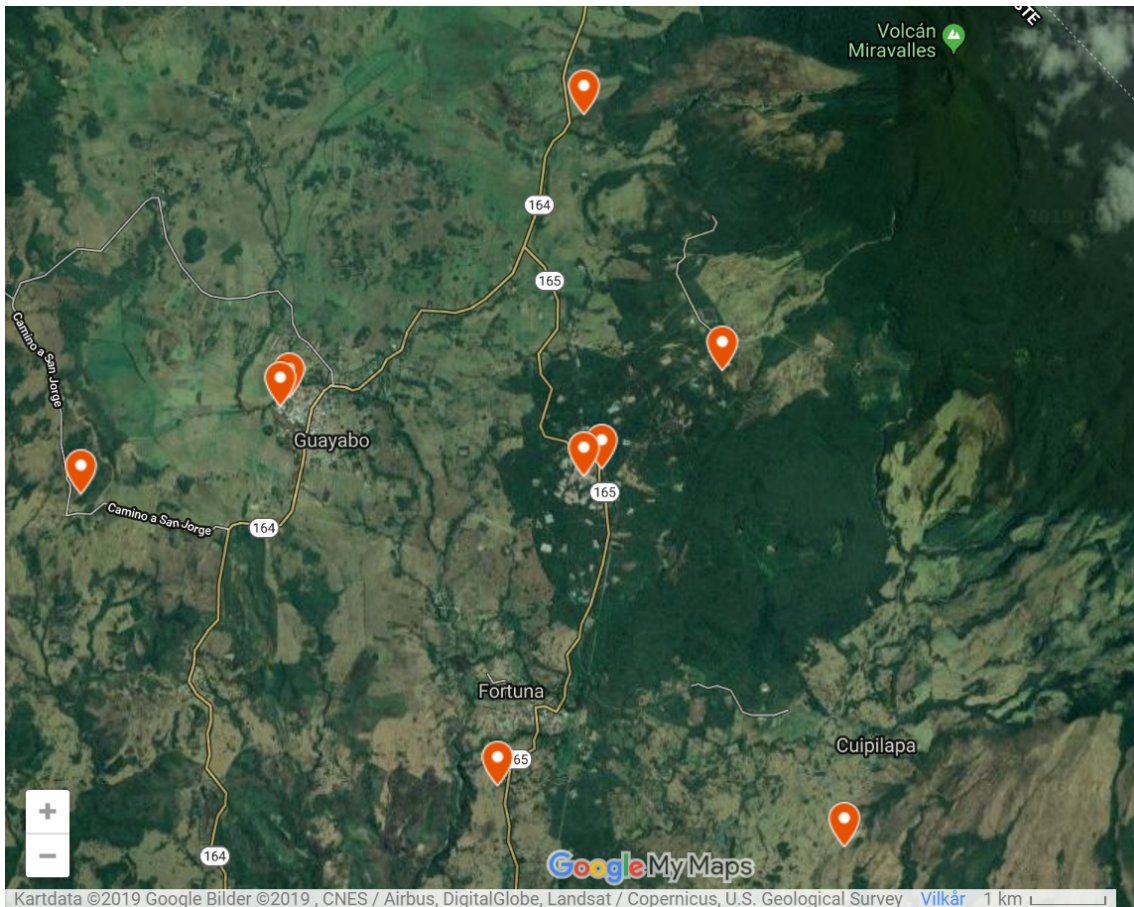
(b) Location of the 9 stations situated at the Miravalles geothermal field.

Figure 5.1: The geographical locations of the seismic stations that provided data.
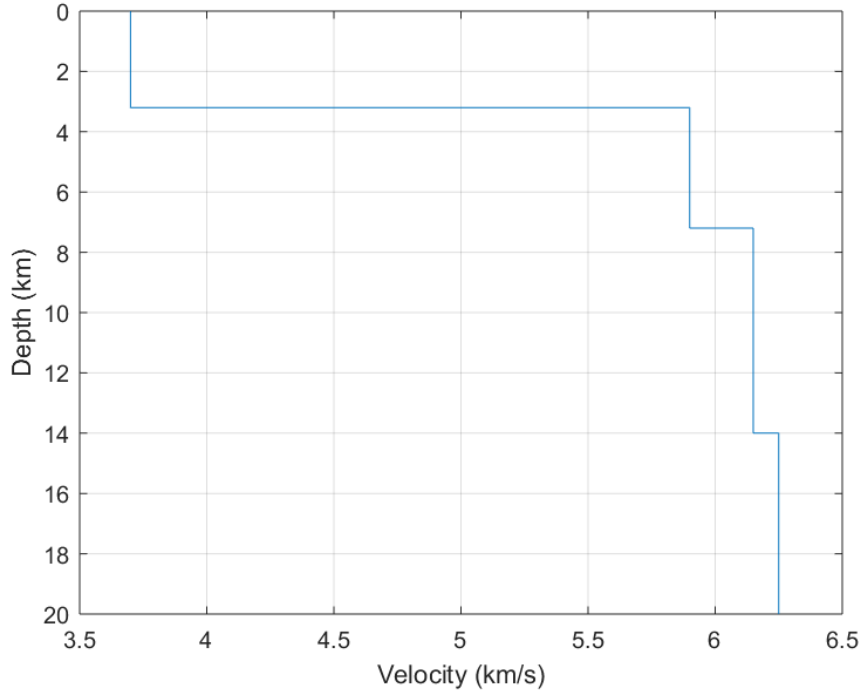
Figure 5.2: The first 20 km of the 1D velocity model used for earthquake location in SEISAN by ICE.

Available data from all the stations are used to locate earthquakes in SEISAN by ICE. Only the first 9 stations, i.e. from station HORN to station CUI, in Table 5.1, however, are used for travel time tomography and the determination of earthquake location using grid search in this thesis.

Between the 1st of January 2016 and the 1st of August 2018, 614 earthquakes were detected at the Miravalles geothermal field. The HYP program was used to determine earthquake location in SEISAN, and it utilizes the velocity model shown in Figure 5.2 [Havskov and Ottemöller, 1999]. The locations determined by ICE and the number of events per layer are shown in Figure 5.3. Nearly 200 earthquakes are located at the surface. This entails that their depth is equal to zero. The magnitude of the detected events is given in California scale, ranging from 0.7 to 3.9. The magnitude distribution is visualized in Figure 5.4. The predominant part of the earthquakes are of a magnitude smaller than 2. The seismic activity within the Miravalles geothermal field is thus largely characterized as micro-seismic.
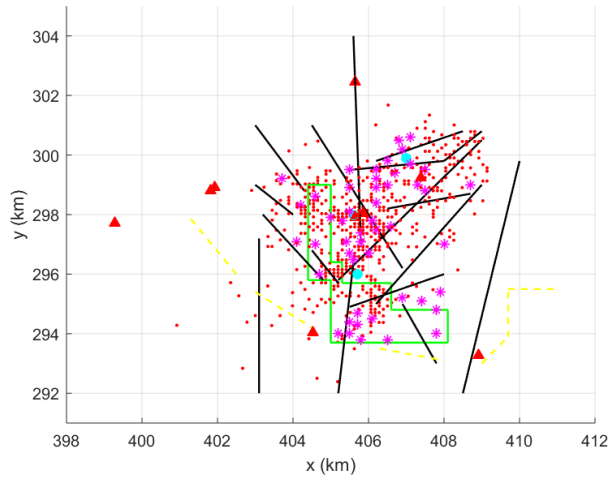
(a) Surface plot of the earthquake locations. The black lines are faults, the yellow dashed line the caldera border, the red triangles the location of the seismic stations, the purple stars the wells and the cyan circles the production units at the Miravalles geothermal field. The area defined by green lines is the main injection area.
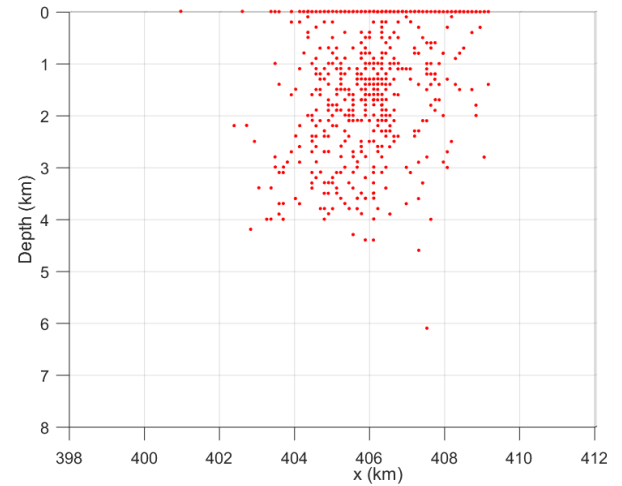
(b) Depth distribution in the x- and z-directions.
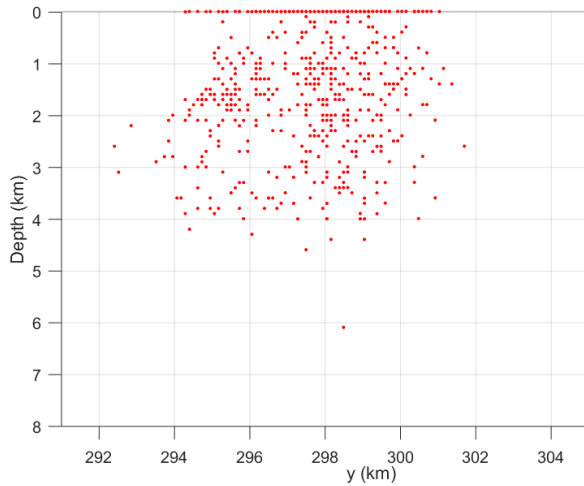
(c) Depth distribution in the y- and z-directions.
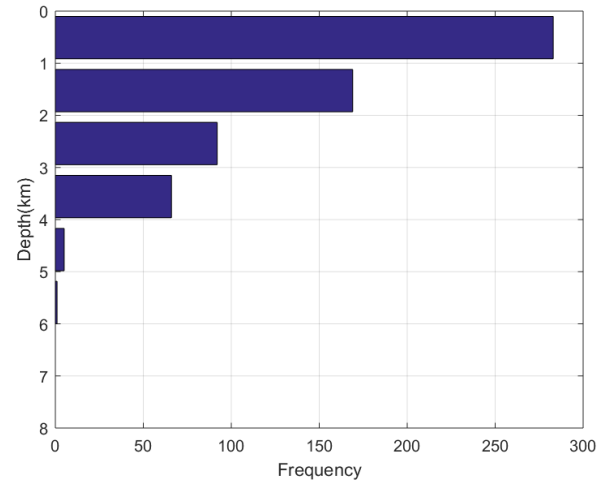
(d) Number of earthquakes per layer.

Figure 5.3: Earthquake locations determined by ICE in SEISAN.

Station Name	Latitude (°)	Longitude (°)
HORN	**10.712**	**-85.178**
MICM	**10.701**	**-85.192**
CAMA	**10.700**	**-85.194**
MESS	**10.741**	**-85.194**
GUA1	**10.709**	**-85.228**
GUAB	**10.708**	**-85.229**
LIM1	**10.698**	**-85.252**
COL	**10.665**	**-85.204**
CUI	**10.658**	**-85.164**
CLAR	10.785	-85.175
MOTZ	10.686	-85.072
ARME	10.812	-85.114
GP77	10.763	-85.324
PP10	10.742	-85.349
ACAL	10.634	-85.035
GPS2	10.752	-85.352
PACM	10.757	-85.358
VORI	10.818	-85.346
PTEN	10.715	-84.987
PEJA	10.895	-85.313
GP1A	10.818	-85.398
BUEV	10.798	-85.407
LAPC	10.767	-85.433
PB63	10.809	-85.442
GBS3	10.782	-85.455
QUEB	10.623	-84.896
COTE	10.575	-84.916
VERA	10.854	-84.865
MAC	10.499	-84.768
REY	10.527	-84.699
MONT	10.307	-84.808
GPS1	10.775	-85.350
GPS3	10.755	-85.365
CANA	10.833	-85.054
BUAI	10.866	-85.326
POB3	10.806	-85.424
CEDE	10.487	-84.703
TIMO	10.576	-85.018
GUAI	10.270	-85.510
SAAN	10.196	-85.447
GP14	10.757	-85.345
ELIB	10.648	-85.534
CASO	10.434	-84.734
TENO	10.646	-85.028
GP03	10.771	-85.350

Table 5.1: Seismic stations employed in this thesis. Data from all the stations are used in SEISAN for earthquake location by ICE. Data from the 9 first stations shown in bold, are employed in this thesis.
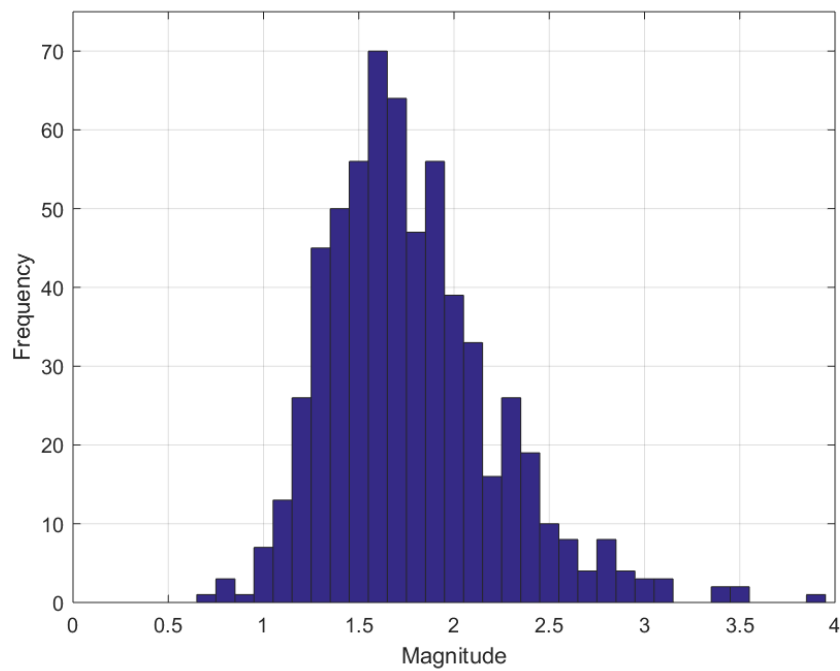
Figure 5.4: Magnitude distribution of the detected events in the time period the 1st of January 2016 to the 1st of August 2018 at the Miravalles geothermal field.

5.3 Selecting First-Arrival Times from Waveform Data

Selecting first-arrival times is an important first step for processing seismic waveform data in this thesis, as they are required to determine the earthquake locations and do the travel time tomography.

Nearly 2700 P-arrival times were selected from 614 seismic events at the first 9 stations in Table 5.1 from January 2016 to August 2018. The first-arrival times are manually picked in order to ensure reliable and accurate observations. Even though some of the selected first-arrival times were done by ICE, these where revised in this thesis for consistency. In addition to doing this, a number of arrival times were also selected.

The process of choosing arrival times is illustrated in Figures 5.5a and 5.5b. The P-arrival time is selected at the location where the waveform exhibits a sudden increase in amplitude. This is marked by a vertical black line with the label EP above it.

The difference between stations of high and low quality is shown in Figures 5.5a and 5.5c that illustrates the vertical-component of waveforms recorded by stations COL and CASO, respectively. Both stations display waveform data for the 3.5 magnitude earthquake that took place on the 25th of July 2017 within the Miravalles geothermal field. It is difficult to determine where the first motion of the earthquake took place at station CASO (Figure 5.5c). Its recorded waveform for this earthquake is therefore of low quality and a selection of a P-arrival cannot be made. By contrast, the first motion is sharp at station COL and the first-arrival time can consequently be accurately determined (Figure 5.5a).
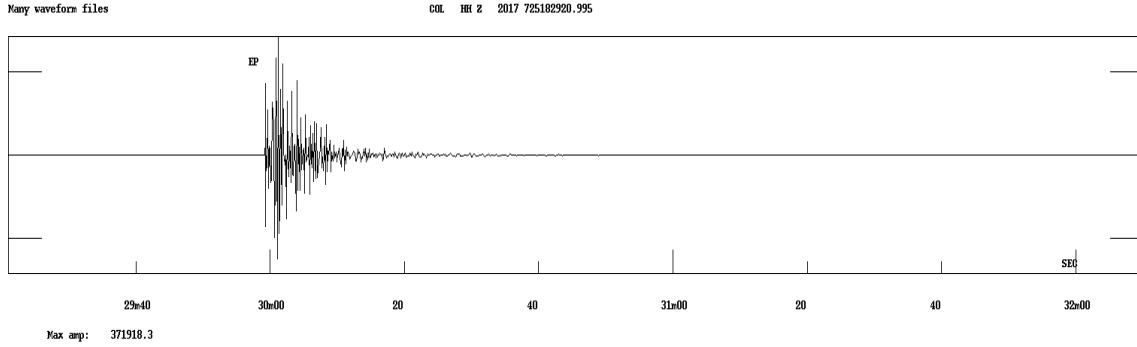
(a) Z-component at station COL.
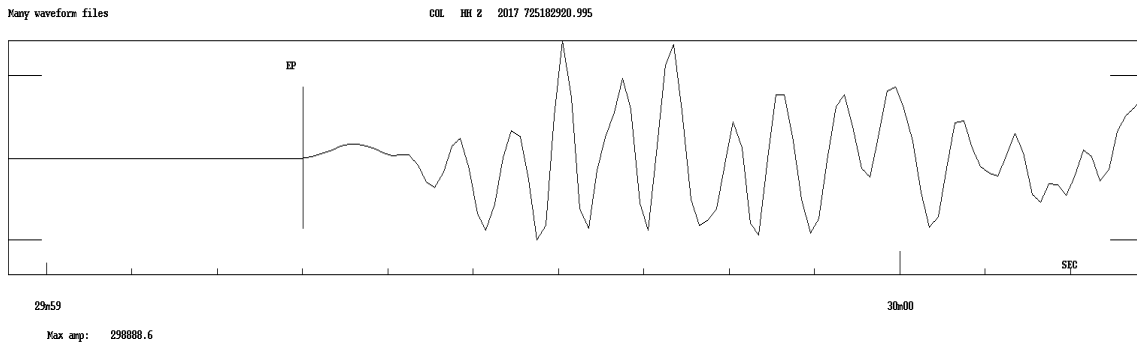
(b) Zoomed section on Z-component at station COL.
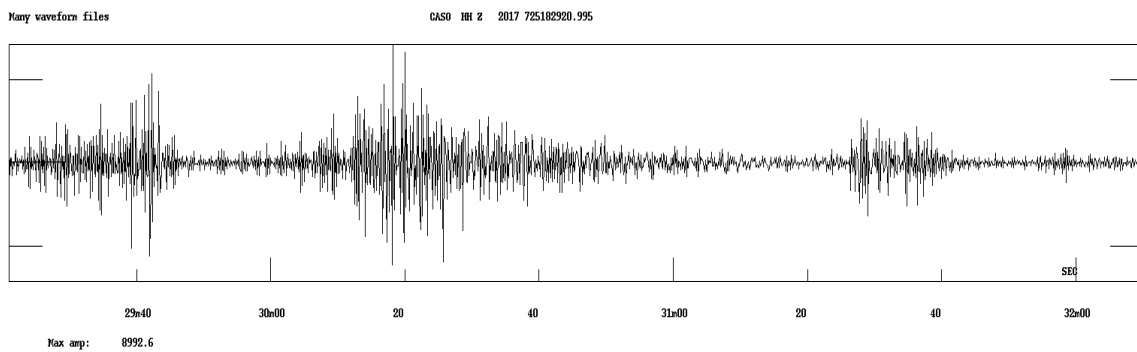
(c) Z-component at station CASO.

Figure 5.5: An example of selecting first-arrivals at a station with a good signal to noise ratio (Figures (a) and (b)). Figure (c) is an example of a station where it is difficult to select first arrivals. The displayed data is from the 3.5 magnitude earthquake that occurred on the 25th of July 2017.

5.4   Results: the Constant Velocity Model

The first step towards the determination of a 3D velocity model of the Miravalles geothermal field is to find the best fitting constant velocity model. This constant velocity model is employed as the first background model for the 1D multiscale travel time tomography.

The algorithm introduced in section 4.7 is used to determine the most optimal constant background model.

The velocities that are tested for the constant background model are in the range 2.6 km/s to 3.8 km/s. This interval was chosen based on the 1D velocity model employed by ICE in SEISAN to determine earthquake locations at the Miravalles geothermal field (Figure 5.2).

The detected earthquakes are relocated for each constant background velocity model. The earthquakes are located using differences in observed arrival times and calculated travel times of the P-waves. Finally the misfit for each location is computed through applying equation (4.33).
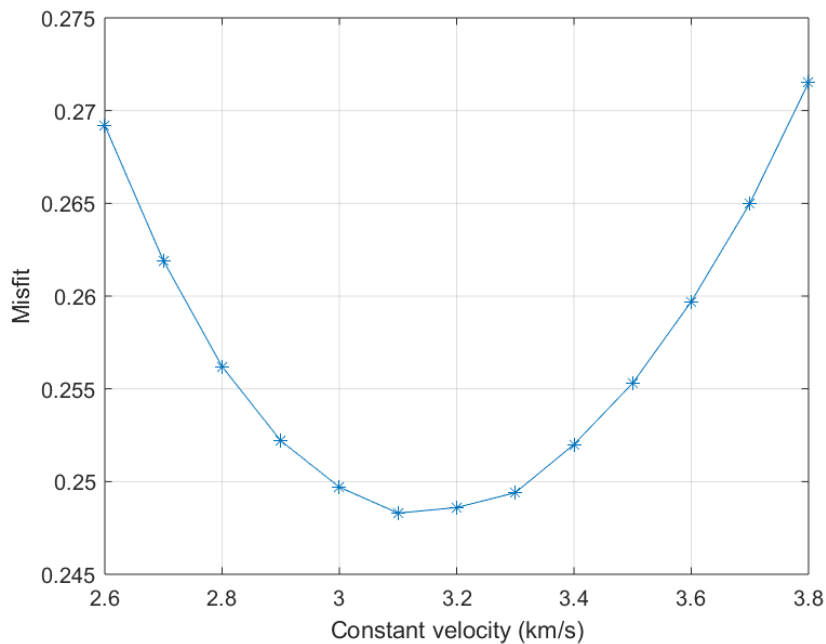
Figure 5.6: A plot of how the misfit changes when different constant background velocity models are used to relocate the detected earthquakes.

A grid search covering the entire Miravalles geothermal field is computationally demanding. For this reason, the earthquake locations determined by SEISAN are

implemented to restrict the grid search area for each event. A new location is searched for in an area which extends ± 2 km in the x- and y-directions of the location determined by SEISAN[1], i.e. an area of 16 km^2. In the z-direction depths from 0 to 8 km were tested.

The average misfit for all the determined earthquake locations has been used as the overall measure of fit of the background model[2]. The most optimal constant background velocity model for the 1D travel time tomography is the constant background model for which the difference between observed arrival times and computed travel times is smallest, i.e. the misfit.

Figure 5.6 illustrates how the (mean) misfit for the relocated earthquakes changes as a function of the constant background velocity. It shows that the 3.1 km/s constant background model resulted in the best fit between the observed arrival times and calculated travel times used to located the earthquakes. A constant 3.1 km/s velocity model is therefore used as the starting model for the 1D multiscale travel time tomography.

---

[1]This is also utilized in the multiscale travel time tomography. Instead of using the locations from SEISAN, however, the locations determined in the previous iteration are employed.

[2]This is how the measure of fit is defined for all the velocity models throughout this chapter.

5.5   Results: Multiscale Travel Time Tomography

In this section the multiscale travel time tomography results are presented. The implementation of multiscale travel time tomography was discussed in section 4.10 and a detailed explanation of the tomography algorithm was given in section 4.8.

P-wave single difference travel times are employed to determine the most likely hypocenter locations. The earthquakes are relocated for each new velocity model.
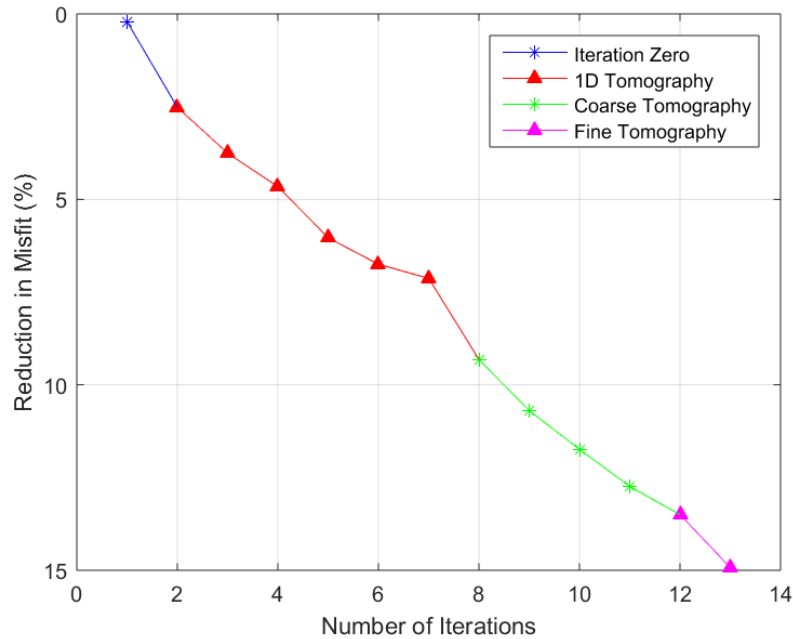
Figure 5.7: The misfit for the multiscale travel time tomography.

A total of 12 iterations were performed for the multiscale travel time tomography. A plot illustrating the reduction in misfit for each iteration is shown in Figure 5.7. Iteration zero is the 3.1 km/s constant background velocity model (colored blue in Figure 5.7). The reduction in misfit for the following iterations is relative to the misfit of iteration zero.

6 iterations were performed for the 1D tomography (colored red in Figure 5.7). This is the first step of the multiscale travel time tomography wherein the misfit was reduced with almost 7%.

4 iterations were conducted for the coarse tomography with cell sizes of $4 \times 4 \times 1$ km (colored green in Figure 5.7). This is the second step of the multiscale travel time tomography and it resulted in a reduction of approximately 5.6% in misfit.

The final step in the multiscale travel time tomography, called the fine tomography

with cell sizes of $2 \times 2 \times 1$ km, was performed twice (colored pink in Figure 5.7). The reduction in misfit was almost 2.3%.

The total reduction in misfit is nearly 15% from iteration zero to the final velocity model obtained for the fine tomography.

5.5.1   Multiscale Travel Time Tomography: 1D Velocity Model

The first step of the multiscale travel time tomography is to determine the 1D velocity model. In section 5.4 it was found that the most optimal constant velocity model was 3.1 km/s. This is therefore selected as the first background model for the 1D travel time tomography.

The 1D tomography was performed 6 times. The corresponding 1D velocity models are shown in Figure 5.8, and are identified by an index given in the top right corner of the figure. "1" denotes the 1D model obtained from the first inversion and "6" the last.
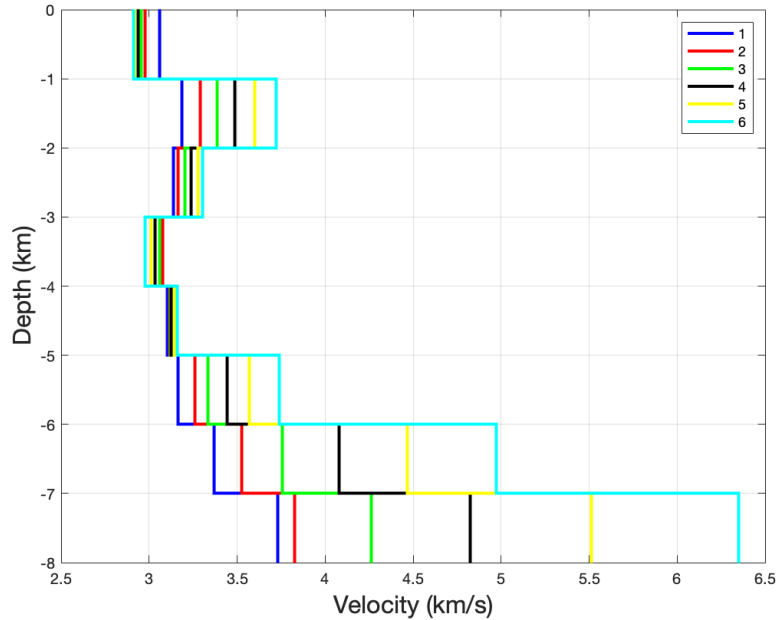
Figure 5.8: Plot of the 1D velocity models obtained from the inversion. The different colors indicate the iteration number.

The final 1D velocity model has a relatively high and low velocity layer located close to the surface (cyan colored line in Figure 5.8). The high velocity layer is at a depth of 1 to 2 km. The low velocity layer, on the other hand, is found between 3 and 4 km. For depths larger then 4 km the velocity increases.

5.5.2   Multiscale Travel Time Tomography: 3D Velocity Model

The 3D multiscale tomography consists of both the coarse and fine tomography, called steps two and three in section 4.10. A total of 6 iterations were performed for these two steps. The final 1D velocity model from step one is used as the first background model. This is the 1D model labeled "6" in Figure 5.7.

The final velocity model[3] from the 3D multiscale tomography is shown in Figure 5.9. This figure also includes the main faults (black lines), wells (purple stars), the three production units (cyan circles), the injection area (marked by green lines), seismic stations (red triangles) and the caldera border (yellow dashed line).

Figure 5.9: The final 3D velocity model from the multiscale travel time tomography. The black lines are faults, the yellow dashed line the caldera border, the red triangles the seismic stations, the purple stars the wells and the cyan circles the production units at the Miravalles geothermal field. The area defined by green lines is the main injection area.

The main features of this velocity model are that there are higher velocities between

---

[3]Smoothing is applied to all the figures of the final velocity model.
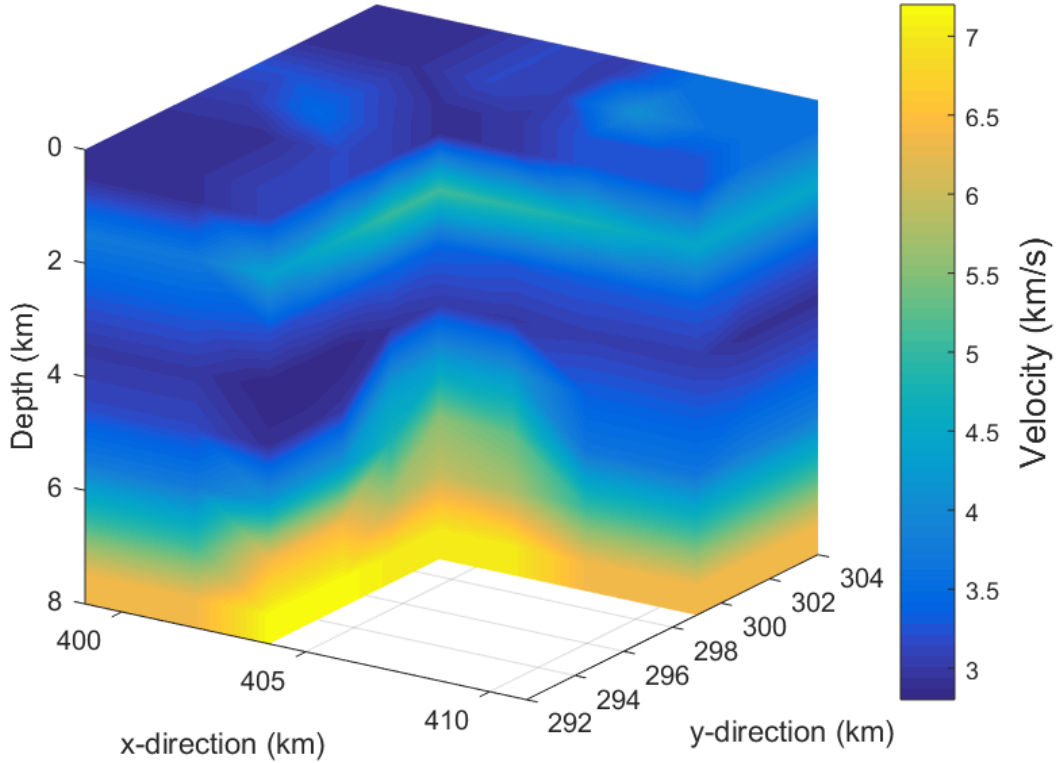
Figure 5.10: Slice of the inside of the final 3D velocity model from the multiscale travel time tomography.

a depth of approximately 0.8 and 2.1 km, and it increases for depths higher than 5 km. In addition, there is a low velocity layer between roughly 2.5 and 4.5 km.

The surface

The surface of the velocity structure is shown in Figure 5.11. The major features of it include four areas of higher velocities that surround a lower velocity area in the center of the figure. The low velocity area is between x ∈ [404, 406.5] km and y ∈ [297, 300] km.

The reservoir

The layer located at a depth of approximately 0.8 to 2.1 km with relatively higher velocities, is interpreted in this thesis as the Miravalles geothermal reservoir. Figure 5.12 shows a horizontal slice of the reservoir at a depth of 1.5 km. The same features, e.g. the faults and caldera border, that were included on the surface of the block
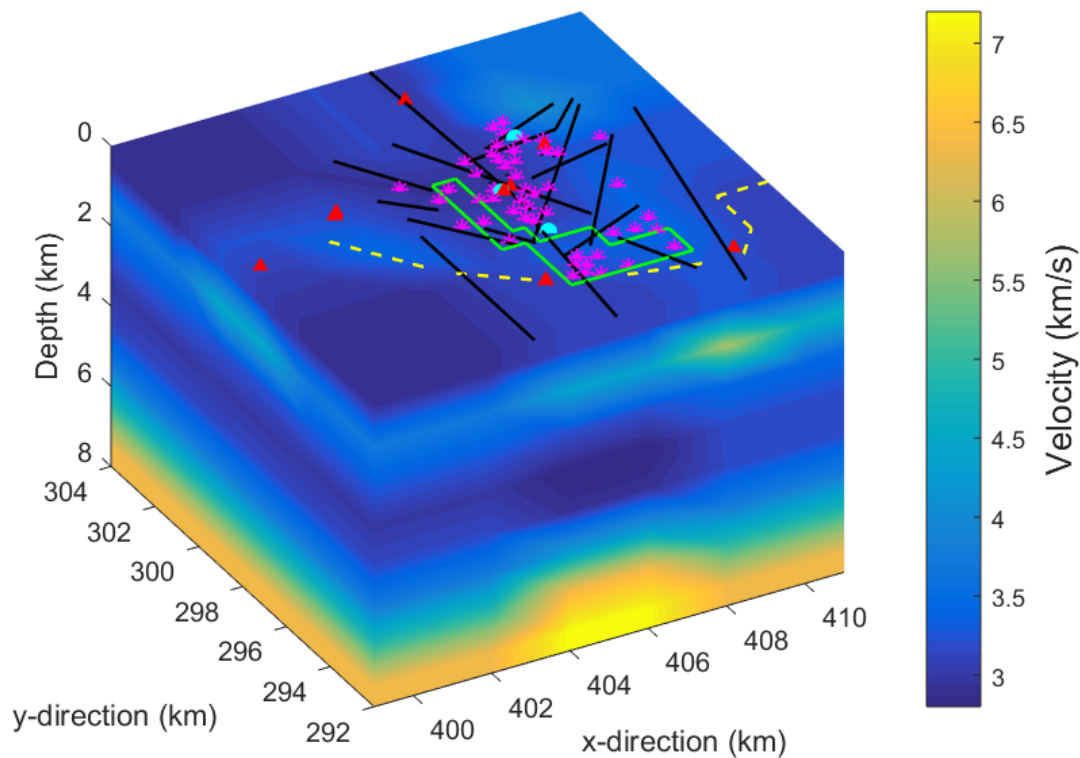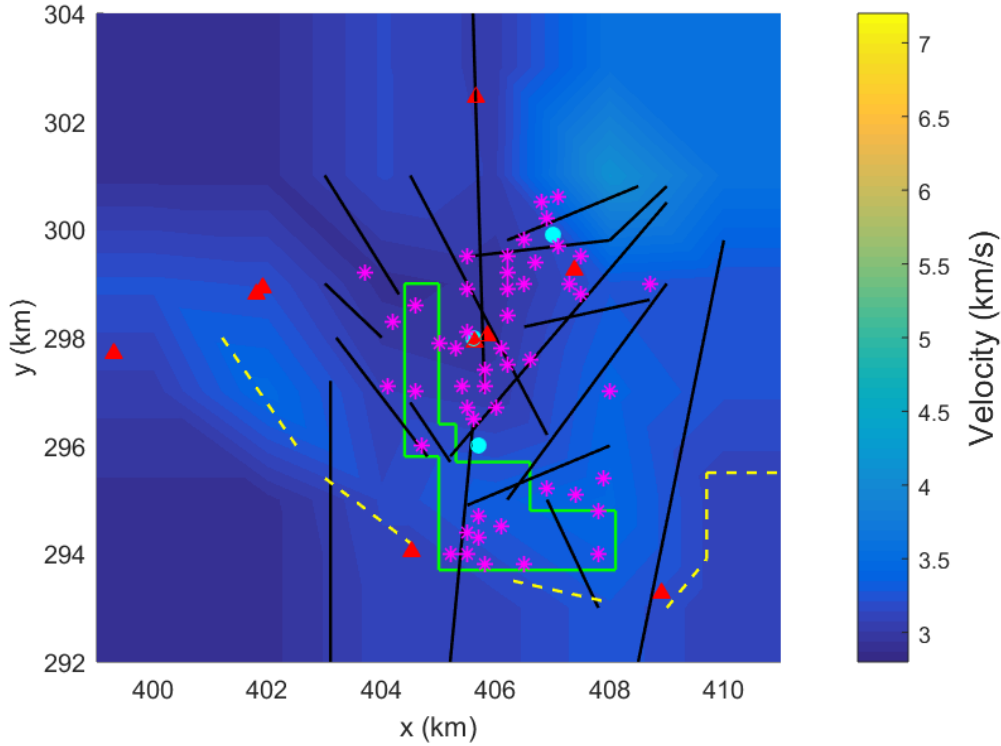
Figure 5.11: The surface of the final 3D velocity model obtained from the multiscale travel time tomography. The black lines are faults, the yellow dashed line the caldera border, the red triangles the seismic stations, the purple stars the wells and the cyan circles the production units at the Miravalles geothermal field. The area defined by green lines is the main injection area.

velocity structure in Figure 5.9 are added to this figure.

There exist three high velocity areas at a depth of 1.5 km. The first one is located between x $\in [407, 409]$ km and y $\in [300, 302]$ km. The second is situated between x $\in [401, 406]$ km and y $\in [296, 299]$ km. Finally, the third is located between x $\in [407, 409]$ km and y $\in [292, 296]$ km. The velocities gradually decrease towards the edges of the reservoir, except for south of the third high velocity area. Meanwhile, the lowest velocities are found towards the western part of the field.

The reservoir is visualized as a volume in Figure 5.13. It is thickest in the eastern part, and gradually becomes thinner towards the south- and northwest.

The seismicity inside the reservoir is shown in Figure 5.14. Nearly all of the determined earthquake locations are found at the eastern side of the injection area. Furthermore, there appears to be a cluster of events in the center of the field, i.e. at
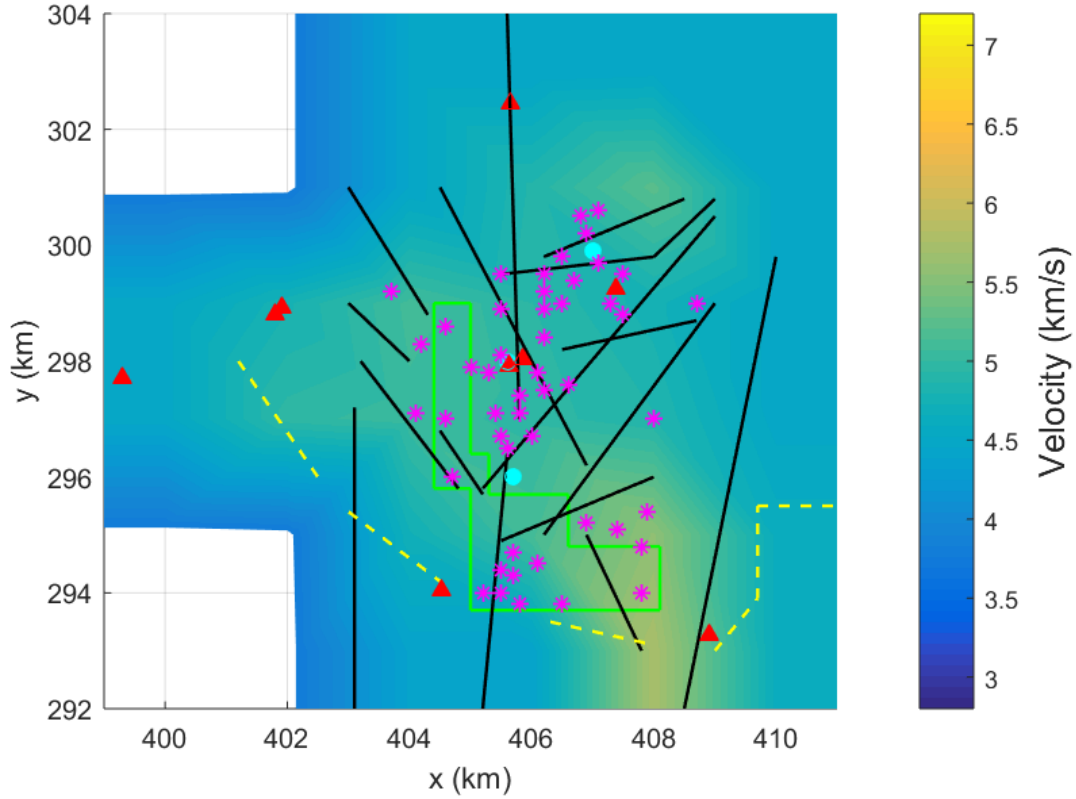
Figure 5.12: A slice of the Miravalles geothermal reservoir at 1.5 km depth. The black lines are faults, the yellow dashed line the caldera border, the red triangles the seismic stations, the purple stars the wells and the magenta circles the production units. The area defined by green lines is the main injection area

$x \in [405, 407]$ km and $y \in [297, 298.3]$ km.

The intrusion

There is an ellipsoidal-shaped high velocity structure inside the 3D velocity model (Figure 5.10). This structure is interpreted as an intrusion in this thesis and is plotted as a isosurface in Figure 5.15. This structure is located approximately in the center of the velocity model, and it starts at a depth of approximately 4 km and has a width of 6 and 8 km in the x- and y-directions, respectively.
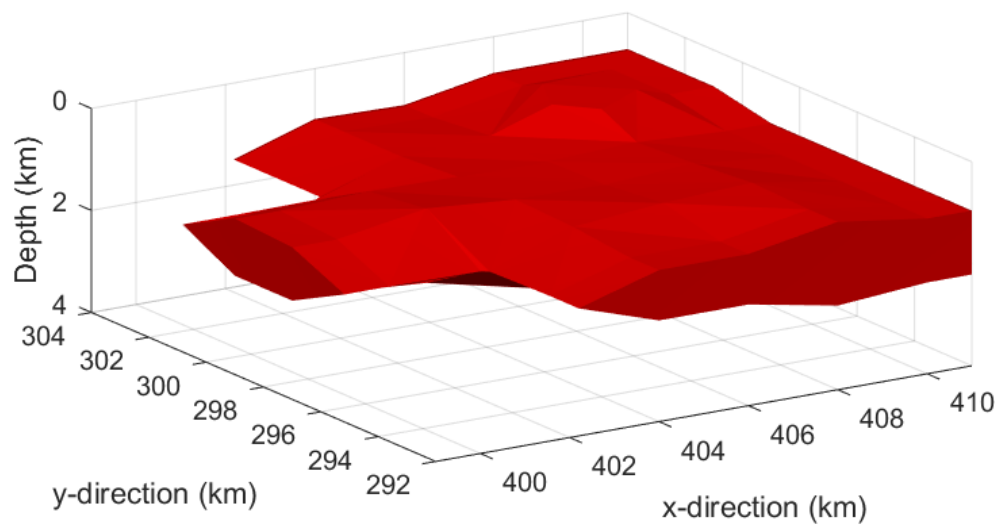
Figure 5.13: The Miravalles geothermal reservoir. It corresponds to the high velocity area between approximately 0.8 to 2.1 km deep in Figure 5.9.
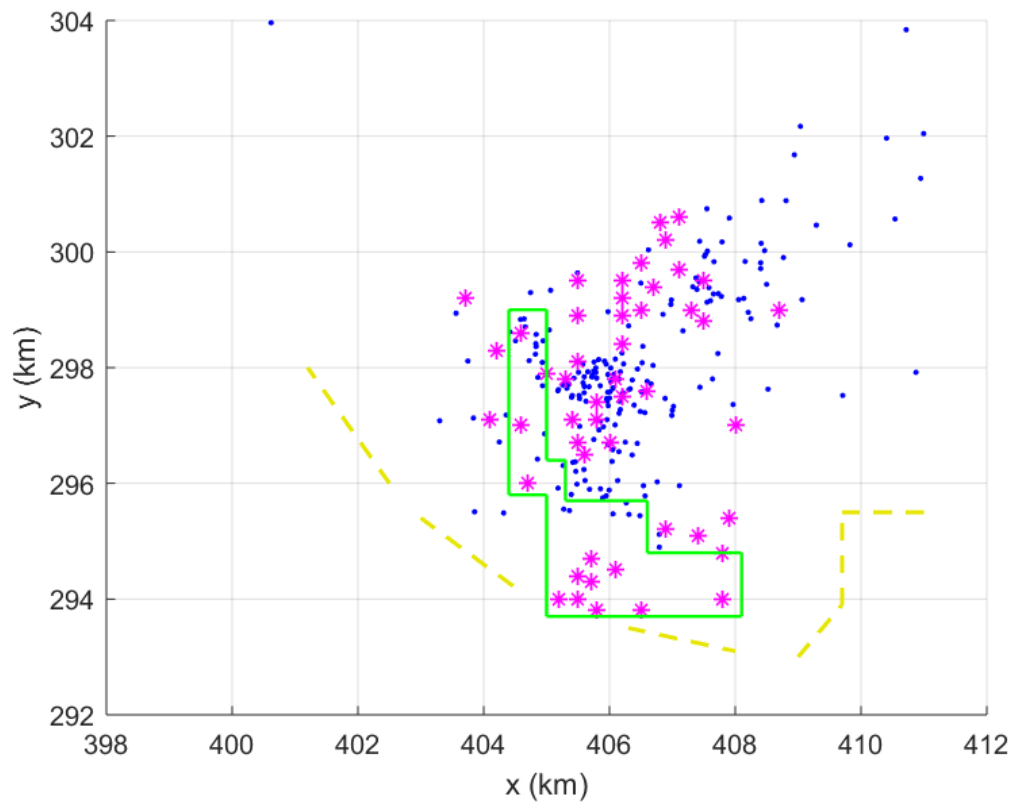
Figure 5.14: Seismicity inside the Miravalles geothermal reservoir. The determined earthquake locations are marked by blue circles, the yellow dashed line is the caldera border and the purple stars mark the location of the wells. The area defined by green lines is the main injection area.
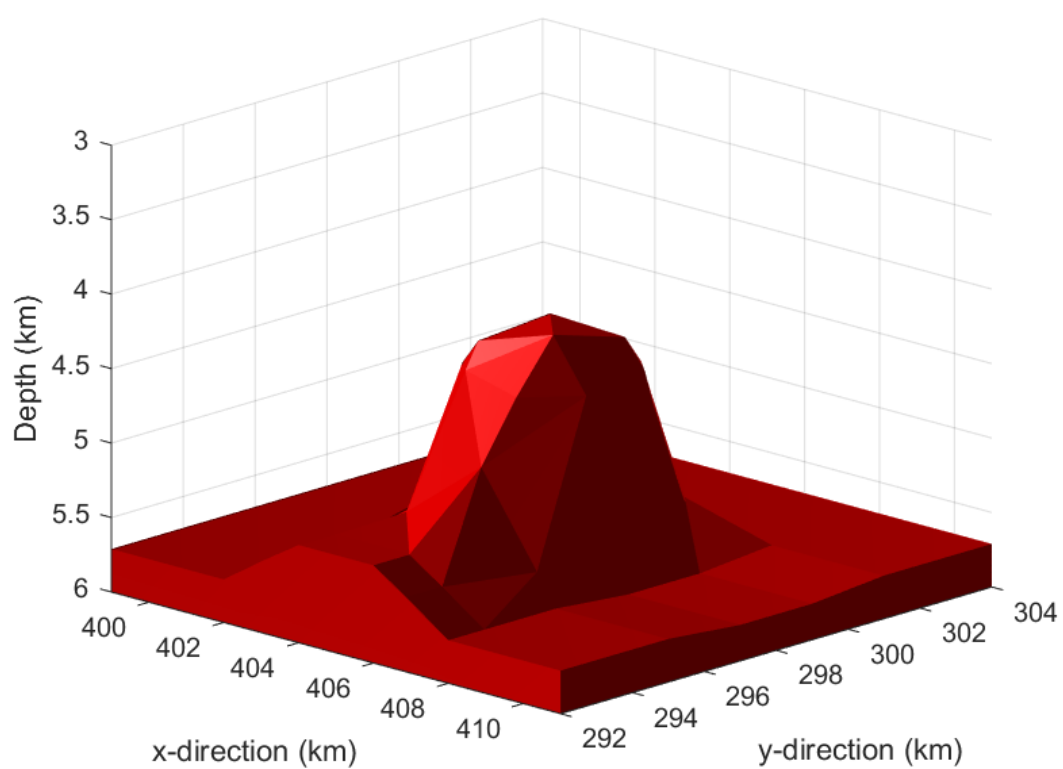
Figure 5.15: The ellipsoidal-shaped structure beneath the Miravalles geothermal field which is interpreted as an intrusion.

5.5.3   Earthquake Locations

In this subsection the final earthquake locations are first presented, before showing how the locations have changed from the constant background velocity model (iteration zero in Figure 5.7) to the final 3D velocity model (iteration 13 in Figure 5.7). Lastly, the locations of the 3D velocity model are compared with those determined by ICE in SEISAN.
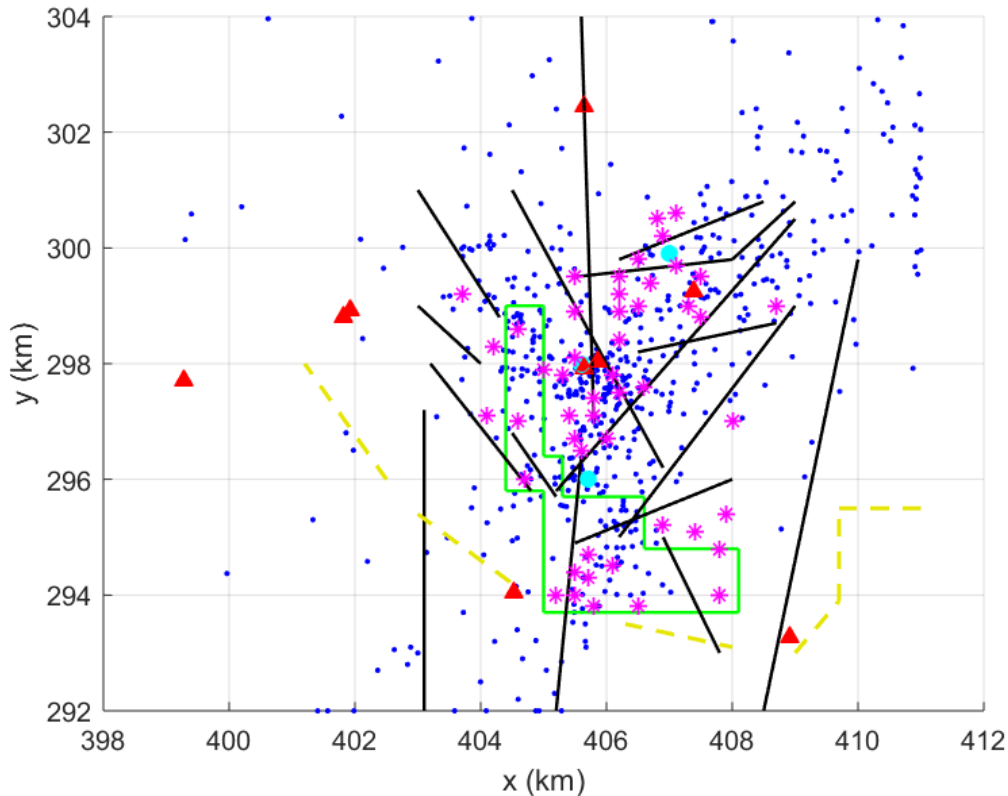
Figure 5.16: Surface plot of the final earthquake locations from the 3D multiscale tomography. These are marked by blue circles. The black lines are faults, the yellow dashed line the caldera border, the red triangles the seismic stations, the purple stars the wells and the cyan circles the production units at the Miravalles geothermal field. The area defined by green lines is the main injection area.

The distribution of the final earthquake locations in the x- and y-directions are displayed in Figure 5.16. The same features that were at the surface of the block velocity model (Figure 5.9) are also included at the surface plot of the earthquake locations, e.g. the faults and caldera border. The predominant part of the detected earthquakes are positioned between x ∈ [404, 409] km and y ∈ [294, 301] km (Figure 5.16). Furthermore, most of the earthquakes seem to be located approximately

along two lines. The first line is parallel to the large normal fault (see Figure 2.4) in the center of Figure 5.16. In other words, from $[x, y] = [402, 292]$ km to $[x, y] = [411, 303]$ km. The second line is parallel to the NW-SE fault lines. That is from $[x, y] = [404, 300]$ km to $[x, y] = [407, 296]$ km.

Figure 5.17 shows a surface plot of the earthquake locations with the same features that were at the surface of the block velocity model (Figure 5.9), e.g. the faults and caldera border. The size and color of the circles indicate the magnitude of the events. It is clear that most of the events have a magnitude smaller than 2 (black small circles). The spread in the x- and y-directions becomes smaller and smaller for each increase in magnitude range. 5 of the 614 detected earthquakes have a magnitude larger than or equal to 3 (large red circles). These are most densely distributed. Two of these earthquakes are found inside the injection zone. Another two are situated where fluid withdrawal takes place. The final one is located close to the most western fault.

The depth distribution in the x- and y-directions for the locations obtained using the 3D velocity model are visualized in Figures 5.18a and 5.18b, while those for the constant velocity model in Figures 5.18c and 5.18d. In Figure 5.18 9 of the drilled wells at the Miravalles geothermal field are included. These are represented by black vertical lines. The majority of the seismic events for the 3D velocity model are located in the top 3 km (Figures 5.18a and 5.18b). The distribution of the earthquakes that are situated deeper than 3 km are more spread out than in the first three layers. Nonetheless, there seems to be some structure. In Figure 5.18a few earthquakes are found to the left of x equal to 403 km and the detected earthquakes appear to form a line, going from $[x, z] = [409, 0]$ km to $[x, z] = [402, 8]$ km. In the figure that shows the depth distribution in the y-direction, on the other hand, the locations are more spread out. However, there appears to be an alignment of earthquakes that form an arc-shaped structure. This structure starts at $[y, z] = [293, 8]$ km and reaches its maximum at approximately $[y, z] = [297, 3.5]$ km, before ending at $[y, z] = [301, 8]$ km. The locations for the constant velocity model, by contrast, are more equally distributed with depth (Figures 5.18c and 5.18d). This is also seen in the Figures 5.19a and 5.19b which show the number of events per layer for both of the velocity models. The layer with the most seismicity for the constant velocity model is the deepest one, while for the 3D velocity model is the second, i.e. the geothermal reservoir. In the latter, approximately 50 events occur in each of the layers at levels deeper than 2 km.

Figure 5.20 displays the distribution of travel time residuals. The red columns are the travel time residuals for the constant background velocity model (iteration zero) and the blue columns are for the final 3D velocity model[4]. The travel time residuals

---

[4]The reader is advised to take notice that the two different shades of blue are caused by the blue column overlapping with the red column.
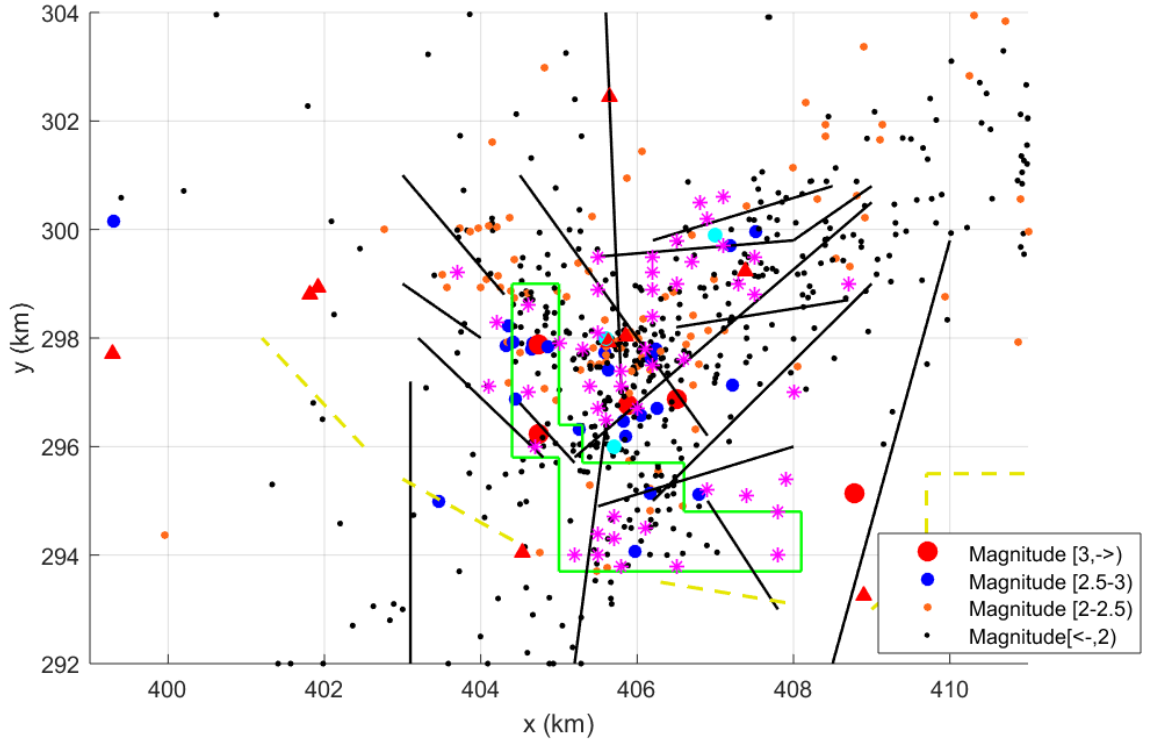
Figure 5.17: Surface plot of earthquake locations where the magnitude of the earthquake is indicated. The red circle indicates locations of events with a magnitude larger than or equal to 3, dark blue circles for a magnitude between 2.5 and 3, orange circles for a magnitude between 2 and 2.5, and black circles for a magnitude smaller than 2. The black lines are faults, the yellow dashed line the caldera border, the red triangles the seismic stations, the purple stars the wells and the cyan circles the production units at the Miravalles geothermal field. The area defined by green lines is the main injection area.

for the 3D velocity model (blue column) have a relatively high number of small residuals (from -0.01 to 0.01 s) and few large residuals.

When comparing the final earthquake locations obtained from the multiscale travel time tomography the ones determined by ICE (Figures 5.18 and 5.3), it appears that the events are distributed over a smaller area in the locations determined by ICE. In addition to this, in the locations determined by ICE, most of the seismicity is confined to the first layer and there are no events deeper than 6 km (Figure 5.3).
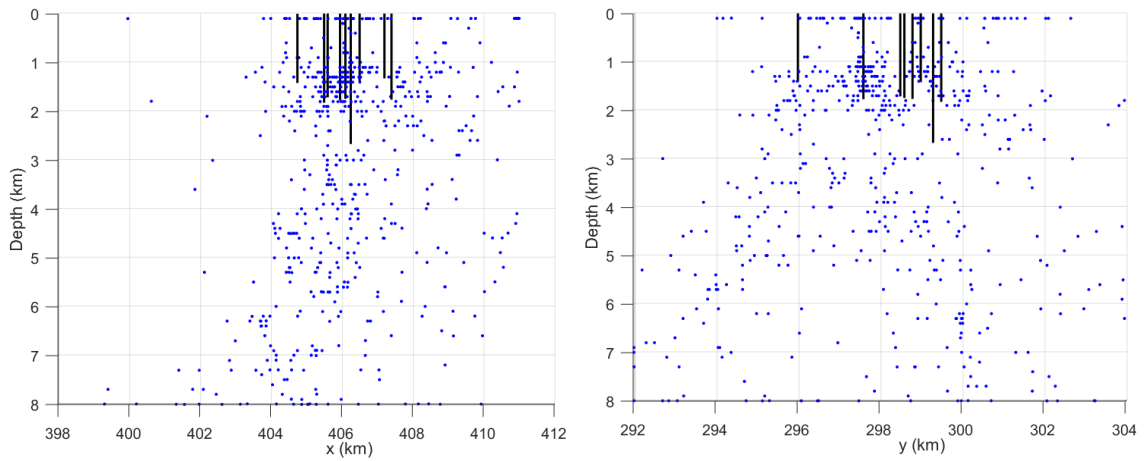
(a) Depth distribution in the x- and z-directions for the 3D velocity model.

(b) Depth distribution in the y- and z-directions for the 3D velocity model.
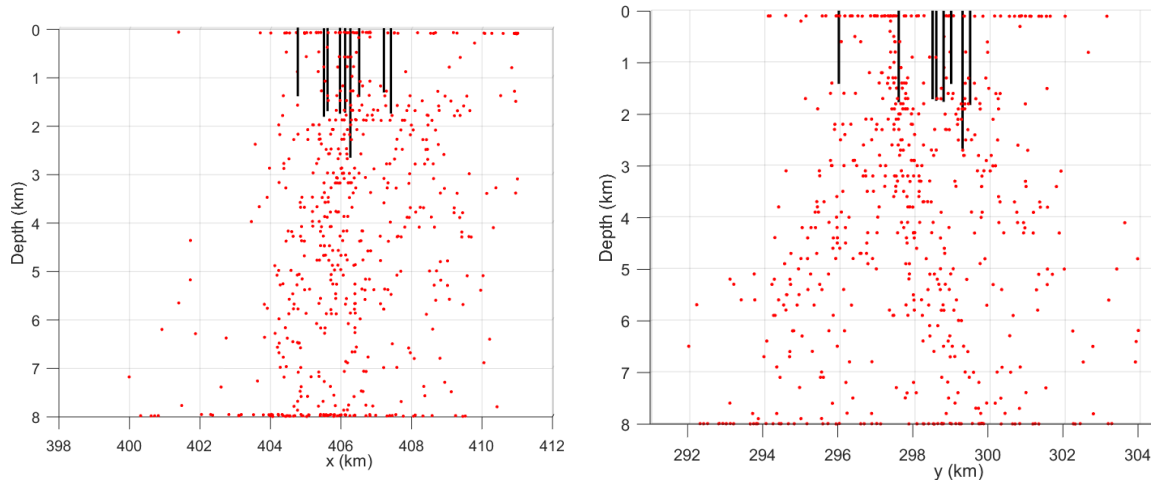
(c) Depth distribution in the x- and z-directions for the constant velocity model.

(d) Depth distribution in the y- and z-directions for the constant velocity model.

Figure 5.18: Depth distribution of earthquakes for the final 3D velocity model (blue locations) and for the constant velocity model (red locations). The black lines in the figures represent wells.
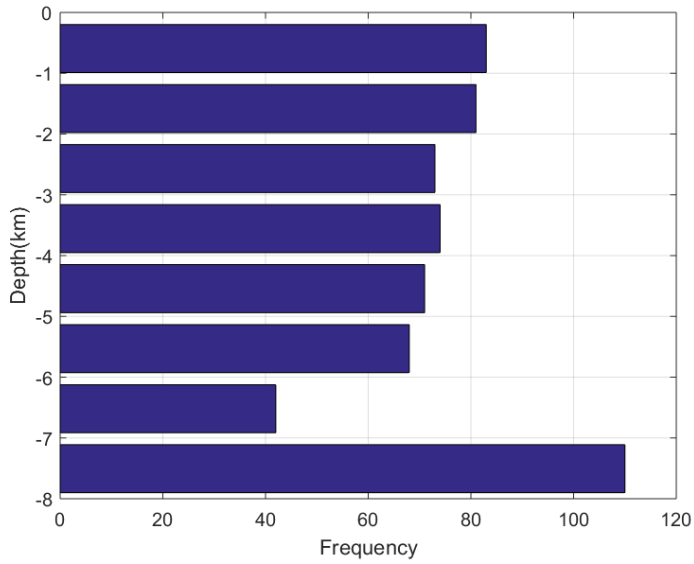
(a) Number of events per layer obtained by using the constant
velocity model.
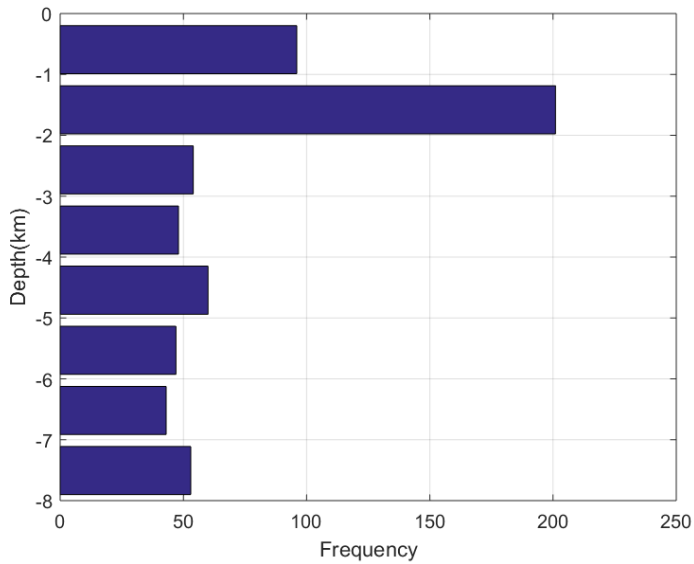
(b) Number of events per layer obtained by using the final 3D
velocity model.

Figure 5.19: Depth distribution for iteration zero and iteration 13.
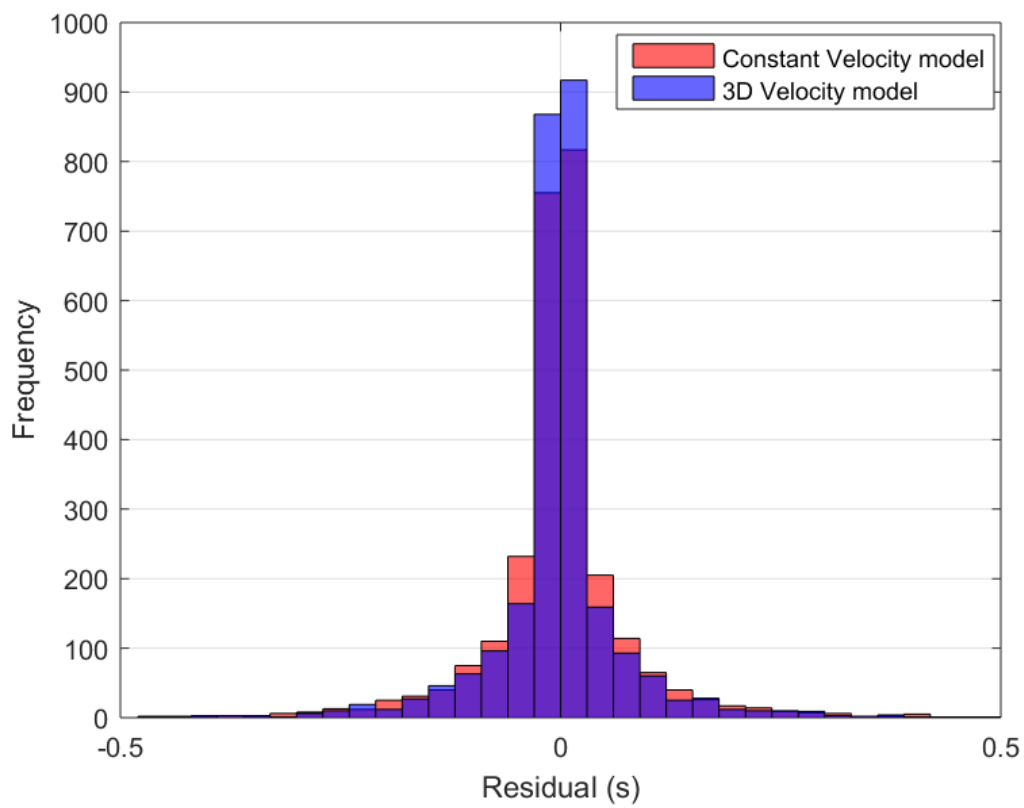
Figure 5.20: Histogram of the travel time residuals for the constant velocity model (red column) and the final 3D velocity model (blue column).

5.6   Resolution Test

A checkerboard test was performed on the final source locations[5]. This was conducted in order to investigate how the resolution is for the fine tomography, i.e. step three of the multiscale travel time tomography.

The heterogeneous input model for this synthetic test consists of an alternating pattern of positive and negative anomalies of a magnitude $\pm 10\%$ (see Figure 4.11 for an illustration of the alternating pattern). The dimensions of the cells in the constant background model and the heterogeneous input model are $l_x \times l_y \times l_z = 2 \times 2 \times 1$ km. This is equal to those of the final parameterization of the multiscale travel time tomography.
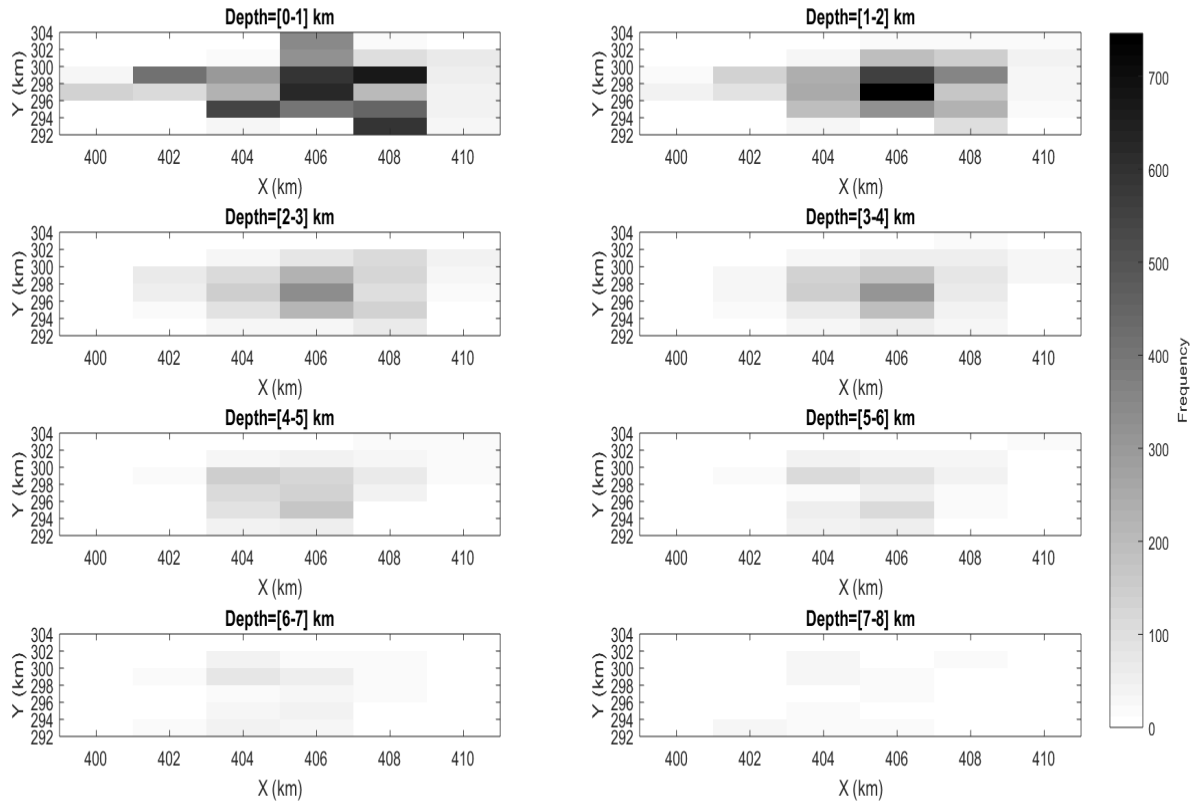
Figure 5.21: The coverage for each layer of the source locations obtained from the final 3D multiscale travel time tomography and the real receiver locations at the Miravalles geothermal field. The dimensions of the cells are $2 \times 2 \times 1$ km.

_____

[5]An explanation of how to conduct a synthetic test was discussed in section 4.9

The acquisition geometry, i.e. the location of sources and receivers, gives rise to a total of 2656 rays propagating through the background and input velocity models. The coverage of this setup is displayed in Figure 5.21, and is best in the two layers closest to the surface. The reason for this is that this is where the predominant part of the earthquakes are located. The coverage decreases with depth, as well as towards the edges of the layers (the whiter the cells, the poorer the coverage).
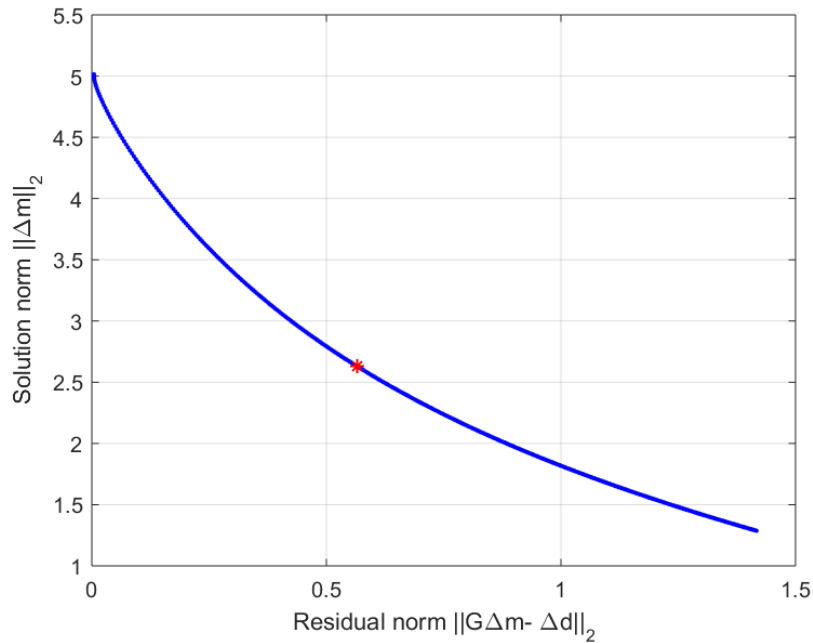
Figure 5.22: The L-curve for the checkerboard test for the final source locations obtained using 3D multiscale travel time tomography and the real receiver locations from the Miravalles geothermal field. The red star shows the location that corresponds to the best damping parameter ($\alpha = 0.3006$).

The L-curve is shown in Figure 5.22. The best damping parameter was chosen to be 0.3006 which corresponds to the location of the red star. This yields the relative change in velocity for each layer shown in Figure 5.23.

The heterogeneous input model is best recovered at the two top layers and in the center of the layers below. This means that the resolution is best where the coverage is high. The magnitude of recovery decreases with increasing depth and smearing of the anomalies takes place. The checkerboard test suggests that the main features of the 3D multiscale travel time tomography presented in the previous section are reasonably well resolved.
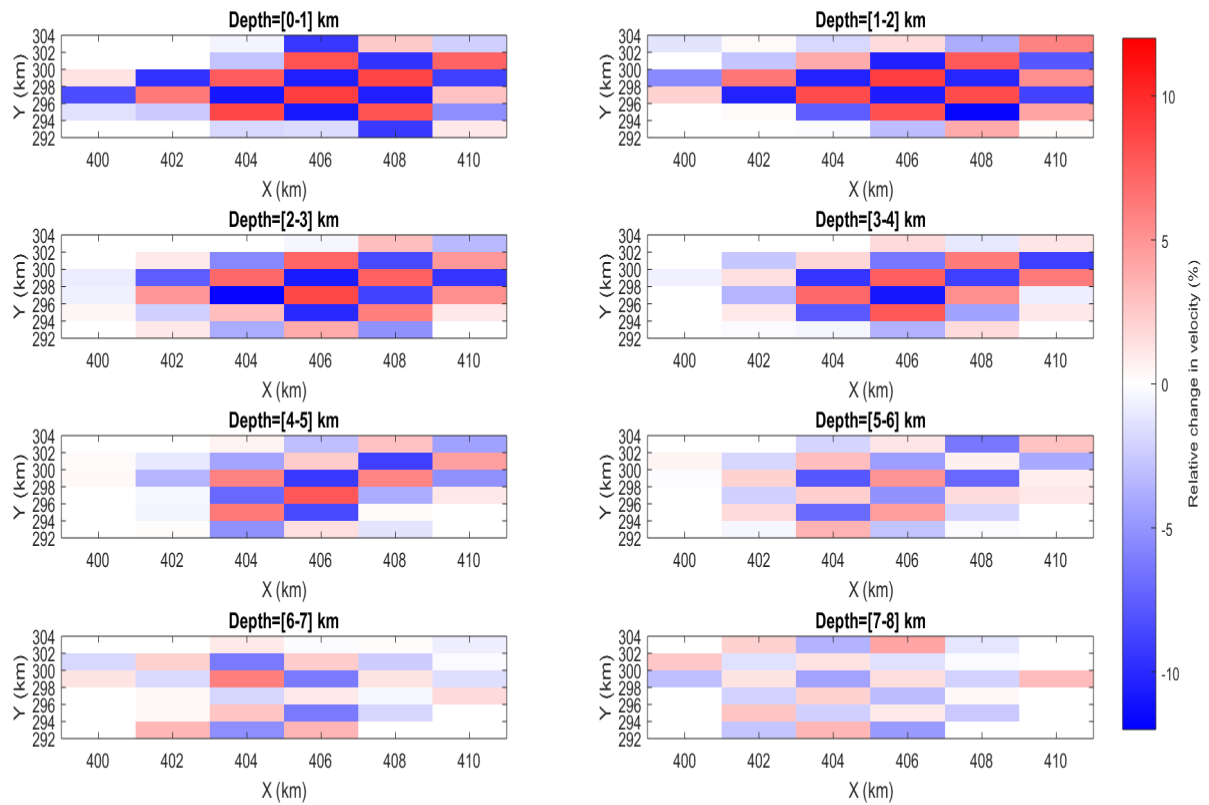
Figure 5.23: Relative change (%) in velocity for each layer using the checkerboard test on the final source locations obtained from the 3D multiscale travel time tomography and the real receiver locations at the Miravalles geothermal field. The dimensions of the cells are $2 \times 2 \times 1$ km.

Chapter 6

Discussion

6.1   Overview

In this chapter the results that were presented in chapter 5 are discussed. The main features of the 3D velocity model at the Miravalles geothermal field are investigated in section 6.2. This includes an interpretation of the reservoir in subsection 6.2.1, the surface in subsection 6.2.2 and the intrusion in subsection 6.2.3. Section 6.3 is dedicated to discussing the seismic activity at the Miravalles geothermal field and the improvement in fit from the constant background velocity model to the 3D velocity model. It also looks at the differences between the locations determined by the 3D velocity model obtained in this thesis and those determined by ICE in SEISAN. Finally, some ideas for future work are given in section 6.4.

6.2   The 3D Velocity Model

The velocity structure of the subsurface can yield important information regarding geological features, as well as physical properties of the rocks and rock fluids. The reason for this is that the velocity of a wave propagating through a layer rock depends on several factors, including porosity, water saturation, effective pressure, temperature and the chemical composition of fluids. In general, the velocity decreases under higher temperatures and levels of porosity [Timur, 1977; Schön, 2015], while it increases under higher saturation and effective pressure levels [Toksöz et al., 1976; Schön, 2015; Schuler et al., 2015]. As a consequence, travel time tomography can provide useful information to the operators of a geothermal field.

The first step of the multiscale travel time tomography consisted in determining a 1D velocity model for the Miravalles geothermal field. One of the central characteristics of the final 1D model (cyan colored line in Figure 5.8) is the high velocity layer that

is located between 1 and 2 km deep. In addition, it was discovered that directly above and below this layer are ones with lower velocities. The velocities increase for depths greater than 4 km.

The 3D velocity model shown in Figure 5.9 is the final result of the multiscale travel time tomography. The main features of the final 1D velocity model are still evident in the 3D velocity model.

6.2.1   The Reservoir

The high velocity layer situated between depths of 0.8 and 2.1 km correspond to the depth of the reservoir and is the layer that is the main source of production at the Miravalles geothermal field (see Figures 5.18a and 5.18b). It is therefore considered the geothermal reservoir in this thesis.

The reservoir consists of volcanic material. This means that it is likely that it has naturally high levels of porosity. Circulation of hydrothermal fluids in the reservoir can also improve the porosity even further [Farooqui et al., 2009].

The aquifer gets recharged by meteoric water from the northeastern part of the field and is injected with fluid from the southern and western parts. Injection and extraction of fluid from the reservoir can change the local stress regime and lead to a fracturing of the reservoir. The bulk modulus is the reciprocal of compressibility of a material and gas can be more compressed than water. This entails that a rock that has pores containing water can have higher velocities than ones with pores containing gas [Schön, 2015]. Assuming the density changes are smaller[1], it is possible that the higher velocities in the reservoir are a result of it originally being a low permeability, porous rock with pores (partially) filled with gases. After some time of production, the permeability improved through utilization of the geothermal resource. This can have caused the gas filled pores to be filled with water.

Figure 5.12 shows a slice of the reservoir. It is evident that the velocities decrease as one moves towards the western part of the Miravalles geothermal field. It also illustrates that the highest velocities (colored orange and yellow in Figure 5.12) within the reservoir are restricted towards the southern and western parts of the field. This correlates with the caldera border and la Fortuna graben. La Fortuna graben is open for lateral discharge of volcanic sediments towards the south. Due to the existence of the graben structure and the shape of the reservoir, it is likely that the latter originates from some type of volcanic material that formed within the Guayabo caldera and has moved towards the south. These two structures thus act as natural borders for the reservoir.

---

[1]This assumption will function as a basis of the interpretations of higher velocities as a result of the change in content of pores carried out in the rest of this thesis

The production zone is surrounded by three zones of higher velocities (orange and yellow areas in Figure 5.12). The first zone is found between $x \in [407, 409]$ km and $y \in [300, 302]$ km. It corresponds to the location of the main inflow of meteoric water. Higher saturation levels can thus be expected there, something that can yield higher velocities. Another possible explanation is that it is caused by heterogeneity within the crust.

The second zone of higher velocities is situated between x $\in [401, 406]$ km and y $\in [296, 299]$ km. Finally, the third zone is between x $\in [407, 409]$ km and y $\in [292, 296]$ km (Figure 5.12). These two zones overlap with the main injection area, as well as where some of the lowest temperatures of the field are found (Figure 2.5). Injection of fluid will lead to the fracturing of rock and therefore give higher saturation levels. A possible explanation for the higher velocities in these areas may be that they are caused by the combined effect of the lower temperatures and the injection of fluid.

The second high velocity zone is relatively large and it extends from the center of the field almost all the way to the most western part of the reservoir. There are three seismic stations (marked by red triangles in Figure 5.12) located in the western part of the field. It is thus possible that there is some smearing of the second high velocity zone towards the west.

The highest velocities in the reservoir appear in the third high velocity zone. This is also where most of the injection of fluid takes place. The temperature of the fluid injected there is almost 30°C lower than in the western part of the injection zone. It is consequently reasonable to assume that this area will have the highest saturation and the lowest temperatures. There is also a correlation between the high velocity area and the location of la Fortuna graben. This can therefore indicate that also this structure is being imaged.

The seismically most active layer is located approximately 1 to 2 km deep (Figure 5.19b). This means that the majority of the earthquakes are found within the reservoir where the main production at the Miravalles geothermal field happens.

Nearly all of the events are clustered in the center of the production zone, i.e. where fluid is extracted (Figure 5.14). Fluid withdrawal from the reservoir can lead to a deflation of the reservoir. It consequently affects the local stress regime, sometimes yielding seismic activity. Another possibility is that at least some of the earthquakes are due to high temperatures mixing together with high pore pressures. This is called thermal cracking and is a phenomenon that causes the permeability of the geothermal reservoir to increase [Ghassemi, 2012].

The seismicity is low directly above and below the reservoir (Figures 5.18a and 5.18b). A probable reason for this is that these rock layers may have high porosity, yet low permeability. The movement of fluid is thus prevented. In other words, seismic events associated with volume changes could be prevented. One could, how-

ever, expect earthquakes to occur on the boundaries between the reservoir and the surrounding rock because these are zones of structural weakness.

6.2.2 The Surface

Above the reservoir there is a layer of lower velocity (Figure 5.9). A part of this layer is the cap rock which is close to impermeable and keeps the heated fluid at depth. It is likely that this layer has a porosity that is comparable to that of the reservoir, but it is possibly not as fractured; it has high porosity and low permeability. This means that the pores can contain gas, making the velocity in the layer lower. The top layer also contains clay and lacustrine deposits, both of which typically have lower velocities [Schön, 2015].

6.2.3 The Intrusion

There is an ellipsoid-shaped structure that is 4 to 8 km deep for $x \in [402, 407]$ km and $y \in [293, 301]$ km (Figure 5.10). This structure is localized approximately in the center of the caldera.

According to Schuler et al. [2015], an intrusive body that cools slowly will have a high density and thus high velocities. The higher velocities and the structure of it can therefore be interpreted as an intrusive body that has cooled slowly. It is, however, also possible that this is an artifact of the tomography, as the coverage of the fine tomography is best in the center of the deeper layers (Figure 5.21). In order to determine this, it is advisable to investigate this structure even further through employing denser station coverage and more data.

The ellipsoid-shape in the velocity model is also seen in the depth distribution of the earthquakes in the y-direction (Figure 5.18b). This was referred to as an arc-shape in chapter 5. A plausible cause for these earthquakes is the cooling of the intrusion, since this leads to a contraction of the intrusion and the surrounding rock.

The distribution of earthquake locations with depth is, nonetheless, asymmetrical in the x- and y-directions. In the plot of the depth distribution in the x-direction, the earthquake locations are located on a diagonal going from [x,z]=[409, 0] km to [x,z]=[402, 8] km and not on an arc-structure. A possible connection between the spread of hypocenters with depth in the x- and y-directions is that there is a fault that is parallel to the diagonal in the x-direction, and that it reaches the intrusion at depth. Figure 6.1 is a visual representation of how the diagonal fault (blue plane) can intersect with the intrusion (red dome).
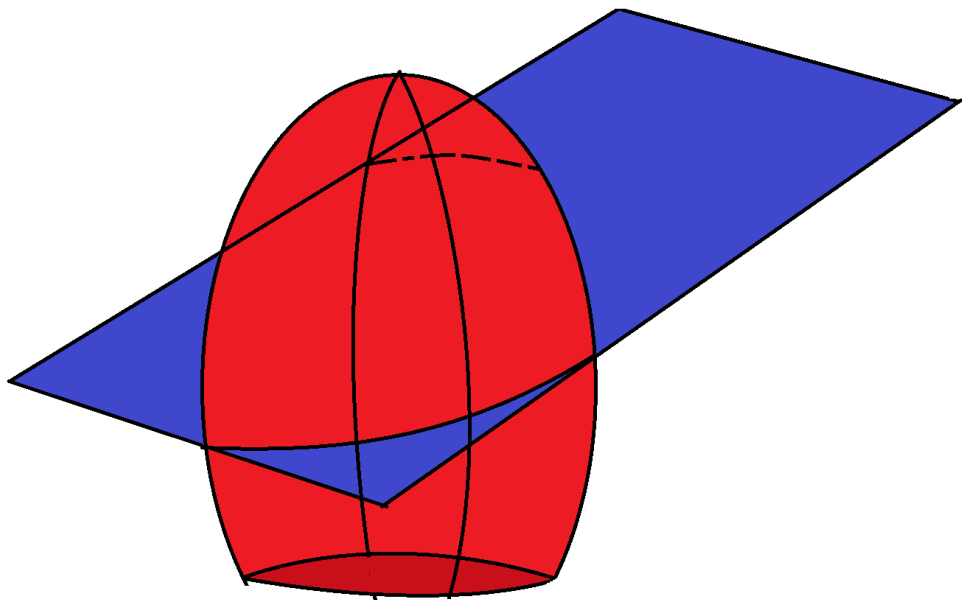
Figure 6.1: A sketch of how a diagonal fault (blue plane) intersects with the intrusion (red dome).

6.3   Seismicity

The stress field at the Miravalles geothermal field is complex due to the combination of regional tectonics and local effects, such as the injection and withdrawal of fluid from the subsurface.

There was hardly any seismicity detected at the Miravalles geothermal field prior to the development of the geothermal power plant, as prior to this there were no seismic stations in the area [Linkimer et al., 2018]. The number of earthquakes was also small during the first years of production. After the first decade, however, it increased dramatically (Figure 2.7). This makes it likely that the seismic activity is caused by the utilization of the geothermal resource. The reason this lies in that the local stress regime is sensitive to the addition and extraction of fluids from the subsurface. Changes in the local stress regime can induce rock failure, i.e. earthquakes, which can generate fractures. These fractures are probably the main reason why the Miravalles geothermal field is successful, as it depends on the injection of fluids that circulate in the reservoir towards the production wells and get heated up at the same time.

The majority of the determined earthquake locations are situated inside the Guayabo caldera (Figure 5.16). Within this area, there is a lot of seismic activity in the center where the main production takes place. This is west of the western injection sector. In addition to the cluster of earthquakes in the center of the field, they seem to occur on two lines parallel to geological structures (Figure 5.16). The first one extends from the northeast towards the southwest and is parallel to the large normal fault. This also correlates with the location of the main inflow of water and its flow path. Seismic events originating along this fracture can therefore be interpreted as a result of movement of fluids that get heated up which lead to thermal cracking of the rocks. The second line is parallel to the structure system that moves from the northwest towards the southeast. This suggests that this is an active fracture system.

Figure 5.17 shows the link between the location of earthquakes and their magnitude. It is clear that detected earthquakes with a magnitude smaller than 2 are the most common. Furthermore, the spread in location gets progressively smaller as the magnitude increases and clusters around the center of the field. The locations of the largest earthquakes (magnitude larger than or equal to 3) indicate that there is a correlation between them and the utilization of the geothermal resource. Two of five seismic events are located in the injection zone and two in the production zone.

6.3.1   Improvement in Earthquake Locations

In this thesis the mean misfit for all earthquake locations was used as a measure of fit for the velocity model. From iteration zero, i.e. the constant velocity model,

to iteration 13, i.e. the final 3D velocity model, the misfit reduced by almost 15 %. The 3D velocity model also leads to a growth in the number of smallest travel time residuals and a decrease of larger ones (Figure 5.20). This can suggest that the final velocity model has more accurately discovered the location of earthquakes in comparison to those found by the constant background velocity model. The change in depth distribution of the detected earthquakes can also be considered an improvement. Originally, the number of earthquakes per layer was relatively equally distributed for the constant velocity model. By contrast, the 3D velocity model show a clear grouping of seismic events in the second layer. This is where the reservoir is located, and the production and injection associated with the utilization of the geothermal resource takes place. It therefore looks like the earthquake locations move towards this layer from the ones determined by the constant velocity model to those of the 3D velocity model. Normally a large number of seismic events at the production and injection levels, as well as a decrease in it with depth would be expected. This is what is seen in the final earthquake locations.

Comparing the earthquake locations for the final 3D velocity model with the ones determined by ICE, it is clear that the seismicity is spread out over a larger area in the former and generally deeper (Figures 5.18a,5.18b, 5.16 and 5.3). The locations determined in this thesis also suggest, furthermore, that the second layer is the most seismically active (Figure 5.19b). Based on the locations determined by ICE, on the other hand, the first layer is the one with the most seismic events (Figure 5.3d).

The predominant part (195 events) of the earthquakes situated in the first layer are located on the surface, i.e. they have a depth equal to 0 km, in the locations determined by ICE. This suggests that the velocity model in the first layers is too low. If the velocity was higher, the events would be found further down. There are no events found at the surface according to the locations determined in this thesis. Nonetheless, there are some at a depth of 0.1 km (65 events). This comparison therefore suggests that there could be a high velocity layer located close to the surface.

Another possible explanation for the shallower earthquake locations determined by ICE is that they use all the available data from the 45 seismic stations, while in this thesis only 9 stations were employed. For shallow events, the ray that travels from the source to a receiver located far away is close to horizontal, this can lead to a limited depth resolution.

A final plausible reason for the difference in earthquake locations may be that they are found using two different velocity models and location methods. The locations determined by ICE use the HYP program in SEISAN, while the ones found in this thesis employs P-wave single difference. Several tests could be implemented in order to investigate how P-wave single difference compares to conventional methods like those used in SEISAN for earthquake locations. Doing this, however, was beyond

the scope of this thesis.

6.4   Future Work

6.4.1   General

In section 4.10 it was mentioned that the coverage of the area plays a vital role in the resolution of the tomography. In order to obtain an improved inversion result it is recommend to use a denser network of seismic stations that covers the entire Miravalles geothermal field extending beyond the reservoir boundary, as well as to use more data to improve illumination (ideally 20 000-30 000 travel times).

Furthermore, if one has continuous data it would be possible to investigate the noise at the seismic stations. Information from this could be implemented in the inversion in order to account for errors in the selection of first-arrival times.

6.4.2   Body Wave Travel Time Tomography

In the work administered in this thesis, only the P-wave data was used. It would, however, be useful to perform travel time tomography for both the P-waves and the S-waves, and to investigate how the P/S ratios vary. The reason why is that the velocity for the S-waves is slower in a medium that contains a fluid. This could therefore help to better image the reservoir and locate areas that contain a large amount of fluids. In addition to this, one should take attenuation into account because this will affect the results.

6.4.3   Earthquake Location

In this thesis a new earthquake location method called P-wave single difference was developed. In the future it might be beneficial to compare this method with conventional earthquake location methods. It could also be interesting to implement the earthquake location method called double difference location, as several studies have found that it improved the locating of earthquakes.

6.4.4   Moment Tensor

Another possibility could be to investigate the moment tensor of some of the largest earthquakes. This would enhance the understanding of the orientations of the faults and the local stress regime, and provide useful knowledge about the behavior of the reservoir.

6.4.5   Time Dependence

It could also be beneficial to study the time dependency of seismic events, and to correlate the time of the events with production and injection data. The former

can be used to examine how the seismicity in an area has changed with time. The latter, on the other hand, can help to determine if it is injection, production or thermal cracking that is the main source of earthquakes. It would consequently provide a better understanding of how the reservoir is affected by the utilization of the geothermal resource.

6.4.6   Reservoir Management

Finally, through the development of a rock physics model a reservoir model could be made or an existing one improved. This could lead to a more efficient management of a reservoir which ultimately is one of the main goals of geothermal reservoir engineering.

Chapter 7

Conclusion

The purpose of this thesis was to investigate if multiscale travel time tomography and earthquake locations could improve the understanding of the Miravalles geothermal field located in Costa Rica. In particular, a main goal was to find out how earthquake locations and the velocity model of the subsurface correlate with the geothermal reservoir and its structure.

Achieving these goals was done through the interpretation of results from multiscale travel time tomography in combination with a new earthquake location method. The locations of the detected earthquakes provide viable information about active fault systems and permeable zones. They can also be used to better understand how the utilization of the geothermal reservoir affects the local stress regime.

Even though the number of stations and detected earthquakes limit the overall resolution of the multiscale travel time tomography, this approach yields new insight regarding the Miravalles geothermal field. The results obtained in this thesis indicate that the extent of the Miravalles geothermal reservoir and the seismicity are limited by the caldera border and la Fortuna graben. They furthermore suggest that there is a parallel between most of the seismic activity, the reservoir, and the area where the main utilization, i.e. the adding and extraction of fluid, takes place at the Miravalles geothermal field. Some events can also be interpreted to be thermally induced. These events propably increase permeability and therefore production.

The determined hypocenter locations also contribute to a clearer understanding of the implications of both injection and production. It has been claimed that the latter causes the majority of the seismic activity. The basis for this interpretation was the correlation that was discovered between the position of the earthquakes and the production wells.

The outcome of the multiscale travel time tomography gives the first tomographic

image of the Miravalles geothermal reservoir. It indicates that the reservoir is thicker towards the east and gradually becomes thinner towards the west. The higher seismic velocities in the reservoir were believed to be a result of the production and hydrothermal alteration which lead to improved permeability, causing a shift from gas filled to water filled pores and fractures.

The high velocity ellipsoid-shaped structure found at a greater depth than the reservoir was interpreted as a possible intrusion. The limited coverage of the travel time tomography at depth could, however, also mean that this is an artifact of the tomography. In order to determine this, it is advised to use a greater amount of earthquake data, preferably 20 000- 30 000 travel times, and to improve the station coverage to better image the reservoir and this deeper structure. It is nonetheless evident that the information obtained from the results in this thesis can be useful for the operators at the Miravalles geothermal field, as it could help to increase the understanding of how the reservoir works. This should ultimately lead to improved production.

Bibliography

Aster, R. C., Borchers, B., and Thurber, C. H. (2005). *Parameter Estimation and Inverse Problem.* Elsevier Academic press, 1 edition.

Banks, D. (2012). *An introduction to Thermogeology ground source heating and cooling*, volume 30. Wiley-Blackwell.

Barbier, E. (2002). Geothermal energy technology and current status: an overview. *Renewable and Sustainable Energy Reviews*, 6:3–65.

Bertani, R. (2012). Geothermal power generation in the world 2005-2010 updated report. *Geothermics*, 41:1–29.

Bertani, R. (2016). Geothermal power generation in the world 2010–2014 update report. *Geothermics*, 60:31–43.

Bijwaard, H., Spakman, W., and Engdahl, E. R. (1998). Closing the gap between regional and global travel time tomography. *Journal of Geophysical Research: Solid Earth*, 103:30055–30078.

Bording, R. P., Gersztenkorn, A., Lines, L. R., Scales, J. A., and Treitel, S. (1987). Applications of seismic travel-time tomography. *Geophysical Journal International*, 90:285–303.

Breede, K., Dzebisashvili, K., Liu, X., and Falcone, G. (2013). A systematic review of enhanced (or engineered) geothermal systems: past, present and future. *Geothermal Energy*, 1:1–27.

British Petroleum (2018). BP Statistical Review of World Energy. https://www.bp.com/content/dam/bp/business-sites/en/global/corporate/pdfs/energy-economics/statistical-review/bp-stats-review-2018-full-report.pdf. [Online; accessed 25.04.19].

Brodsky, E. E. and Lajoie, L. J. (2013). Anthropogenic Seismicity Rates and Operational Parameters at the Salton Sea Geothermal Field. *Science*, 341:543–546.

Cerveny, V. (2001). *Seismic ray theory.* Cambridge University Press, 1 edition.

Chapman, C. H. (2004). *Fundamentals of seismic wave propagation.* Cambridge University Press, 1 edition.

Cubasch, U., Wuebbles, D., Chen, D., Facchini, M. C., Frame, D., Mahowald, N., and Winther, J. G. (2013). Introduction. In *Climate Change 2013: The Physical Science Basis.* Cambridge University Press. `https://www.ipcc.ch/site/assets/uploads/2017/09/WG1AR5_Chapter01_FINAL.pdf` [Online; accessed 19.04.19].

Datuin, R. T. and Troncales, A. C. (1986). Philippine geothermal resources: General geological setting and development. *Geothermics*, 15:613–622.

Dipippo, R. (2007). *Geothermal Power Plants Principles, Application, Case Studies and Environmental Impact.* Elsevier, 2 edition.

Ellabban, O., Abu-Rub, H., and Blaabjerg, F. (2014). Renewable energy resources: Current status, future prospects and their enabling technology. *Renewable and Sustainable Energy Reviews*, 39:748–764.

Farooqui, M. Y., Hou, H., Li, G., Machin, N., Neville, T., Pal, A., Shrivastva, C., Wang, Y., Yang, F., Yin, C., Zhao, J., and Yang, X. (2009). Evaluating volcanic reservoirs. `https://www.slb.com/~/media/Files/resources/oilfield_review/ors09/spr09/evaluating_volcanic_reservoirs.pdf`. [Online; accessed 12.05.19].

Fernando, M. and Martí, J. (2018). Proposal for an initial development strategy for the Borinquen geothermal zone (Cañas Dulces, Costa Rica). *Renewable Energy*, 118:409–424.

Fichtner, A., Trampert, J., Cupillard, P., Saygin, E., Taymaz, T., Capdeville, Y., and Villaseñor, A. (2013). Multiscale full waveform inversion. *Geophysical Journal International*, 194:534–556.

Fukao, Y., Obayashi, M., Inoue, H., and Nenbai, M. (1992). Subducting slabs stagnant in the mantle transition zone. *Journal of Geophysical Research: Solid Earth*, 97:4809–4822.

Gaucher, E., Schoenball, M., Heidbach, O., Zang, A., Fokker, P. A., Van Wees, J. D., and Kohl, T. (2015). Induced seismicity in geothermal reservoirs: Physical processes and key parameters. In *Proceedings World Geothermal Congress 2015 Melbourne, Australia.*

Ghassemi, A. (2012). A review of some rock mechanics issues in geothermal reservoir development. *Geotechnical and Geological Engineering*, 30:647–664.

González-Vargas, C., Moya-Rojas, P., Sánchez-Rivera, E., Vallejos-Ruiz, O., and Yock-Fung, A. (2005). Evolution of the Miravalles Geothermal Field in Costa

Rica after Ten Years of Exploitation. In *Proceedings World Geothermal Congress 2005*.

Harsh, K. G. and Sukanta, R. (2007). *Geothermal Energy an alternative resource for the 21st century*. Elsevier, 1 edition.

Havskov, J. and Ottemöller, L. (1999). Seisan earthquake analysis software. *Seismological Research Letters*, 70:532–534.

Havskov, J. and Ottemöller, L. (2010). *Routine Data Processing in Earthquake Seismology*. Springer.

Huene, R., Ranero, C. R., Weinrebe, W., and Hinz, K. (2000). Quaternary convergent margin tectonics of Costa Rica, segmentation of the Cocos Plate, and Central American volcanism. *Tectonics*, 19:314–334.

Hutchings, L., Bonner, B., Jarpe, S., and Singh, A. (2014). Micro-earthquake Analysis for Reservoir Properties at the Prati-32 Injection Test, The Geysers, California. volume 38, pages 519–526.

IRENA, OECD/IEA and REN21 (2018). Renewable energy policies in a time of transition. `https://www.irena.org/-/media/Files/IRENA/Agency/Publication/2018/Apr/IRENA_IEA_REN21_Policies_2018.pdf`. [Online; accessed 22.02.19].

Juncu, D., Árnadóttir, T., Geirsson, H., Gudmundsson, G. B., Lund, B., Gunnarsson, G., Hooper, A., Hreinsdóttir, S., and Michalczewska, K. (2018). Injection-induced surface deformation and seismicity at the Hellisheidi geothermal field, Iceland. `https://doi.org/10.1016/j.jvolgeores.2018.03.019`. [Online; accessed 02.05.19].

Knoblauch, T. A. K., Trutnevyte, E., and Stauffacher, M. (2019). Siting deep geothermal energy: Acceptance of various risk and benefit scenarios in a Swiss-German cross-national study. *Energy Policy*, 128:807–816.

Kristmannsdóttir, H. and Ármannsson, H. (2003). Environmental aspects of geothermal energy utilization. *Geothermics*, 32:451–461.

Linkimer, L., Arroyo, I. G., Alvarado, G. E., Arroyo, M., and Bakkar, H. (2018). The National Seismological Network of Costa Rica (RSN): An Overview and Recent Developments. *Seismological Research Letters*, 89:392–398.

Lomax, A., Michelini, A., and Curtis, A. (2009). Earthquake location, direct, global-search methods. In Meyers, R. A., editor, *Encyclopedia of Complexity and Systems Science*, chapter 150, pages 2449–2472. Springer.

Lu, S. (2018). A global review of enhanced geothermal system (EGS). *Renewable and Sustainable Energy Reviews*, 81:2902–2921.

Lund, J. W., Bertani, R., and Boyd, T. L. (2015). Worldwide geothermal energy utilization 2015. *Geothermal Resources Council Transactions*, 39:79–92.

Marshak, S. (2012). *Earth portrait of a planet*. W.W. Norton, New York.

Massachusetts Institute of Technology (2006). The future of geothermal energy. `https://www1.eere.energy.gov/geothermal/pdfs/future_geo_energy.pdf`. [Online; accessed 17.04.19].

Minissale, A. (1991). The Larderello geothermal field: a review. *Earth-Science Reviews*, 31:133–151.

Moeck, I. S. (2014). Catalog of geothermal play types based on geologic controls. *Renewable and sustainable Energy Reviews*, 37:867–882.

Moya, P., Nietzen, F., Castro, S., and Taylor, W. (2011). Behavior of the geothermal reservoir at the Miravalles geothermal field during 1994-2010. `https://orkustofnun.is/gogn/unu-gtp-sc/UNU-GTP-SC-12-22a.pdf`. [Online; accessed 23.03.19].

Moya, P. and Yock, A. (2007). Assessment and development of the geothermal energy resources of Costa Rica. `https://orkustofnun.is/gogn/unu-gtp-sc/UNU-GTP-SC-04-11.pdf`. [Online; accessed 11.02.19].

National Research Council (2013). *Induced Seismicity Potential in Energy Technologies*. National Academies Press.

Nietzen, F. and Solís, L. (2015). Production-Injection at the Costa Rica Geothermal Fields: Miravalles and Pailas. In *Proceedings World Geothermal Congress 2015*.

Niiranen, J. (1999). Fast and accurate symmetric Euler algorithm for electromechanical simulations NOTE: The method became later known as Symplectic Euler. In *Proceedings of the Electrimacs'99*, volume 1, pages 71–78.

Nolet, G. (2008). *A Breviary of Seismic Tomography Imaging the Interior of the Earth and Sun*. Cambridge University Press.

Olasolo, P., Juárez, M. C., Morales, M. P., D´Amico, S., and Liarte, I. A. (2016). Enhanced geothermal systems (egs): A review. *Renewable and Sustainable Energy Reviews*, 56:133–144.

Pujol, J. (2003). *Elastic Wave Propagation and Generation in Seismology*. Cambridge University Press.

Purnomo, B. J. and Pichler, T. (2014). Geothermal systems on the island of Java, Indonesia. *Journal of Volcanology and Geothermal Research*, 285:47–59.

Rawlinson, N., Pozgay, S., and Fishwick, S. (2010). Seismic tomography: A window into deep Earth. *Physics of the Earth and Planetary Interiors*, 178:101–135.

Reinsch, T., Dobson, P., Asanuma, H., Huenges, E., Poletto, F., and Sanjuan, B. (2017). Utilizing supercritical geothermal systems: a review of past ventures and ongoing research activities. *Geothermal Energy*, 5.

REN21 (2018). Renewables 2018 global status report. `http://www.ren21.net/wp-content/uploads/2018/06/17-8652_GSR2018_FullReport_web_final_.pdf`. [Online; accessed 13.04.19].

Ritchie, H. and Roser, M. (2019). Energy production & changing energy sources. *Our World in Data*. `https://ourworldindata.org/energy-production-and-changing-energy-sources` [Online; accessed 17.02.19].

Rojas, L. C. (2003). Miravalles geothermal field, Costa Rica- evidence of thermal evolution and comparison of the mineralogy of an acid well and a neutral well. `https://orkustofnun.is/gogn/unu-gtp-report/UNU-GTP-2003-06.pdf`. [Online; accessed 08.01.19].

Ruiz, O. V. (2013). THE MIRAVALLES GEOTHERMAL SYSTEM, COSTA RICA. `https://orkustofnun.is/gogn/unu-gtp-sc/UNU-GTP-SC-16-32.pdf`. [Online; accessed 17.03.19].

Sánchez-Rivera, E. and Vallejos-Ruiz, O. (2015). Costa Rica Country Update Report. In *Proceedings World Geothermal Congress 2015*.

Sauer, T. (2014). *Numerical Analysis*. Pearson Education Limited, 2 edition.

Schoenball, M., Davatzes, N. C., and Glen, J. M. G. (2015). Differentiating Induced and Natural Seismicity Using Space-Time-Magnitude Statistics Applied to the Coso Geothermal Field. *Geophysical Research Letters*, 42:6221–6228.

Schön, J. H. (2015). *Physical Properties of Rocks: Fundamentals and Principles of Petrophysics*. Elsevier Science, 2 edition.

Schuler, J., Greenfield, T., White, R. S., Roecker, S. W., Brandsdóttir, B., Stock, J. M., Tarasewicz, J., Martens, H. R., and Pugh, D. (2015). Seismic imaging of the shallow crust beneath the Krafla central volcano, NE Iceland. *Journal of Geophysical Research: Solid Earth*, 120:7156–7173.

Sánchez-Rivera, E., Vallejos-Ruiz, O., and González-Vargas, C. (2010). Maintenance of the Production in the Miravalles Geothermal Field, Costa Rica: New Productive Zones . In *Proceedings World Geothermal Congress 2010*.

Stein, S. and Wysession, M. (2003). *An Introduction to Seismology, Earthquakes, and Earth Structure*. Blackwell Publishing, 1 edition.

Stober, I. and Bucher, K. (2013). *Geothermal Energy From Theoretical Models to Exploration and Development*. Springer.

The Human-Induced Earthquake Database (HiQuake) (2018). `https://inducedearthquakes.org/`. [Online; accessed 31.10.18].

Timur, A. (1977). Temperature dependence of compressional and shear wave velocities in rocks. *Geophysics*, 42:950–956.

Toksöz, M. N., Cheng, C. H., and Timur, A. (1976). Velocities of seismic waves in porous rocks. *Geophysics*, 41:621–645.

United Nations Climate Change (2019). `https://unfccc.int/process/the-paris-agreement/status-of-ratification`. [Online; accessed 25.04.19].

Williams, C. F., Reed, M. J., and Anderson, A. F. (2011). Updating the classification of geothermal resources. In *Thirty-Sixth Workshop on Geothermal Reservoir Engineering Stanford University*.

Wilson, C. J. N. and Rowland, J. V. (2016). The volcanic, magmatic and tectonic setting of the Taupo Volcanic Zone, New Zealand, reviewed from a geothermal perspective. *Geothermics*, 59:168–187.

Wohletz, K. and Heiken, G. (1992). *Volcanology and Geothermal Energy*. University of California Press.

World Population Review (2019). `http://worldpopulationreview.com/countries/costa-rica-population/`. [Online; accessed 27.04.19].

Zang, A., Oye, V., Jousset, P., Deichmann, N., Gritto, R., McGarr, A., Majer, E., and Bruhn, D. (2014). Analysis of induced seismicity in geothermal reservoirs – an overview. *Geothermics*, 52:6–21.

Zhen-Wu, B. Y. (2010). Gas Geochemistry of the Miravalles, Pailas and Borinquen geothermal areas of Costa Rica, and a comparison with Reykjanes and Theistareykir geothermal fields, Iceland. `https://orkustofnun.is/gogn/unu-gtp-report/UNU-GTP-2010-33.pdf`. [Online; accessed 01.03.19].

Zhou, H.-W. (2003). Multiscale traveltime tomography. *Geophysics*, 68:1639–1649.

Zou, C., Zhao, Q., Zhang, G., and Xiong, B. (2016). Energy revolution: From a fossil energy era to a new energy era. *Natural Gas Industry B*, 3:1–11.